Dipl.-Ing. Delia Maria Fugger, BSc

Correlated impurities out of equilibrium in different environments: Auxiliary master equation approach

DOCTORAL THESIS

to achieve the university degree of

Doktorin der technischen Wissenschaften

submitted to

Graz University of Technology

Supervisor

Univ.-Prof. Dr.rer.nat. Enrico Arrigoni

Institute of Theoretical and Computational Physics

Graz, June 2020

AFFIDAVIT

I declare that I have authored this thesis independently, that I have not used other than the declared sources/resources, and that I have explicitly indicated all material which has been quoted either literally or by content from the sources used. The text document uploaded to TUGRAZonline is identical to the present doctoral thesis.

Date

Signature

Abstract

In this thesis, we study the Kondo effect in the Anderson impurity model under the influence of a bias voltage in two different environments. The model describes an impurity with a local electron-electron interaction coupled to two noninteracting leads at potentially different chemical potentials. Exchange processes of an unpaired impurity electron with the conduction electrons qualitatively change the energy spectrum and transport properties of the system leading to the emergence of the Kondo effect. Here, we consider one setup, where the impurity electron is additionally subjected to a local magnetic field and another one, where the leads display a pseudogap in the density of states. We are particularly interested in the interplay of these features with the bias voltage and their combined influence on the Kondo effect in the current-carrying steady state. Due to their many-body nature, the considered setups are hard to address numerically. We employ the recently developed auxiliary master equation approach in combination with two different schemes based on matrix product states for that purpose. By mapping to an auxiliary open quantum system, we can conveniently perform the time evolution and access the steady state as well as Green's functions in the steady state. The auxiliary system is addressed by means of matrix product states providing an efficient representation for the determination of both quantities. Our calculations yield very accurate results, when compared with the numerical renormalization group. Specifically, for the setup with the magnetic field, we determine the spin-dependent shift of the Kondo resonance in the spectrum as well as its counterpart in the differential conductance as a function of voltage. In case of the more challenging setup with the pseudogap leads, we investigate the fate of an inherent quantum phase transition under voltage bias.

Kurzfassung

Diese Arbeit befasst sich mit dem Kondo Effekt in Andersons Störstellenmodell unter dem Einfluss einer elektrischen Spannung in zwei unterschiedlichen Umgebungen. Dieses Modell beschreibt eine Störstelle, an der Elektronen miteinander in Wechselwirkung treten, gekoppelt an zwei nichtwechselwirkende Bäder, gegebenenfalls auf unterschiedlichen chemischen Potentialen. Austauschprozesse zwischen einem ungepaarten Störstellenelektron und den Leitungselektronen ändern qualitativ das Energiespektrum und die Transporteigenschaften des Systems und führen schließlich zur Ausbildung des Kondo Effekts. In dieser Arbeit betrachten wir einerseits eine Problemstellung, bei der das Störstellenelektron zusätzlich einem lokalen Magnetfeld ausgesetzt ist, und andererseits eine Problemstellung, in der die Bäder eine sogenannte Pseudo-Bandlücke in der Zustandsdichte aufweisen. Wir sind besonders am Zusammenspiel dieser Eigenschaften mit der Spannung interessiert und an deren gemeinsamer Auswirkung auf den Kondo Effekt im stromführenden stationären Zustand des Systems. Aufgrund ihrer Vielteilchennatur sind die betrachteten Problemstellungen numerisch schwer zugänglich. Wir verwenden zu diesem Zweck einen kürzlich entwickelten Ansatz, den „Auxiliary Master Equation Approach“, in Kombination mit zwei verschiedenen Schemata basierend auf Matrix-Produktzuständen. Die Abbildung auf ein offenes Quantensystem erlaubt es, bequem die Zeitentwicklung auszuführen, den stationären Zustand zu erreichen sowie Greensche Funktionen im stationären Zustand zu berechnen. Wir adressieren das offene System mit Hilfe von Matrix-Produktzuständen, welche eine effiziente Darstellung zur Ermittlung beider Größen bieten. Dieser Zugang erlaubt es, äußerst präzise Resultate im Vergleich zur numerischen Renormierungsgruppe zu generieren.

Für das System im Magnetfeld bestimmen wir die Spin-abhängige Verschiebung der Kondo Resonanz im Spektrum sowie ihren Gegenspieler in der differenziellen Leitfähigkeit als Funktion der Spannung. Im Falle der anspruchsvolleren Problemstellung mit der Pseudo-Bandlücke untersuchen wir das Schicksal eines inhärenten Quantenphasenübergangs unter dem Einfluss einer angelegten Spannung.

Acknowledgements

First of all, I want to thank my supervisor Enrico Arrigoni for giving me the opportunity to work in this interesting field, for his guidance and all the hours, also personal time, he spent on supporting my work. I am also very thankful for the pleasant work atmosphere and the opportunity to attend several interesting schools, workshops and conferences.

I gratefully acknowledge the contributions of the co-authors of my publications, Antonius Dorda, Max Sorantin and Daniel Bauernfeind here in Graz as well as Frauke Schwarz and Jan von Delft in Munich and thank them for the good collaboration.

Special thanks also to Andreas Hirczy for solving various computer related problems and Brigitte Schwarz for the administrative support.

Further I would like to thank all colleagues at the institute for interesting discussions about various topics at lunch and during the coffee breaks, the nice atmosphere and the hiking trips and skiing days spent together, the not yet mentioned in alphabetical order: Markus Aichhorn, Gerhard Dorn, Michael Draxler, Viktor Eisler, Johanna Ganglbauer, Paolo Gazzaneo, Johannes Graspeuntner, Matthias Gruber, Winfried Kernbichler, Christian Kokail, Gernot Kraberger, Roman Lucrezi, Florian Maislinger, Markus Richter, Michael Rumetshofer, Hermann Schnait, Irakli Titvinidze, Robert Triebl, Wolfgang von der Linden and Manuel Zingl.

Last but not least, I want to thank my family, particularly my mother Petra and my sister Valentina, and my fiancé Georg for their support and encouragement over these years.

List of Publications

[1] D. M. Fugger, A. Dorda, F. Schwarz, J. von Delft, and E. Arrigoni. Nonequilibrium Kondo effect in a magnetic field: auxiliary master equation approach. *New J. Phys.* 20, 013030 (2018).

[2] M. E. Sorantin, D. M. Fugger, A. Dorda, W. von der Linden, and E. Arrigoni. Auxiliary master equation approach within stochastic wave functions: Application to the interacting resonant level model. *Phys. Rev. E* 99, 043303 (2019).

[3] D. M. Fugger, D. Bauernfeind, M. E. Sorantin, and E. Arrigoni. Nonequilibrium pseudogap Anderson impurity model: A master equation tensor network approach. *Phys. Rev. B* 101, 165132 (2020).

List of Figures

Contents

Chapter 1

Introduction

Many exciting phenomena in physics have collective nature, i.e. they arise due to interactions between a system's constituents, such as electrons or phonons, and cannot be explained just by adding up the individual behavior of the constituents [4]. Prominent examples involve superconductivity [5, 6], ferromagnetism [7], quantum criticality [8], the Mott transition [9], heavy fermions [10] and the Kondo effect [11]. Besides the fundamental interest in understanding these phenomena, also their application in present and proposed future technologies is potentially manifold, ranging, e.g., from the energy sector [12] to medicine [13] and information processing [14].

From a technological perspective, there is a trend towards miniaturization, smaller and faster devices are built for enhanced performance and, at the same time, reduced costs. At the nanoscale, classical device characteristics are altered by quantum mechanical effects, such as energy and charge quantization [15], and electronic interactions typically play a bigger role [16]. This is a curse and a blessing at the same time: It introduces new challenges to cope with [17], but also opens up pathways for completely new types of devices, which are based on the laws of quantum mechanics rather than compromised and exploit strong interactions for their functionality [18].

While the motivation to study many-body systems on a microscopic level is strong, this turns out to be very hard in practice and we usually have to rely on approximate models, such as the Hubbard model [19], the related

Anderson impurity model [20] or the Ising model [21]. These models involve only a small number of parameters crucial to capture the underlying physics. Despite this, analytical solutions of these models are scarce and accurate numerical solutions tend to be hard to obtain. Out of equilibrium, where devices typically operate, this hardship is particularly severe, since we cannot exploit thermodynamics principles for simplification, but have to deal with the full many-body quantum dynamics.

There is a plethora of interesting questions to address out of equilibrium, such as the transport properties of a many-body system in the steady state [22], its transient behavior in the course of a pump-probe experiment [23] or the effects of periodic driving [24, 25]. Other fundamental questions involve nonequilibrium quantum phase transitions [26], dissipation and decoherence [27] and thermalization after a quench [28], to name a few. Describing a quantum many-body system up to the nonequilibrium steady state with high accuracy poses a great challenge, and method development in this direction is currently a very active field of research [22, 29, 30].

In this thesis, we address the Kondo effect in the nonequilibrium steady state of the Anderson impurity model under voltage bias employing the auxiliary master equation approach in combination with matrix product states techniques. We study the model, consisting of an interacting impurity site in contact with two noninteracting leads in two different environments, with a local magnetic field and with a pseudogap in the leads' density of states. We focus on the interplay of these features with the bias voltage and their combined effect on the spectral and transport properties.

Three published papers originated from the present thesis. For two of them I was the main contributor and, accordingly, first author. Therefore, these two papers [1, 3] are included literally as an integral part of this thesis in Chs. 5 and 6. The further organization is as follows: Ch. 2 contains an introduction to the Kondo effect and the Anderson impurity model, in Ch. 3 the auxiliary master equation approach is motivated and Ch. 4 deals with matrix product states techniques. Finally, Ch. 7 holds general conclusions and an outlook to possible future studies.

Chapter 2

Kondo effect

This chapter deals with the Kondo effect, one of the main topics I have studied during my PhD. It aims at providing introductive and complementary material to my two main publications, presented in Ch. 5 and Ch. 6, to make them more accessible. I tried to avoid overlaps with Secs. 5.2, 6.2 and Secs. 5.3.1, 6.3.1, which also touch the basics of the Kondo effect, as much as possible. For this chapter, I used the books by Hewson [31] and Coleman [32] as well as the feature [33] as main sources of information. This chapter is organized as follows:

In Sec. 2.1, the Kondo effect is introduced and ambiguities in the terminology are clarified. Sec. 2.2 is meant to put the topic into historical context, providing an overview of the developments since the discovery of the effect up to the present. In Sec. 2.3, the Anderson impurity model is introduced with particular focus on the spectral properties. This is the model of interest in my two main publications, Refs. [1, 3], whose objectives are introduced in Sec. 2.4.

2.1 Terminology

In ordinary metals, the resistance R decreases monotonically as the temperature T is lowered, because electron-phonon scattering is reduced. Further, it takes a constant finite value as T approaches absolute zero, due to potential

scattering on defects.[1]

The situation is quite different, when the metal contains magnetic impurities, such as atoms from the $3d$ transition element or the $4f$ rare earth series. In this case, the resistance first goes down upon decreasing the temperature, as in ordinary conductors, then it takes a minimum at $T \approx T_K$ and rises again as $T \to 0\,\mathrm{K}$, see Fig. 2.1(a). This behavior is caused by a magnetic contribution to the scattering by the impurities, which strongly depends on the temperature. When the magnetic scattering overcomes the electron-phonon scattering, a minimum occurs. This effect is termed *Kondo effect* and the temperature T_K is called *Kondo temperature*.

The process of magnetic scattering also triggers the entanglement of electrons at the impurities with conduction electrons of the metal at temperatures $T \ll T_K$, culminating in the formation of a very special ground state. In this ground state, the magnetic moments of the impurity atoms are entirely screened by the spins of the conduction sea. This ground state shows up as a resonance of width T_K at the chemical potential μ in the local density of states at the impurities, the so-called *Kondo resonance*, see also Fig. 2.4. Its occurrence is nowadays also often referred to as Kondo effect.

So, the Kondo temperature sets a crossover[2] between a regime, where local magnetic moments are present, due to the free spins at the impurities ($T \gg T_K$), and the Kondo regime, where the impurity spins are screened and no net magnetic moments survive ($T \ll T_K$), see Fig. 2.2. Remarkably, in the Kondo regime, the physics is completely governed by T_K, $k_B T_K$ being the only relevant energy scale, and observables, such as the resistance, are universal functions of T/T_K. This implies that all $R(T)$ curves, independent of any physical details of the experiments they result from, follow the same function $f(T/T_K)$.

Notice that quantum dots also display the Kondo effect. These are tiny pieces of semiconductor, where electrons are confined and have quantized states, resembling the states in an atom. The same mechanisms that are

[1] Some metals suddenly loose their resistance completely and become superconducting. This is associated with a phase transition at a critical temperature, below which electrons form a condensate of Cooper pairs.

[2] Notice that no phase transition is involved here, but a smooth crossover.

responsible for the resistance minimum in bulk metals with dilute magnetic impurities cause the opposite effect in quantum dots, see also Fig. 2.1(b). Here the conductance G takes a minimum at $T \approx T_K$ and rises again as $T \to 0\,\mathrm{K}$ to reach its quantum limit of $2\frac{e^2}{h}$. The different behavior is related to the different geometries: In a metal, electrons can circumvent the impurities and the magnetic scattering process hinders their motion. Quantum dots, on the other hand, are not surrounded by metal, but locally coupled to electrodes. In order to get from one electrode to another, electrons are forced to travel through the dot and the Kondo resonance at the chemical potential supports the transport.[3]

2.2 Historical overview

Historically, the Kondo effect was first observed in gold by de Haas, de Boer and van dën Berg in 1934 [34]. Based on measurements by Clogston, Matthias *et al.* [35] and Sarachik *et al.* [36] the resistance minimum could be linked to the presence of magnetic moments. On the theoretical side, Friedel introduced the concept of virtual bound states, states that are almost localized at the impurity sites [37]. This concept was taken up by Anderson, who came up with an effective model for the situation of the impurities in the metal. The Anderson impurity model was also able to explain the formation of magnetic moments based on strong interactions between electrons [20].

Three decades after its discovery, the Kondo effect was explained by Kondo, who addressed another impurity model, the s-d model, which is nowadays also called Kondo model [38, 39]. Within third order perturbation theory he found a magnetic contribution to the scattering and therefore to the resistance $\propto \ln T$ [11]. Together with the phonon contribution $\propto T^5$ this accounts for the resistance minimum.[4] However, the perturbation theory breaks down as $T \to 0\,\mathrm{K}$,[5] so with this approach, the behavior at very low temperatures $T \ll T_K$ could not be explained. This posed another long-standing problem which was termed *Kondo problem*.

[3] In quantum dots, the conductance is measured from the impurity electrons.
[4] The potential scattering contribution is almost constant.
[5] $\ln T$ diverges

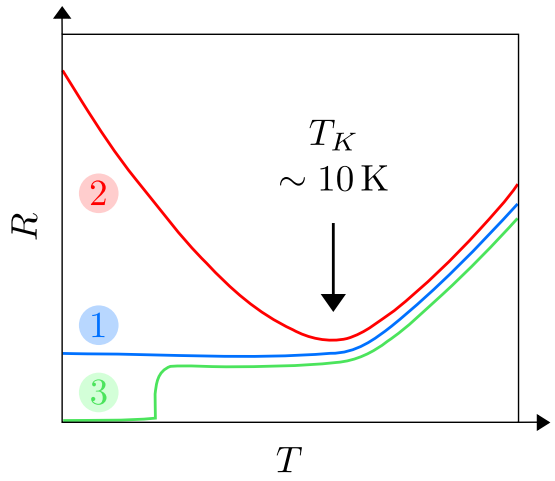

(a)

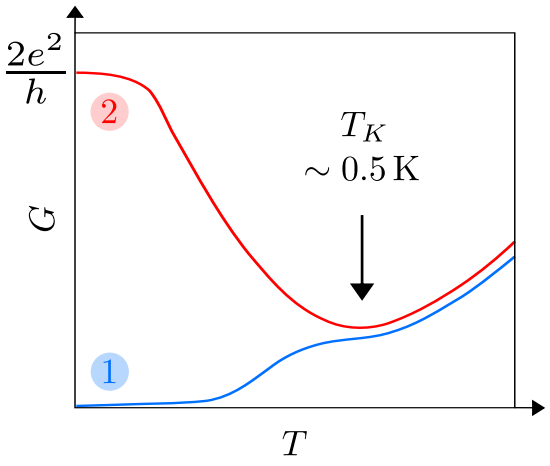

(b)

Figure 2.1: (a) Qualitative behavior of the resistance R in dependence of temperature T for (1) an ordinary metal, (2) a metal with dilute magnetic impurities displaying the Kondo effect and (3) a superconductor. (b) Conductance G in a quantum dot (1) in so-called Coulomb blockade (for an even number of electrons at the dot) and (2) in the Kondo regime (for an odd number). This representation was adapted from [33].

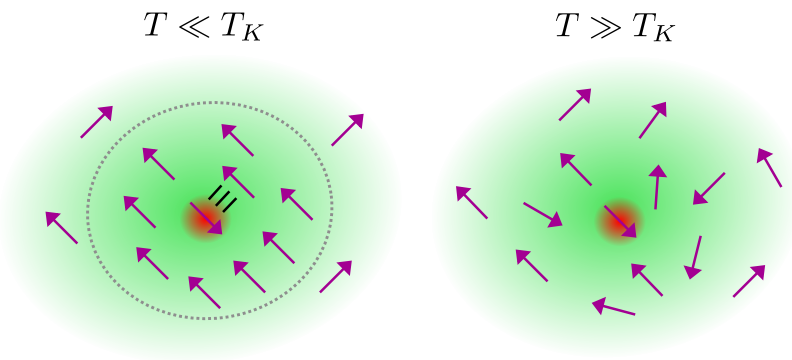

Figure 2.2: Situation in a system capable of the Kondo effect. Impurity (red circle) surrounded by a Kondo screening cloud at $T \ll T_K$ versus free electron spins (purple arrows) at $T \gg T_K$.

Another decade later, Wilson devised the numerical renormalization group and solved the Kondo problem numerically, which was recognized with the award of the Nobel Prize in 1982 [40]. Wilson thereby confirmed a hypothesis, which had been proposed based on the results of previous, unsuccessful attempts to solve the Kondo problem: In the ground state of the Kondo model the impurity electron is bound to the conduction electrons in a singlet state. This holds true also for the Anderson impurity model, which is linked to the Kondo model in the low-energy regime by a Schrieffer-Wolff transformation [41]. Other experimental results for the transport and thermodynamic properties at very low temperatures $T \ll T_K$ could be interpreted by Nozières in terms of a Landau Fermi liquid theory [42]. Later, this theory was microscopically derived on the basis of the Anderson impurity model [43, 44].

In 1980, Wiegmann and Andrei independently came up with an exact solution to the Kondo model employing Bethe ansatz [45, 46]; shortly afterwards also the Anderson impurity model was solved exactly. However, Bethe ansatz does not provide the possibility to access Green's functions as desirable for comparison with experiments, such as photoemission or neutron scattering [47, 48]. A variety of methods with different degrees of approximation emerged to meet this challenge, see e.g. [43, 49–51]. They all have in common that they yield a very narrow many-body resonance in the impurity density of states at the Fermi level, which was termed Abrikosov-Suhl

resonance [52, 53] and, later on, Kondo resonance. This ground state resonance accounts for the anomalous low-energy behavior of metals with dilute magnetic impurities and, nowadays, its build-up is also often referred to as Kondo effect.

Having assessed most aspects of the Kondo effect in theory by considering impurity models in equilibrium, i.e. at bias voltage $\phi = 0\,\mathrm{V}$, and employing linear response theory, the next step was to reach out for nonequilibrium. This is of fundamental interest and provides a more realistic description of many experiments. Meir and Wingreen were the first to observe a suppression, broadening and splitting of the Kondo resonance at finite bias voltages [54, 55] and their results have been confirmed, extended and refined by many other works up to now [56–65]. Sill, there is no state-of-the-art method to address the Kondo effect out of equilibrium. Studying the Anderson impurity model in different, nonequilibrium situations and according method development also poses the main issue of this thesis.

The Kondo effect and the impurity models have enjoyed renewed interest in the rapidly growing field of nanotechnology, which allows not only to study matter on an atomic scale, but also to manipulate and control it. An important tool in this context is the scanning tunnelling microscope. It allows to place individual atoms on a surface, such as magnetic impurities on a metal, forming any desired structure, and to measure the local energy spectrum with atomic resolution. This gives rise to a completely new type of experiments, where the position of the impurity atoms is known, may even be tuned, prior to measuring the Kondo effect [33, 66].

Exploiting modern chip technologies, on the other hand, quantum dots can be manufactured, which also display the Kondo effect, but in a way different from their bulk-metal counterparts [67, 68], as sketched in the previous Sec. 2.1. They are often well described by impurity models, whose parameters can be faithfully tuned in the laboratory [67, 69]. This also opens up new pathways for experiments: Just recently, the Kondo screening cloud was observed for the first time by Borzenets, Shim, Chen, Ludwig, Wieck, Tarucha, Sim and Yamamoto [70]. They studied a setup where a quantum dot is coupled to a Fabry-Pérot interferometer. Upon tuning a voltage on the in-

terferometer end gate, they measured oscillations in the Kondo temperature, which is a signature of the Kondo cloud.

Further, impurity models have enjoyed a revival within dynamical mean-field theory [71, 72]. This approach, invented by Georges, Kotliar, Metzner and Vollhardt, addresses the physics of strongly-correlated materials by mapping the (intractable) lattice problem onto an impurity model, which has to be solved self-consistently. In this respect, the impurity problem constitutes the bottleneck problem of the theory and the corresponding solution methods are referred to as impurity solvers. Therefore, it is also interesting to develop new accurate and efficient methods to solve impurity models under different conditions, out of equilibrium, in particular, as in the present thesis. The latter allows to extend the dynamical mean-field theory to treat strongly-correlated lattice problems also out of equilibrium [25, 73–77].

2.3 Anderson impurity model

The Anderson impurity model or, more precisely, the single-impurity Anderson model, can be used to effectively describe the situation of magnetic impurities immersed in a metal. The corresponding Hamiltonian reads

$$H = \overbrace{U n_{f\uparrow} n_{f\downarrow}}^{H_{\mathrm{imp}}} + \underbrace{\sum_{\sigma} \varepsilon_f n_{f\sigma} + \sum_{\boldsymbol{k}\sigma} \varepsilon_{\boldsymbol{k}} n_{\boldsymbol{k}\sigma} + \sum_{\boldsymbol{k}\sigma} \left(V_{\boldsymbol{k}} c^{\dagger}_{\boldsymbol{k}\sigma} f_{\sigma} + V^{*}_{\boldsymbol{k}} f^{\dagger}_{\sigma} c_{\boldsymbol{k}\sigma} \right)}_{H_{\mathrm{res}}} . \tag{2.3.1}$$

It models the impurity as a single localized orbital $\psi_f(\boldsymbol{r})$ with on-site energy ε_f that can either be empty or occupied by one or two electrons with opposite spins. Double occupancy is punished via the on-site interaction U that accounts for the Coulomb repulsion of electrons,[6]

$$U = \int d^3r \, d^3r' \; V_{\mathrm{c}}(\boldsymbol{r} - \boldsymbol{r'}) \, \rho_f(\boldsymbol{r}) \rho_f(\boldsymbol{r'}) \, , \qquad V_{\mathrm{c}}(\boldsymbol{r}) = \frac{e^2}{4\pi\epsilon_0 |\boldsymbol{r}|} \, . \tag{2.3.2}$$

[6] The total energy in the system is increased for repulsive $U > 0$.

Here, $V_c(\boldsymbol{r})$ is the Coulomb potential and $\rho_f(\boldsymbol{r}) = |\psi_f(\boldsymbol{r})|^2$ is the electron density in the impurity orbital. Further, $f_\sigma^{(\dagger)}$ destroys (creates) an electron at the impurity with spin σ and $n_{f\sigma} = f_\sigma^\dagger f_\sigma$ is the corresponding particle number operator.

The metal is modeled as effectively free electrons with dispersion $\varepsilon_{\boldsymbol{k}} \in [-D, D]$ within a conduction band of width $2D$. When the impurity is embedded in the metal, its orbital hybridizes with the Bloch waves of the conduction sea, giving rise to

$$V_{\boldsymbol{k}} = \int d^3r \; e^{-i\boldsymbol{k}\cdot\boldsymbol{r}} V_{\text{ion}}(\boldsymbol{r})\psi_f(\boldsymbol{r})\,. \tag{2.3.3}$$

Here, $V_{\text{ion}}(\boldsymbol{r})$ is the potential of the impurity ion, $c_{\boldsymbol{k}\sigma}^{(\dagger)}$ destroys (creates) an electron in the conduction band with momentum $\boldsymbol{k}$ and spin σ and $n_{\boldsymbol{k}\sigma} = c_{\boldsymbol{k}\sigma}^\dagger c_{\boldsymbol{k}\sigma}$ is again the corresponding particle number operator.

In order to gain insight into the physics of magnetic impurities dissolved in a metal, the following two limiting cases of the Anderson impurity model are particularly interesting (see Eq. (2.3.1) for definitions):

- H_{imp} describes the atomic limit of an isolated impurity. It explains the formation of local moments based on strong interaction U.
- H_{res} is the noninteracting limit. It shows the emergence of a resonance, due to the impurity, which is a virtual bound state resonance.

2.3.1 Atomic limit

In order to understand the physics of the model, it is convenient to first consider the atomic limit of an isolated impurity H_{imp} and study, in which parameter regime local moments develop by solving the corresponding eigenvalue problem.

The Hamiltonian H_{imp} (2.3.1) has four eigenstates, which are listed in Tab. 2.1 together with the corresponding eigenenergies. In order to obtain the magnetic doublet $(|\uparrow\rangle\,, |\downarrow\rangle)$ as ground state, transitions to all other states must cost nonzero energy. As easily checked, adding or removing one electron

to or from the singly-occupied sector is associated with an excitation energy,

$$\Delta E = \frac{U}{2} \pm \left(\varepsilon_f + \frac{U}{2} \right) . \tag{2.3.4}$$

This excitation energy is positive and, thus, the ground state magnetic for $U > |2\varepsilon_f + U|$, which is also illustrated in the phase diagram in Fig. 2.3. In this scenario, if the impurity is probed below the smallest excitation energy $\Delta E_{\text{min}} = \frac{U}{2} - \left|\varepsilon_f + \frac{U}{2}\right|$, the charge degree of freedom is unaffected and it

states	energy	magnetic
$\|0\rangle$	0	no
$\|\uparrow\rangle$, $\|\downarrow\rangle$	ε_f	yes
$\|\uparrow\downarrow\rangle$	$2\varepsilon_f + U$	no

Table 2.1: Eigenstates and eigenenergies of H_{imp}.

behaves as a local moment. When coupled to the conduction sea, the Kondo effect shows up in the parameter regime, where the local moments develop (orange colored area).

In this thesis, we are interested in the symmetric model, $2\varepsilon_f + U = 0$, where the states $|\uparrow\downarrow\rangle$ and $|0\rangle$ are degenerate (and repulsive $U > 0$).

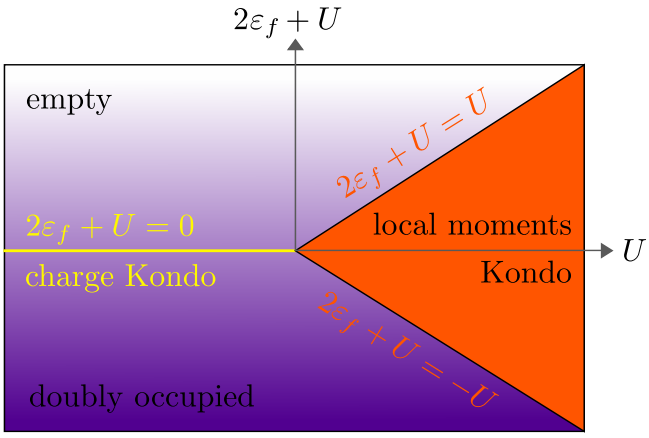

Figure 2.3: Phases of H_{imp} and parameter regimes, where the Kondo effect and the charge Kondo effect arise, when the impurity is immersed in a metal. This representation was adapted from [32].

Notice that in the symmetric model for attractive $U < 0$, the charge

doublet ($|\uparrow\downarrow\rangle$, $|0\rangle$) is the ground state (yellow line). This ground state gives rise to the so-called *charge Kondo effect*, when coupled to the conduction sea [78], but this is out of scope of this thesis.

2.3.2 Noninteracting limit

When embedded in a metal, the impurity orbital hybridizes with the Bloch waves of the conduction sea allowing electrons to tunnel in and out with amplitude $V_{\boldsymbol{k}}$. Now, we study the consequences of this fact for the impurity spectrum in the noninteracting limit H_{res} (2.3.1), using Green's functions.

For simplicity, we consider the particular case, where the retarded hybridization function has a constant imaginary part,[7]

$$-\Im\Delta^R(\varepsilon) = \pi \sum_{\boldsymbol{k}} |V_{\boldsymbol{k}}|^2 \delta(\varepsilon - \varepsilon_{\boldsymbol{k}}) \equiv \Gamma = const. \tag{2.3.5}$$

for $\varepsilon \in [-D, D]$. Note that $\Re\Delta^R(\varepsilon) = \mathcal{O}(\varepsilon/D)$ can be neglected for a wide conduction band. In this case, the retarded impurity Green's function is

$$G^R(\varepsilon) = \frac{1}{\varepsilon - \varepsilon_f + i\Gamma}\,, \tag{2.3.6}$$

which follows from Dyson's equation (5.3.11) with $g_0^R = (\varepsilon - \varepsilon_f + i0^+)^{-1}$ and zero Keldysh component. The corresponding spectral function is determined via $A(\varepsilon) = -\Im G^R(\varepsilon)/\pi$, yielding

$$A(\varepsilon) = \frac{1}{\pi} \frac{\Gamma}{(\varepsilon - \varepsilon_f)^2 + \Gamma^2}\,. \tag{2.3.7}$$

This is a Lorentzian of width Γ and maximum $1/(\pi\Gamma)$ located at $\varepsilon = \varepsilon_f$, see also Fig. 2.4. So, the hybridization has a broadening effect. The resonance, Eq. (2.3.7), is called a virtual bound state resonance, since the corresponding states are not completely localized like atomic bound states, but become Bloch waves far from the impurity (instead of decaying rapidly).

[7] This also happens to be a commonly studied case in Kondo physics.

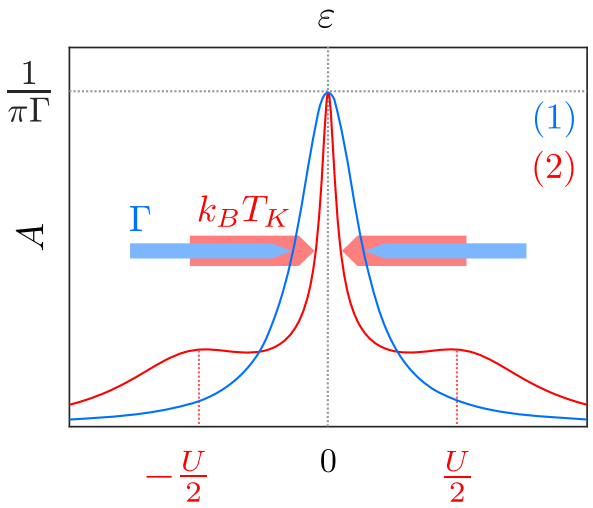

Figure 2.4: Impurity spectrum $A(\varepsilon)$ in the symmetric Anderson impurity model for (1) $U = 0$ displaying a Lorentzian and (2) $U > 0$ displaying the Kondo resonance in the center and the Hubbard bands to the left and right.

2.3.3 General case

The Coulomb interaction, which tends to localize electrons and which drives the formation of magnetic moments, and the hybridization, which enables them to spread over the whole metal, are competing. In the full Anderson impurity model, Eq. (2.3.1) with $U \neq 0$ and $V_{\boldsymbol{k}} \neq 0$, it is, thus, obvious that a local moment can only develop, if the interaction exceeds the hybridization to a sufficient extent. From mean-field theory it follows that $U \gtrsim \pi\Gamma$ must be fulfilled.

One expects that, at finite U, the virtual bound state resonance in the impurity spectrum splits into two peaks associated with the charge excitation energies of the isolated impurity, Eq. (2.3.4). In detail, a spectral decomposition of the impurity spectral function yields:

$$A(\varepsilon) = \begin{cases} \overbrace{\sum_\lambda \left|\langle\lambda|f_\sigma^\dagger|\phi_0\rangle\right|^2 \delta(\varepsilon - [E_\lambda - E_0])}^{\text{adding one impurity electron}} & (\varepsilon > 0) \\ \underbrace{\sum_\lambda \left|\langle\lambda|f_\sigma|\phi_0\rangle\right|^2 \delta(\varepsilon - [E_0 - E_\lambda])}_{\text{removing one impurity electron}} & (\varepsilon < 0) \end{cases} \tag{2.3.8}$$

Here, $|\phi_0\rangle$ and $|\lambda\rangle$ are the ground state and excited states of the full Hamiltonian, Eq. (2.3.1), and E_0 and E_λ are the corresponding energies. Since these energies enter only as differences, we can approximate the result by substituting them with the eigenenergies in the atomic limit, Tab. 2.1. In this way, in the regime where the ground state is magnetic ($|\uparrow\rangle, |\downarrow\rangle$), we obtain two peaks separated by U, one located at ε_f and another one at $\varepsilon_f + U$. These peaks have a width of $\approx \Gamma$[8] and they are called Hubbard bands.

In the symmetric Anderson impurity model, $2\varepsilon_f + U = 0$, which we consider in the present thesis, the Hubbard bands are located at $\approx \pm U/2$, while the Lorentzian in the noninteracting limit is centered around zero energy. So, at large U, one would expect all indications of this Lorentzian to vanish and no spectral weight to be left at zero energy. Contrary to this expectation, it turns out that there is always a peak at $\varepsilon = 0$.[9] It becomes progressively narrower with increasing U, but its height is pinned to $1/(\pi\Gamma)$ [79]. This peak is the Kondo resonance, see Fig. 2.4. Whereas the emergence of the Hubbard bands may be explained in the atomic limit of an isolated impurity, the Kondo resonance is a genuine many-body effect that has no atomic counterpart. We saw that the Hubbard bands are due to valence fluctuations and describe charge excitations. The Kondo resonance, on the other hand, is associated with spin fluctuations.

The tunneling of electrons between the impurity and the metal can effectively cause a spin flip at the impurity. This happens as a second-order process via a virtual state, which violates the conservation of energy, see Fig. 2.5. The energy that an impurity electron classically requires to move into the bath, i.e. the transition energy to the virtual state, typically amounts to $|\varepsilon_f| = (1-10)$eV. Albeit classically forbidden, the Heisenberg uncertainty principle allows such a transition to take place without introducing energy into the system, provided that the virtual state decays within a short time span $\approx h/|\varepsilon_f|$. Within this time span, another bath electron has to tunnel onto the impurity, in order to restore the energy balance. This new impurity

[8] Thus, it is obvious that we will see two distinct peaks only for sufficiently large U/Γ.
[9] which corresponds to the position of the chemical potential in the metal

electron may have opposite spin[10] creating a spin excitation in the Fermi sea. Such exchange processes qualitatively change the energy spectrum at the impurity and lead to the Kondo resonance.

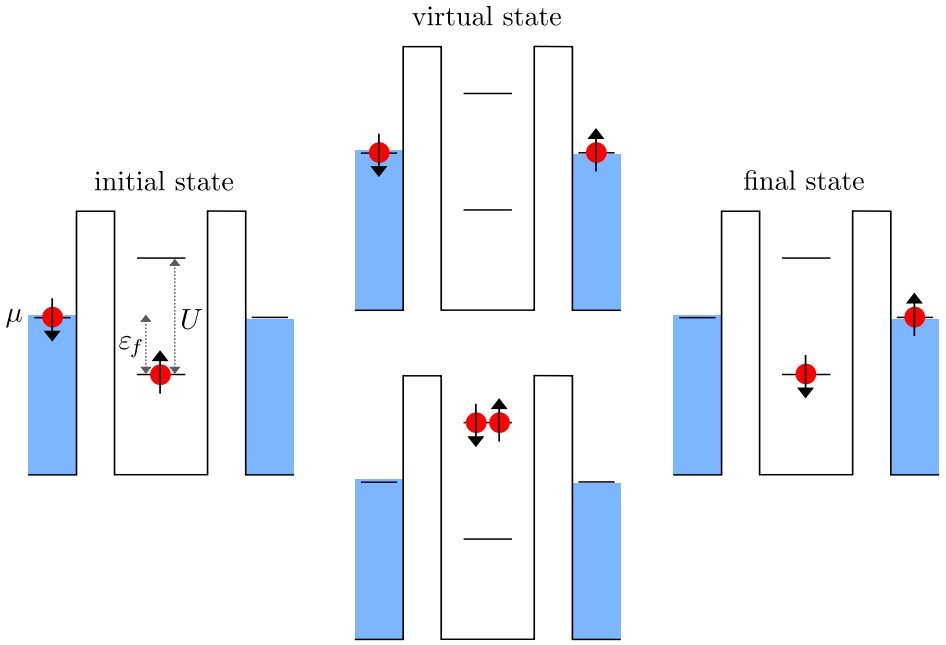

Figure 2.5: Spin-flip scattering process. (left) An impurity electron (red circle) with spin up tunnels into the bath (blue) leaving the impurity empty, which is classically high-energetic (upper panel). Then a spin-down bath electron tunnels onto the impurity, restoring a singly-occupied state (right), while creating a spin excitation in the bath. The order of tunnelings may also be exchanged leading to a doubly-occupied high-energy state (lower panel). This representation was adapted from [33].

Assuming that the spin-flip scattering takes place with a rate τ_{sf}^{-1}, the Kondo temperature may be defined in the following way,[11]

$$k_B T_K = \frac{\hbar}{\tau_{\mathrm{sf}}} = \sqrt{\frac{2U\Gamma}{\pi}} \exp\left(-\frac{\pi U}{8\Gamma}\right). \tag{2.3.9}$$

As noted in Sec. 2.1, T_K sets the crossover between the local moment regime ($T \gg T_K$), where the impurity spin is free, and the Kondo regime ($T \ll T_K$),

[10] with respect to the initial impurity electron

[11] Note that there are various definitions of the Kondo temperature, whose numerical values differ slightly, the scale, however, is the same.

where it is screened. In the Kondo regime, the impurity electron entangles with the conduction electrons via spin-flip scattering and the ground state is a spin singlet. Further, the system behaves as a Fermi liquid, see Fig. 2.6.

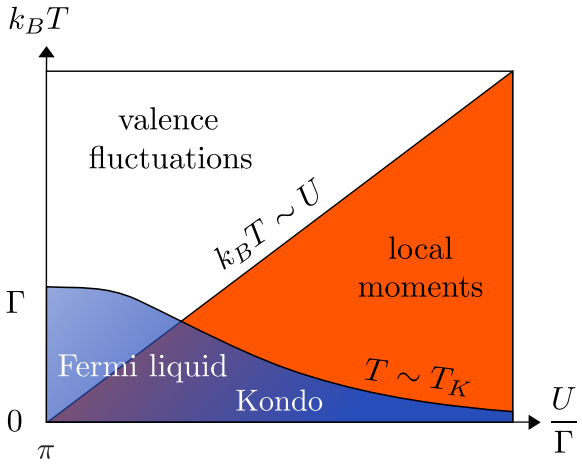

Figure 2.6: Phases of H (2.3.1) and parameter regime, where the Kondo effect arises. This representation was adapted from [32].

2.3.4 Out of equilibrium

As discussed in the previous Sec. 2.3.3, the Kondo resonance develops at the position of the chemical potential of the metal.[12] If the impurity is connected to two leads at different chemical potentials, realizing a bias voltage $\phi = \mu_R - \mu_L$, one expects two resonances to emerge, one at each chemical potential. In fact, upon turning on a bias voltage, the Kondo resonance is first broadened and, at some critical voltage, it splits into two peaks, which, at large bias, are located at μ_L and μ_R, respectively. The amplitudes of these split peaks are suppressed by dissipative processes, where electrons are transferred from the lead with the higher chemical potential to the one with the lower chemical potential. These processes also cause a broadening $\frac{\hbar}{\tau_d}$, where τ_d the dissipative lifetime, see Fig. 2.7. So, out of equilibrium, the emergence of two new energy scales[13] is observed, $e\phi$ and $\frac{\hbar}{\tau_d}$, which are linked to the bias voltage as well as the dissipative lifetime [54].

[12] which was at $\varepsilon = 0$
[13] in addition to k_BT_K

However, while the small bias regime, $\phi \approx 0$, is easily accessed via linear response theory and perturbation theory can be employed at large bias, the intermediate regime $e\phi \approx k_B T_K$ is challenging and only a few approaches are capable of generating accurate results also for large times in the steady state. The auxiliary master equation approach, employed in this thesis, is one of them, see Ch. 3 as well as Ref. [63].

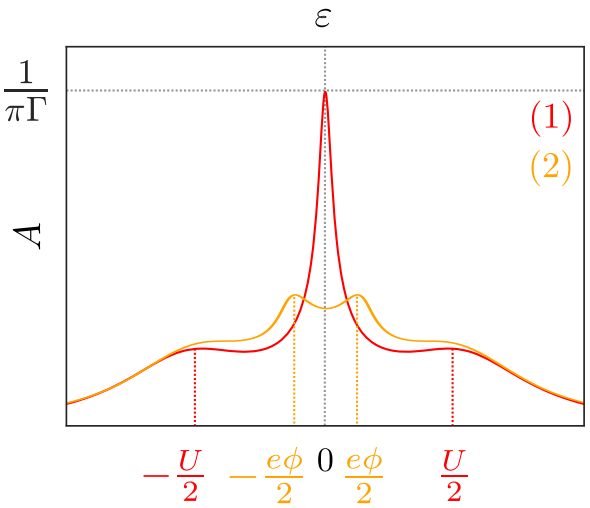

Figure 2.7: Impurity spectrum $A(\varepsilon)$ in the symmetric Anderson impurity model for (1) $\phi = 0$ displaying the Kondo resonance and (2) $\phi > 0$ displaying the broadened and suppressed Kondo split peaks at the chemical potentials $\mu_\lambda = \pm\frac{e\phi}{2}$.

2.4 This work

In the present thesis, we study the Kondo effect in the steady state of the Anderson impurity model under voltage bias in two different environments, in a local magnetic field, on the one hand, and with a pseudogap in the density of states of the leads, on the other hand.

A local magnetic field B at the impurity produces a spin-dependent shift in the on-site energies in Eq. (2.3.1), according to $\varepsilon_f \to \varepsilon_f \pm \frac{1}{2}\Delta\varepsilon$, where $\Delta\varepsilon = |g|\mu_B B$ is the Zeeman splitting. Therefore, one expects to observe a shift in the Kondo resonance as well, naively by the same amount as in the

on-site energies. However, the situation turns out to be more complex, and, for large magnetic fields, the peaks emerge at the positions of the Zeeman splitting $\pm\Delta\varepsilon$ [54]. The spectral shift also affects the differential conductance, which takes a maximum, when the Kondo split peaks enter the transport window at $e\phi \approx \Delta\varepsilon$. Again, the intermediate regime $\Delta\varepsilon \approx k_B T_K$ is most challenging, in particular with a bias voltage applied. In this case, one expects to see four peaks for certain parameter combinations, located at $\pm\Delta\varepsilon \pm \frac{e\phi}{2}$ [80]. In this thesis, we examine the discussed properties with the auxiliary master equation approach in combination with matrix product states, see Ch. 5 or Ref. [1].

At zero magnetic field, the Kondo resonance emerges at the chemical potential of the metal, see Sec. 2.3.3. So, the density of states at the chemical potential has a crucial influence on the effect. In particular, if there is a gap, the Kondo resonance cannot (fully) develop. However, in case of a pseudogap, i.e. a density of states $\propto |\varepsilon - \mu|^r$, which is zero directly at the chemical potential and finite elsewhere, a quantum phase transition is observed[14] depending, i.a., on the exponent r [81, 82]. The fate of this quantum phase transition under the influence of a bias voltage is not a priori clear and is also subject of studies in this thesis, see Ch. 6 or Ref. [3].

[14] in contrast to the crossover in the ordinary Anderson impurity model

Chapter 3

Auxiliary Master Equation Approach

This chapter is devoted to introducing and motivating the auxiliary master equation approach (AMEA), a numerical method that has been developed in our working group. It is particularly well suited to deal with impurity problems out of equilibrium, such as those studied in Refs. [1, 3] and presented in Chs. 5 and 6. Further details about AMEA can be found in Refs. [63, 83]. The books by Schaller [84] and Breuer and Petruccione [85] as well as Ref. [86] are also serving as sources of information.

Before addressing the actual subject of this chapter, we first review the physics of closed quantum systems in Sec. 3.1. Afterwards, in Sec. 3.2, an overview of open quantum systems is given, which can be employed to model a bias voltage. In Sec. 3.2.1, the Lindblad master equation is presented. This is the central equation in the auxiliary master equation approach, which is introduced in Sec. 3.3. The following Sec. 3.4 deals with the super-fermion representation, which is a useful tool for solving master equations. Finally, this representation is applied to the Anderson impurity model, see Sec. 3.5. In particular, the structure of the Lindblad equation, which is solved in Chs. 5 and 6, is derived.

Throughout the whole chapter (except for the last Sec. 3.5), all ordinary operators are indicated by a hat and the introduced super-operators, i.e.

operators acting on other operators producing again other operators as a result, are indicated by a double hat, to omit confusions.

3.1 Closed quantum systems

Pure states: In a closed quantum system, a pure state $|\psi(t)\rangle$ evolves in time, due to the action of a Hamiltonian $\hat{H}(t)$, as described by the Schrödinger equation,[1]

$$i\hbar\frac{d}{dt}|\psi(t)\rangle = \hat{H}(t)\,|\psi(t)\rangle\ . \tag{3.1.1}$$

The solution to Eq. (3.1.1) can be expressed in terms of a unitary time evolution operator $\hat{U}(t,t_0)$, which maps an initial state $|\psi(t_0)\rangle$ to a final state $|\psi(t)\rangle$, according to

$$|\psi(t)\rangle = \hat{U}(t,t_0)\,|\psi(t_0)\rangle\ . \tag{3.1.2}$$

Inserting this into the Schrödinger equation results in a differential equation for $\hat{U}(t,t_0)$, which is solved by the following expression,

$$\begin{aligned}\hat{U}(t,t_0) &= \hat{T}\exp\left[-\frac{i}{\hbar}\int_{t_0}^{t}\mathrm{d}\tau\hat{H}(\tau)\right]\\ &\overset{\hat{H}\neq\hat{H}(\tau)}{=}\exp\left[-\frac{i}{\hbar}\hat{H}(t-t_0)\right].\end{aligned} \tag{3.1.3}$$

Here, $\hat{T}$ is the chronological time ordering operator. It arranges products of operators to its right such that their time arguments increase from the right to the left. Since the Hamiltonian is Hermitian, $\hat{H}=\hat{H}^\dagger$, the time evolution operator is unitary, $\hat{U}^\dagger\hat{U}=\hat{U}\hat{U}^\dagger=\hat{\mathbb{1}}$. Finally, time dependent expectation values of operators $\hat{O}$ are obtained as

$$\langle\hat{O}(t)\rangle = \langle\psi(t)|\hat{O}|\psi(t)\rangle\ . \tag{3.1.4}$$

[1]Notice that the Hamiltonian may depend on time, even though the system is said to be closed. Such a treatment may apply, under certain conditions, to systems that are driven by external forces, such as an electromagnetic field.

Mixed states: In the more general case, a closed system is not in a pure state, but in a mixed one, and it is characterized by its density operator $\hat{\rho}(t)$, which obeys the Liouville - von Neumann equation,

$$i\hbar\frac{d}{dt}\hat{\rho}(t) = [\hat{H}(t), \hat{\rho}(t)]\,. \tag{3.1.5}$$

Here, $[\hat{H}, \hat{\rho}]$ denotes the commutator $\hat{H}\hat{\rho} - \hat{\rho}\hat{H}$. The solution to this equation is given in terms of the same time evolution operator $\hat{U}(t, t_0)$ as in the pure-state case, Eq. (3.1.3), as

$$\hat{\rho}(t) = \hat{U}(t, t_0)\hat{\rho}(t_0)\hat{U}^\dagger(t, t_0)\,. \tag{3.1.6}$$

Notice that the Liouville - von Neumann equation (3.1.5) may be rephrased and expressed in analogy to the Schrödinger equation (3.1.1) (as well as the classical Liouville equation),[2]

$$i\hbar\frac{d}{dt}\hat{\rho}(t) = \hat{\hat{L}}(t)\hat{\rho}(t)\,. \tag{3.1.7}$$

Here, $\hat{\hat{L}}$ is the Liouvillian or Liouville super-operator, which is defined by its action as $\hat{\hat{L}}\hat{\rho} = [\hat{H}, \hat{\rho}]$. Also the solution to Eq. (3.1.5) can be expressed in terms of a super-operator,

$$\hat{\rho}(t) = \hat{\hat{U}}(t, t_0)\hat{\rho}(t_0)\,. \tag{3.1.8}$$

The time evolution super-operator $\hat{\hat{U}}$ acts as $\hat{\hat{U}}\hat{\rho} = \hat{U}\hat{\rho}\,\hat{U}^\dagger$. Alternatively, it can be defined, in analogy to the pure-state case, Eq. (3.1.3), as

$$\begin{aligned}\hat{\hat{U}}(t, t_0) &= \hat{\hat{T}}\exp\left[-\frac{i}{\hbar}\int_{t_0}^{t} \mathrm{d}\tau\,\hat{\hat{L}}(\tau)\right] \\ &\overset{\hat{\hat{L}}\neq\hat{\hat{L}}(\tau)}{=} \exp\left[-\frac{i}{\hbar}\hat{\hat{L}}(t - t_0)\right].\end{aligned} \tag{3.1.9}$$

[2] This is particularly useful for open quantum systems, which we study in the following.

$\hat{\hat{U}}$ is again unitary, $\hat{\hat{U}}^\dagger\hat{\hat{U}} = \hat{\hat{U}}\hat{\hat{U}}^\dagger = \hat{\hat{\mathbb{1}}}$, since the Liouvillian is Hermitian, $\hat{\hat{L}} = \hat{\hat{L}}^\dagger$. In this framework, time dependent expectation values of operators $\hat{O}$ are obtained as

$$\langle \hat{O}(t) \rangle = \mathrm{Tr}\left\{ \hat{\rho}(t)\hat{O} \right\} \ . \tag{3.1.10}$$

In summary, a closed quantum system always evolves unitarily in time. As discussed in the next section, this is, in general, not the case for open quantum systems. The representation in terms of super-operators is particularly useful for open systems, since it allows to map the problem to a standard operator problem, which is also discussed in the following sections.

3.2 Open quantum systems

A quantum system S is called *open*, if it is coupled to another quantum system E, with which it can exchange particles, energy, etc. In typical applications, the combined quantum system $U = S + E$ is considered to be closed, see Fig. 3.1. Therefore, E is usually termed *environment* and U *universe*.[3]

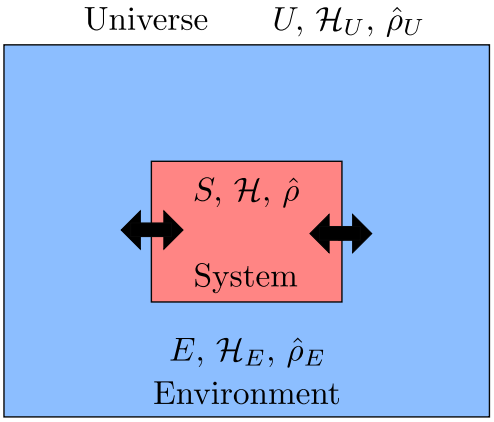

Figure 3.1: The open quantum system S and its environment E together constitute the closed universe $U = S + E$. The respective Hilbert spaces are denoted $\mathcal{H}$, $\mathcal{H}_E$ and $\mathcal{H}_U = \mathcal{H} \otimes \mathcal{H}_E$ and the density operators $\hat{\rho}$, $\hat{\rho}_E$ and $\hat{\rho}_U$. This illustration was adapted from [85].

[3] In principle, the roles of S and E could be exchanged. Here, we denote by S the part of the universe we are interested in and by E the rest we are not explicitly interested in.

The universe evolves unitarily in time, as summarized in the previous Sec. 3.1, due to the action of the Hamiltonian $\hat{H}_U$,

$$\hat{H}_U = \hat{H} \otimes \hat{\mathbb{1}}_E + \hat{\mathbb{1}} \otimes \hat{H}_E + \hat{H}_C \,. \tag{3.2.1}$$

The dynamics of the open system, on the other hand, is not solely governed by its Hamiltonian $\hat{H}$ - also the environment and the coupling to it, described by $\hat{H}_E$ and $\hat{H}_C$, contribute.

Formally, the time evolution of S may be obtained from the time evolution of U by taking the partial trace over E, such as the reduced density operator is obtained from the global one,

$$\hat{\rho} = \mathrm{Tr}_E \, \hat{\rho}_U(t) \,. \tag{3.2.2}$$

Under certain circumstances, this leads, applied to Eq. (3.1.8), to the definition of a dynamical map $\hat{V}(t, t_0)$ from the state space of reduced density operators of S onto itsself:[4]

$$\begin{array}{ccc} \hat{\rho}_U(t_0) = \hat{\rho}(t_0) \otimes \hat{\rho}_E(t_0) & \xrightarrow{\text{unitary evolution}} & \hat{\rho}_U(t) = \hat{\hat{U}}_U(t, t_0) \, [\hat{\rho}(t_0) \otimes \hat{\rho}_E(t_0)] \\ \Big\downarrow \mathrm{Tr}_E & & \Big\downarrow \mathrm{Tr}_E \\ \hat{\rho}(t_0) & \xrightarrow[\text{map}]{} & \hat{\rho}(t) = \hat{\hat{V}}(t, t_0) \, \hat{\rho}(t_0) \end{array} \tag{3.2.3}$$

The dynamical map $\hat{V}(t, t_0)$ is, in general, not unitary. Applying the partial trace also to the differential equation (3.1.7), its generator $\hat{\hat{L}}$ is deduced, which is, in general, not Hermitian:

$$\begin{array}{c} i\hbar \dfrac{d}{dt} \hat{\rho}_U(t) = \hat{\hat{L}}_U \hat{\rho}_U(t) \\ \Big\downarrow \mathrm{Tr}_E \\ i\hbar \dfrac{d}{dt} \hat{\rho}(t) = \hat{\hat{L}} \hat{\rho}(t) \end{array} \tag{3.2.4}$$

[4] We assumed U to be in a product state initially. Notice that, in general, $\hat{\hat{V}}$ is also dependent on $\hat{\rho}(t_0)$ and the reduced dynamics in Eq. (3.2.4) is not always local in time.

Summarizing, the time evolution of an open quantum system is generated by a non-Hermitian operator and is, therefore, non-unitary.

The final Eq. (3.2.4) is called *quantum master equation*. This is a first order differential equation for the reduced density operator of the open system, in terms of other system operators and with coefficients that depend on the environment and the coupling to it. It is analogous to the Schrödinger equation (3.1.1) or the Liouville - von Neumann equation (3.1.5) that are valid for closed quantum systems.

In general, the outlined derivation is not carried out in practice. Computing the time evolution of the universe is usually not feasible and we are only interested in the reduced system dynamics, anyway. For some cases, a master equation can be derived exactly, mostly, it is an approximation. Depending on the assumptions that have been made, there are different types of master equations. One of them is the *Lindblad master equation*, which is discussed in the next section and which we employ in the auxiliary master equation approach.

3.2.1 Lindblad master equation

The Lindblad master equation is the most general quantum master equation that is local in time,[5] has constant coefficients and preserves the defining properties of the density operator [87, 88].[6] It has the following form,

$$i\hbar\frac{d}{dt}\hat{\rho}(t) = [\hat{H}, \hat{\rho}(t)] + i\sum_{ij}\gamma_{ij}\left[2\hat{M}_i\,\hat{\rho}(t)\hat{M}_j^\dagger - \left\{\hat{M}_j^\dagger\hat{M}_i\,, \hat{\rho}(t)\right\}\right]. \qquad (3.2.5)$$

$\hat{H}$ comprises the closed-system Hamiltonian and, potentially, additional Hermitian terms produced by the coupling to the environment. The Lindblad operators $\hat{M}_i$ and the dampening matrix $\boldsymbol{\gamma}$ depend on the nature of environment and the coupling. $\left\{\hat{M}_j^\dagger\hat{M}_i\,, \hat{\rho}\right\}$ means the anticommutator $\hat{M}_j^\dagger\hat{M}_i\,\hat{\rho} + \hat{\rho}\,\hat{M}_j^\dagger\hat{M}_i$.

[5] This means that $\hat{\rho}(t+dt)$ depends on $\hat{\rho}(t)$, but is independent of states that lie farther in the past, so the system has no memory.

[6] These are Hermiticity, $\hat{\rho} = \hat{\rho}^\dagger$, normalization, $\mathrm{Tr}\,\hat{\rho} = 1$ and positive semidefiniteness, $\langle\psi|\,\hat{\rho}\,|\psi\rangle \geq 0$ for all $|\psi\rangle \in \mathcal{H}$ (in fact, complete positiveness).

$\hat{H}$ and $\boldsymbol{\gamma}$ have the following properties,

$$\begin{aligned} \hat{H} &= \hat{H}^\dagger \,, \\ \boldsymbol{\gamma} = \boldsymbol{\gamma}^\dagger \quad &\text{and} \quad \boldsymbol{v}^\dagger \boldsymbol{\gamma} \boldsymbol{v} \geq 0 \,, \end{aligned} \tag{3.2.6}$$

for all vectors $\boldsymbol{v}$. Expressing the Lindblad equation in terms of super-operators, as suggested in the previous section, we can distinguish two fundamentally different contributions to the Liouvillian:

$$\begin{aligned} \hat{\hat{L}} &= \hat{\hat{L}}_H + \hat{\hat{L}}_D \\ \hat{\hat{L}}_H \ \hat{\rho}(t) &= [\hat{H}, \hat{\rho}(t)] \\ \hat{\hat{L}}_D \ \hat{\rho}(t) &= i \sum_{ij} \gamma_{ij} \left[2\hat{M}_i \, \hat{\rho}(t) \hat{M}_j^\dagger - \left\{ \hat{M}_j^\dagger \hat{M}_i \, , \hat{\rho}(t) \right\} \right] \end{aligned} \tag{3.2.7}$$

$\hat{\hat{L}}_H$ generates a unitary propagation in time, such as in a closed system,[7] whereas $\hat{\hat{L}}_D$ has no closed-system analogue. This super-operator accounts for the dissipation, due to the coupling to the environment. Since $\hat{\hat{L}}_D$ is not Hermitian, it generates a non-unitary propagation in time. As a consequence, the overall time evolution[8] is non-unitary:

$$\begin{aligned} \hat{\hat{L}} &\neq \hat{\hat{L}}^\dagger \\ \hat{\hat{V}}^{-1} &\neq \hat{\hat{V}}\dagger \end{aligned} \tag{3.2.8}$$

3.3 Auxiliary Master Equation Approach

In this section, the basic idea of the auxiliary master equation approach is outlined. This approach has been developed in our working group, particularly, to deal with impurity problems, such as the Anderson impurity model, out of equilibrium, i.e. under the influence of a bias voltage. However, it can also be applied to the more general setup of a small central region, such as a molecule or several impurities, that is attached to one or more baths.

[7] It is the generator of a Liouville - von Neumann equation (3.1.5).

[8] determined from Eq. (3.1.9) changing the label $\hat{\hat{U}}$ to $\hat{\hat{V}}$

In contrast to conventional approaches based on a perturbative derivation of the master equation, in AMEA, the general form of a master equation is obtained by requiring that its parameters meet certain conditions. This will be explained in the following. In Fig. 3.2, the setup we investigate in Refs. [1, 3], Chs. 5 and 6, is sketched, an Anderson impurity model with a bias voltage applied, realized by a difference in the chemical potentials of a left (μ_L) and a right (μ_R) bath. The baths are also called leads in this context.

Fig. 3.2(a) shows the impurity site surrounded by a bath of conduction electrons illustrated as a cloud. In Fig. 3.2(b), the bath is split to be allocated to a left and a right lead at potentially different chemical potentials. For simplicity, the left and right lead are illustrated as two semi-infinite chains of bath sites. Roughly, this is also the setup studied in Chs. 5 and 6. However, more general geometries, with more general couplings between the bath sites, are conceivable. Since this impurity problem has an infinitely large state space, it cannot be solved exactly. As a first approximation, one can cut out a finite system, which is small enough such that the solution of the corresponding Schrödinger equation (3.1.1) or Liouville - von Neumann equation (3.1.5) is feasible in practice. This is sketched in Fig. 3.2(c). However, at some instant in time, an electron propagating towards the system boundary will be reflected introducing artificial finite-size effects. As a consequence, in such a setup, we will always observe oscillating behavior and a true steady state will never be reached. In order to simulate a genuine nonequilibrium system with a true steady state, we need to implement absorbing boundary conditions. They allow electrons to jump out of the system and vanish into the surrounding environment and vice versa. One way to implement absorbing boundary conditions is by attaching Markovian baths, as illustrated by the clouds in Fig. 3.2(d). Markovian means that the bath loses its memory immediately. Such a behavior is captured by a master equation that is local in time. In AMEA, we employ the Lindblad equation (3.2.5) for this purpose.

In summary, we map the *physical* impurity problem, Fig. 3.2(a) and (b), to the finite problem with Markovian baths (d) which is termed *auxiliary* impurity problem and whose dynamics is governed by a Lindblad equation. This is done by presuming a general Lindblad equation, whose parameters,

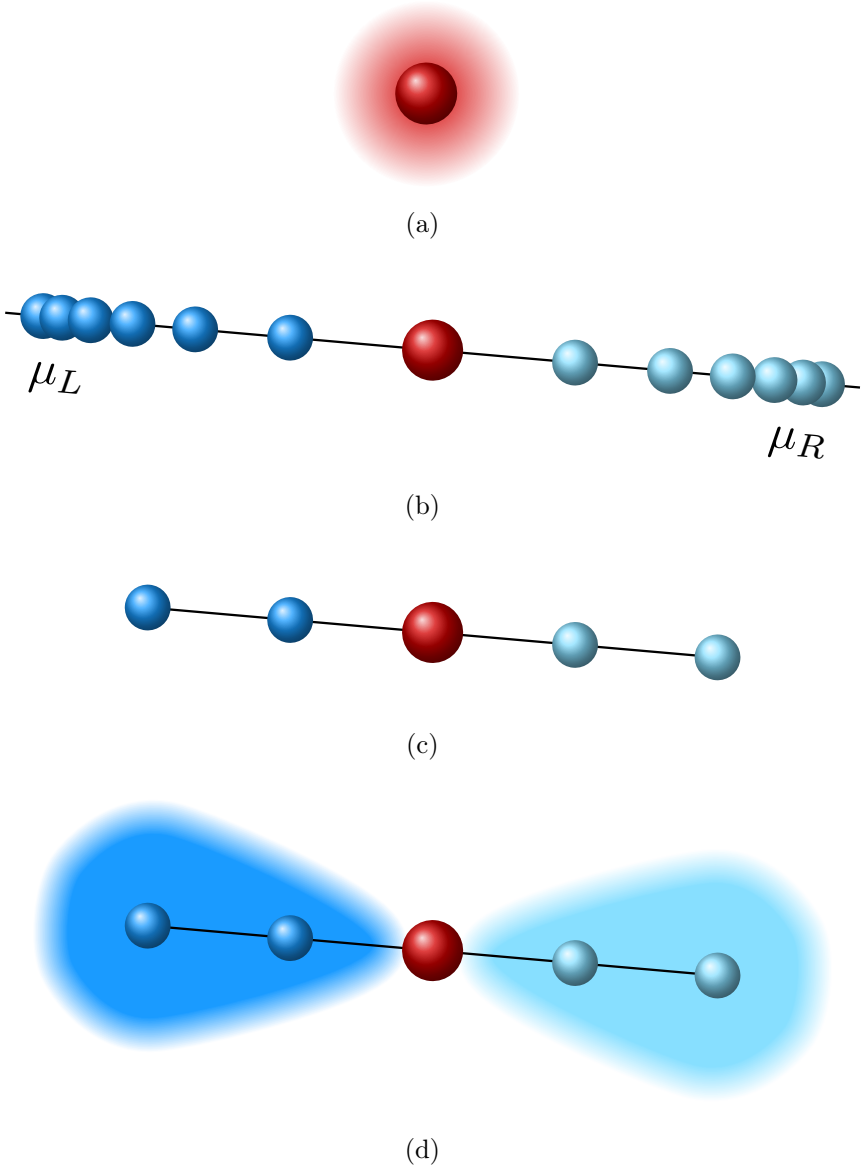

Figure 3.2: Idea of AMEA sketched at the example of the Anderson impurity model. The impurity, represented as a red circle, is in a bath of conduction electrons (a) loosely illustrated as a cloud and (b) represented as two semi-infinite chains of bath sites. They can have different chemical potentials μ_α realizing a nonequilibrium situation. This physical system is too large to solve. Thus, (c) it is truncated and (d) Markovian baths are attached to remove finite-size effects. The auxiliary system obeys a Lindblad equation, whose parameters are fitted to approximate the hybridization function of (b).

i.e. the dampening matrix as well as energies and hoppings in the baths and to/from the central region,[9] are obtained from a fit. They are determined such that the hybridization function of the auxiliary system matches the physical one as well as possible. In particular, the fit involves the retarded and the Keldysh component of the hybridization function,[10] which define the leads' density of states as well as their particle distribution function, i.e. the Fermi function for the problems considered here. The hybridization function describes the influence of the baths on the impurity or central region completely.[11] Being interested only in the physics of the central region and not in the baths, any transformation on the baths that preserves the hybridization function and the properties of the Lindblad equation is a valid transformation that leads to the same physics. For mathematical details, we refer to Sec. 3.5 as well as Secs. 5.3.3, 6.3.3.1, 6.3.3.2 and Refs. [63, 83].

After the mapping, the resulting Lindblad equation has to be solved. In this thesis, we rely on matrix product states techniques, see Sec. 4.5 as well as Secs. 5.3.3, 6.3.3.3 and Ref. [64], combined with the super-fermion representation, which is discussed in the next Sec. 3.4 as well as Ref. [86]. Alternative methods employed by our group operate in Krylov space [63] or are based on a stochastic evolution of the wave function [2, 89]. The central quantity we are interested in is the Green's function. This is the response function to the Schrödinger equation in case of a closed system and to the Lindblad equation in the discussed auxiliary open system. From the Green's function, several interesting quantities may be accessed, the spectral function (local density of states) at the impurity, the current, differential conductance, nonequilibrium distribution functions, etc. For an overview, see Secs. 5.3.2 and 6.3.2 in the present work and for details Refs. [90, 91].

[9] degrees of freedom of the leads and the coupling, excluding the central region
[10] see Secs. 5.3.2 and 6.3.2
[11] see Dyson's equation (5.3.11)

3.4 Super-fermion representation

The idea of the super-fermion representation is to rephrase a super-operator problem, such as Eq. (3.2.7), such that it turns into an ordinary operator problem in an augmented state space. The advantage of this is that standard many-body methods can be employed to solve the problem.

The procedure is as follows [86]: If the Hilbert space of the open system $\mathcal{H}$ is defined by a complete set of orthonormal states $|n\rangle$, then a second Hilbert space $\tilde{\mathcal{H}}$ is introduced, which is an identical copy of $\mathcal{H}$ and which is defined by the states $|\tilde{n}\rangle$:

$$\begin{aligned} \sum_n |n\rangle\langle n| &= \hat{\mathbb{1}}\,, \quad \langle n|m\rangle = \delta_{nm} \\ \sum_n |\tilde{n}\rangle\langle \tilde{n}| &= \hat{\tilde{\mathbb{1}}}\,, \quad \langle \tilde{n}|\tilde{m}\rangle = \delta_{nm} \end{aligned} \tag{3.4.1}$$

Consequently, the augmented state space $\mathcal{H} \otimes \tilde{\mathcal{H}}$ is spanned by the product states $|n\rangle \otimes |\tilde{m}\rangle$. In this augmented state space, it is useful to define the left vacuum vector $|I\rangle$ as well as the nonequilibrium wave function $|\rho\rangle = \hat{\rho}\,|I\rangle$, as

$$|I\rangle = \sum_n |n\rangle \otimes |\tilde{n}\rangle\ , \tag{3.4.2}$$

$$|\rho(t)\rangle = \sum_{nm} \rho_{nm}(t)\,|n\rangle \otimes |\tilde{m}\rangle\ , \tag{3.4.3}$$

with $\rho_{nm}(t) = \langle n|\hat{\rho}(t)|m\rangle$. The left vacuum $|I\rangle$ corresponds to the identity operator $\hat{\mathbb{1}}$ with the bra-vector $\langle n|$ exchanged by a ket-vector $|\tilde{n}\rangle$ in the additional state space $\tilde{\mathcal{H}}$. Essentially the same is valid for $|\rho\rangle$ and $\hat{\rho}$. Applying the whole differential equation (3.2.7) to $|I\rangle$,

$$i\frac{d}{dt}\,|\rho(t)\rangle = \hat{L}\,|\rho(t)\rangle\ , \tag{3.4.4}$$

yields a Schrödinger - like equation with the ordinary, but non-Hermitian, operator $\hat{L}$ acting as Hamiltonian, $\hat{L}\,|\rho(t)\rangle = \left[\hat{\hat{L}}\hat{\rho}\right]|I\rangle$, in the augmented

state space. In this framework, expectation values (3.1.10) are obtained as

$$\langle \hat{O}(t) \rangle = \langle I \,|\, \hat{O} \,|\, \rho(t) \rangle \ . \tag{3.4.5}$$

From the normalization constraint of the density operator, $\mathrm{Tr}\, \hat{\rho}(t) = 1$, follows that $\langle I|\rho(t)\rangle = 1$ must be fulfilled at any time. Further, applying $\langle I|$ to Eq. (3.4.4) from the left, past the derivative, leads to[12]

$$\langle I| \, \hat{L} = 0 \ . \tag{3.4.6}$$

So, $\langle I|$ is a left eigenvector of $\hat{L}$ to the eigenvalue 0. In the steady state, $|\rho_\infty\rangle = \lim_{t\to\infty} |\rho(t)\rangle$ does not depend on time anymore, and Eq. (3.4.4) yields

$$\hat{L} \, |\rho_\infty\rangle = 0 \, . \tag{3.4.7}$$

So, the steady state $|\rho_\infty\rangle$ is a right eigenvector of $\hat{L}$ to the eigenvalue 0. As a consequence, the problem of finding the steady state can be reduced to the problem of determining this eigenvector.

3.5 Basis of this work

Following Ref. [86], we now show, how to bridge the gap between the general form of the Lindblad equation (3.2.5) and the super-fermion representation, Sec. 3.4, to the equations in Sec. 6.3.3.1 for the auxiliary system in case of the Anderson impurity model, which are used in Ch. 6, of course, but also in Ch. 5. For the sake of readability, we omit hats and double hats for operators and super-operators, here as well as in Chs. 5, 6, while they are employed everywhere else in this thesis.

Auxiliary impurity problem: We start by splitting the Hamiltonian of the auxiliary system, introduced in Sec. 3.3, into three contributions arising

[12] since $\langle I|\hat{L}|\rho(t)\rangle = 0$ at any time

from the impurity, the leads and the coupling between them,

$$H = H_{\text{imp}} + H_{\text{leads}} + H_{\text{coup}} \,. \tag{3.5.1}$$

Assuming interactions to be confined to the impurity, we set up for the rest of the system a general noninteracting Hamiltonian,

$$H_{\text{leads}} + H_{\text{coup}} = \sum_{\substack{\mu\nu\sigma \\ \{\text{leads, coup}\}}} E_{\mu\nu} c^\dagger_{\mu\sigma} c_{\nu\sigma} \,. \tag{3.5.2}$$

The operator $c^{(\dagger)}_{\mu\sigma}$ creates (annihilates) an electron with spin σ at auxiliary system site μ. Further, in AMEA, we consider only Lindblad operators that are linear in these creation and annihilation operators,

$$\begin{aligned} M^\dagger_j &= \left(\boldsymbol{c}^\dagger_\downarrow, \boldsymbol{c}^\dagger_\uparrow, \boldsymbol{c}_\downarrow, \boldsymbol{c}_\uparrow \right)_j \,, \\ \gamma_{ij} &= \text{diag}\left(\boldsymbol{\Gamma}^{(1)T}, \boldsymbol{\Gamma}^{(1)T}, \boldsymbol{\Gamma}^{(2)}, \boldsymbol{\Gamma}^{(2)} \right)_{ij} \,, \end{aligned} \tag{3.5.3}$$

where $\boldsymbol{c}^\dagger_\sigma = \left(c^\dagger_{1\sigma}, c^\dagger_{2\sigma}, \dots \right)$ runs over the leads' degrees of freedom and $\left(\boldsymbol{\Gamma}^{(1)T} \right)_{\mu\nu} = \Gamma^{(1)}_{\nu\mu}$ is the transpose. Entering Eqs. (3.5.2) and (3.5.3) into the Lindblad equation (3.2.5), we obtain:

$$\begin{aligned} i\hbar \frac{d}{dt} \rho(t) = &[H_{\text{imp}}, \rho(t)] \\ &+ \sum_{\substack{\mu\nu\sigma \\ \{\text{leads, coup}\}}} E_{\mu\nu} [c^\dagger_{\mu\sigma} c_{\nu\sigma}, \rho(t)] \\ &+ i \sum_{\substack{\mu\nu\sigma \\ \{\text{leads}\}}} \Gamma^{(1)}_{\mu\nu} \left[2 c_{\nu\sigma} \rho(t) c^\dagger_{\mu\sigma} - \left\{ c^\dagger_{\mu\sigma} c_{\nu\sigma}, \rho(t) \right\} \right] \\ &+ i \sum_{\substack{\mu\nu\sigma \\ \{\text{leads}\}}} \Gamma^{(2)}_{\mu\nu} \left[2 c^\dagger_{\mu\sigma} \rho(t) c_{\nu\sigma} - \left\{ c_{\nu\sigma} c^\dagger_{\mu\sigma}, \rho(t) \right\} \right] \end{aligned} \tag{3.5.4}$$

The matrices $\boldsymbol{E}$, $\boldsymbol{\Gamma}^{(1)}$ and $\boldsymbol{\Gamma}^{(2)}$ hold the parameters to be determined by a fit, as discussed in Sec. 3.3. $\boldsymbol{\Gamma}^{(\alpha)}$ is Hermitian and positive semidefinite and

$\boldsymbol{E}$ is Hermitian.[13] Further, for a solution of the auxiliary impurity problem with MPS, we restrict them all to be tridiagonal.[14]

Super-fermions: For a fermionic many-body system, such as the Anderson impurity model, the Hilbert space is a Fock space and the particle number representation is useful. We chose the left vacuum (3.4.2), without exactly specifying the ordering of states at this point,[15] as

$$\begin{aligned} |I\rangle &= \sum_{\{n_{\mu\sigma}\}} \bigotimes_{\mu\sigma} (-i)^{n_{\mu\sigma}} |n_{\mu\sigma}\rangle \otimes |\tilde{n}_{\mu\sigma}\rangle \\ &= \sum_{n_{1\downarrow}\dots n_{N\uparrow}} (-i)^{n_{1\downarrow}+\dots+n_{N\uparrow}} |n_{1\downarrow}\tilde{n}_{1\downarrow}\dots n_{N\uparrow}\tilde{n}_{N\uparrow}\rangle \\ &= \sum_{n_{1\downarrow}\dots n_{N\uparrow}} (-i)^{n_{1\downarrow}+\dots+n_{N\uparrow}} \left(c^\dagger_{1\downarrow}\tilde{c}^\dagger_{1\downarrow}\right)^{n_{1\downarrow}} \dots \left(c^\dagger_{N\uparrow}\tilde{c}^\dagger_{N\uparrow}\right)^{n_{N\uparrow}} |0\rangle \otimes |\tilde{0}\rangle \end{aligned} \tag{3.5.5}$$

One exploits the possibility to introduce an additional phase, $(-i)^{n_1+n_2+\dots+n_N}$, here, which turns out to be convenient for fermions. Since the very same phase enters also $|\rho\rangle$, expectation values (3.4.5) are not affected by this move. $n_{\mu\sigma}$ is the number of particles in state μ with spin σ,

$$\begin{aligned} c^\dagger_{\mu\sigma}c_{\mu\sigma}\,|\dots n_{\mu\sigma}\dots\rangle &= n_{\mu\sigma}\,|\dots n_{\mu\sigma}\dots\rangle\ , \\ \tilde{c}^\dagger_{\mu\sigma}\tilde{c}_{\mu\sigma}\,|\dots \tilde{n}_{\mu\sigma}\dots\rangle &= n_{\mu\sigma}\,|\dots \tilde{n}_{\mu\sigma}\dots\rangle\ , \end{aligned} \tag{3.5.6}$$

and the tilde operators refer to the additional Hilbert space $\tilde{\mathcal{H}}$. The ordinary fermionic anticommutation rules are fulfilled and, further, operators in different Fock spaces $\mathcal{H}$ and $\tilde{\mathcal{H}}$ anticommute:

$$\begin{aligned} &\{c_{\mu\sigma}, c^\dagger_{\nu\upsilon}\} = \{\tilde{c}_{\mu\sigma}, \tilde{c}^\dagger_{\nu\upsilon}\} = \delta_{\mu\nu}\delta_{\sigma\upsilon} \\ &\{c_{\mu\sigma}, c_{\nu\upsilon}\} = \{c^\dagger_{\mu\sigma}, c^\dagger_{\nu\upsilon}\} = \{\tilde{c}_{\mu\sigma}, \tilde{c}_{\nu\upsilon}\} = \{\tilde{c}^\dagger_{\mu\sigma}, \tilde{c}^\dagger_{\nu\upsilon}\} = \{c^{(\dagger)}_{\mu\sigma}, \tilde{c}^{(\dagger)}_{\nu\upsilon}\} = 0 \end{aligned} \tag{3.5.7}$$

[13] These properties are inherited from $\boldsymbol{\gamma}$ and H, see Eq. (3.2.6).
[14] Notice that one of the matrices can always be chosen tridiagonal.
[15] corresponding non-tilde and tilde states are next to each other

In this representation also the so-called the *tilde conjugation rules* are valid,[16] which constitute a useful tool for calculating expectation values, since they allow to switch between operators in the non-tilde and the tilde state space:

$$\begin{aligned} c_{\mu\sigma} |I\rangle &= -i\tilde{c}^\dagger_{\mu\sigma} |I\rangle \\ c^\dagger_{\mu\sigma} |I\rangle &= -i\tilde{c}_{\mu\sigma} |I\rangle \end{aligned} \tag{3.5.8}$$

Applying the Lindblad equation (3.5.4) to the left vacuum (3.5.5), yields, with the anticommutation and tilde conjugation rules, the following equation in super-fermion representation:

$$\begin{aligned} i\hbar \frac{d}{dt} |\rho(t)\rangle = &\left[H_{\text{imp}} - \tilde{H}_{\text{imp}}\right] |\rho(t)\rangle \\ &+ \sum_{\substack{\mu\nu\sigma \\ \{\text{leads, coup}\}}} E_{\mu\nu} \left[c^\dagger_{\mu\sigma} c_{\nu\sigma} + \tilde{c}_{\mu\sigma} \tilde{c}^\dagger_{\nu\sigma} - \delta_{\mu\nu}\right] |\rho(t)\rangle \\ &+ \sum_{\substack{\mu\nu\sigma \\ \{\text{leads}\}}} \Gamma^{(1)}_{\mu\nu} \left[-2\tilde{c}_{\mu\sigma} c_{\nu\sigma} - i c^\dagger_{\mu\sigma} c_{\nu\sigma} + i\tilde{c}_{\mu\sigma} \tilde{c}^\dagger_{\nu\sigma} - i\delta_{\mu\nu}\right] |\rho(t)\rangle \\ &+ \sum_{\substack{\mu\nu\sigma \\ \{\text{leads}\}}} \Gamma^{(2)}_{\mu\nu} \left[2c^\dagger_{\mu\sigma} \tilde{c}^\dagger_{\nu\sigma} + i c^\dagger_{\mu\sigma} c_{\nu\sigma} - i\tilde{c}_{\mu\sigma} \tilde{c}^\dagger_{\nu\sigma} - i\delta_{\mu\nu}\right] |\rho(t)\rangle \end{aligned} \tag{3.5.9}$$

For the Anderson impurity model, $\tilde{H}_{\text{imp}}$ has exactly the same structure as H_{imp}, Eq. (5.3.2) or (6.3.2), but with tilde operators instead of non-tilde ones. This is, because H_{imp} contains only particle number operators (3.5.6). Collecting terms and comparing with (3.4.4), one obtains the Liouvillian:

$$\begin{aligned} L &= L_0 + L_U \\ L_0 &= \sum_{\mu\nu\sigma} \left[\left(E_{\mu\nu} + i\Omega_{\mu\nu}\right) c^\dagger_{\mu\sigma} c_{\nu\sigma} + \left(E_{\mu\nu} - i\Omega_{\mu\nu}\right) \tilde{c}_{\mu\sigma} \tilde{c}^\dagger_{\nu\sigma}\right] \\ &\quad + \sum_{\mu\nu\sigma} \left[2\Gamma^{(2)}_{\mu\nu} c^\dagger_{\mu\sigma} \tilde{c}^\dagger_{\nu\sigma} - 2\Gamma^{(1)}_{\mu\nu} \tilde{c}_{\mu\sigma} c_{\nu\sigma}\right] - 2\,\text{Tr}\left[\boldsymbol{E} + i\boldsymbol{\Lambda}\right] \\ L_U &= U\left[n_{f\uparrow} n_{f\downarrow} - \tilde{n}_{f\uparrow} \tilde{n}_{f\downarrow}\right] \end{aligned} \tag{3.5.10}$$

[16] since corresponding non-tilde and tilde operators come in pairs in Eq. (3.5.5)

In order to arrive at Eq. (3.5.10), we also shifted the noninteracting terms of $H_{\text{imp}} - \tilde{H}_{\text{imp}}$, i.e. coefficients $\varepsilon_{f\sigma}$, where f denotes the impurity site, to the matrix $\boldsymbol{E}$. In this way, L is split into an interacting and a noninteracting part, L_U and L_0. We further defined $\boldsymbol{\Omega} = \boldsymbol{\Gamma}^{(2)} - \boldsymbol{\Gamma}^{(1)}$ and $\boldsymbol{\Lambda} = \boldsymbol{\Gamma}^{(2)} + \boldsymbol{\Gamma}^{(1)}$.

Carrying out a particle-hole transformation $\tilde{c}^{\dagger}_{\mu\sigma} \leftrightarrow \tilde{c}_{\mu\sigma}$ in Eq. (3.5.10) and redefining $L \to iL$[17] we arrive at Eq. (6.3.17) for the Liouvillian with the corresponding left vacuum Eq. (6.3.21).

[17] We defined L in Eq. (3.1.7) and (3.2.7) without the prefactor i for a closer analogy to the Schrödinger equation (3.1.1) and for a better understanding of the derived properties.

Chapter 4

Matrix Product States

This chapter constitutes an introduction to the matrix product states (MPS) formalism, which we employ to solve the Lindblad equation resulting from the auxiliary master equation approach to the Anderson impurity model out of equilibrium, Refs. [1, 3], Chs. 5 and 6. Whereas MPS are mostly renowned for representing ground states of one-dimensional gapped closed systems efficiently, the formalism turns out to work well also for steady states and steady state correlation functions of the open systems studied here.

Following a review by Schollwöck, Ref. [92], we start this introduction with the singular value decomposition (SVD), which forms the core of almost any operation on MPS, Sec. 4.1. We proceed by exactly deriving canonical forms of matrix product states in Sec. 4.2 and discuss their truncation and the MPS approximation in Sec. 4.3. In Sec. 4.4, matrix product operators (MPOs) are introduced. Sec. 4.5 deals with the time evolution of a system based on MPS, starting with a decomposition of the generator into commuting terms in Sec. 4.5.1 and the definition of gates in Sec. 4.5.2. Then the two main algorithms for the time evolution are introduced, the time-dependent density-matrix renormalization group (tDMRG) algorithm, Sec. 4.5.3, and the time-evolving block decimation (TEBD) algorithm, Sec. 4.5.4. These algorithms are compared in Sec. 4.5.5. Finally, particularities of the implementations for Refs. [1, 3] are discussed in Sec. 4.6.

4.1 Singular Value Decomposition

Working with matrix product states, a very useful tool, which is central to many important manipulations, is the singular value decomposition: Any arbitrary $N_A \times N_B$ matrix $\boldsymbol{M}$ may be decomposed as

$$\boldsymbol{M} = \boldsymbol{U}\boldsymbol{\Lambda}\boldsymbol{V}^\dagger\,, \tag{4.1.1}$$

where the new matrices $\boldsymbol{U}$, $\boldsymbol{\Lambda}$ and $\boldsymbol{V}^\dagger$ arising in this decomposition have the following properties (a sketch is also provided in Fig. 4.1):

- $\boldsymbol{U}$ is an $N_A \times N$ matrix, where $N = \min(N_A, N_B)$, with orthonormal columns, $\boldsymbol{U}^\dagger\boldsymbol{U} = \mathbb{1}$, which are called *left singular vectors*. If $N_A \leq N_B$, $\boldsymbol{U}$ is unitary and, therefore, also $\boldsymbol{U}\boldsymbol{U}^\dagger = \mathbb{1}$ is valid.

- $\boldsymbol{V}^\dagger$ is an $N \times N_B$ matrix with orthonormal rows, $\boldsymbol{V}^\dagger\boldsymbol{V} = \mathbb{1}$, which are analogously called *right singular vectors*. If $N_A \geq N_B$, the matrix $\boldsymbol{V}^\dagger$ is further unitary, fulfilling also $\boldsymbol{V}\boldsymbol{V}^\dagger = \mathbb{1}$.

- $\boldsymbol{\Lambda}$ is a diagonal $N \times N$ matrix with non-negative entries $\Lambda_{aa} \equiv \lambda_a \geq 0$, which are called *singular values*. We assume them to be arranged in descending order. The number r of non-zero singular values, $\lambda_1 \geq \lambda_2 \geq \ldots \geq \lambda_r > 0$, is the *rank* or *Schmidt rank* of $\boldsymbol{M}$.

One application of the SVD, which is of utmost interest, is the approximation of a matrix $\boldsymbol{M}$ of rank r by another matrix $\boldsymbol{M}'$ that has a smaller rank $r' < r$. Based on the Frobenius norm,[1] $\|\boldsymbol{M}\|_F = \mathrm{Tr}\left\{\boldsymbol{M}^\dagger\boldsymbol{M}\right\}$, the optimal solution to this problem is

$$\begin{aligned} \boldsymbol{M}' &= \boldsymbol{U}\boldsymbol{\Lambda}'\boldsymbol{V}^\dagger \\ \boldsymbol{\Lambda}' &= \mathrm{diag}\,(\lambda_1, \lambda_2, \ldots \lambda_{r'}, 0, \ldots 0) \end{aligned} \tag{4.1.2}$$

with the same matrices $\boldsymbol{U}$ and $\boldsymbol{V}^\dagger$ as in Eq. (4.1.1). Notice that the new matrix $\boldsymbol{\Lambda}'$ contains only the r' largest singular values. So, in practice, one

[1] which naturally extends the 2-norm of vectors

can reduce $\boldsymbol{U}$ to the first r' columns, $\boldsymbol{V}^\dagger$ to the first r' rows and $\boldsymbol{\Lambda}$ to the first r' diagonal entries, as an approximation.

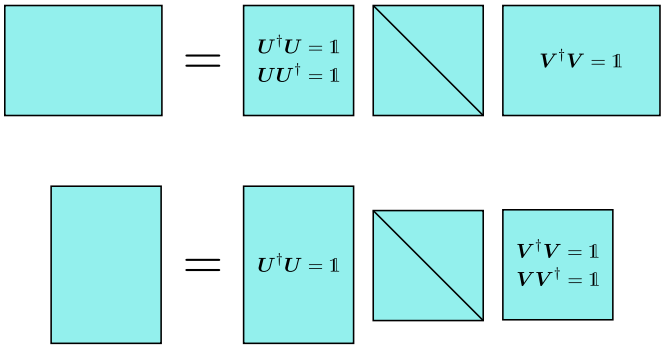

Figure 4.1: Sketch of the matrix shapes in an SVD for $N_A < N_B$ (top) and $N_A > N_B$ (bottom), adapted from [92].

4.2 Derivation of canonical forms

Here, we consider a lattice of L sites.[2] The local Hilbert space is of dimension d and it is spanned by the states $|s_l\rangle$ for $l = 1, \ldots, L$. Let $|\psi\rangle$ be a normalized pure state of this system. It can be expanded as

$$|\psi\rangle = \sum_{s_1,\ldots,s_L} c_{s_1,\ldots,s_L} |s_1, \ldots, s_L\rangle \ . \tag{4.2.1}$$

In the following, we will show, how to turn this state into an MPS, i.e. how to express the expansion coefficients $c_{s_1,\ldots,s_L}$ as products of local matrices,

$$c_{s_1,\ldots,s_L} = \boldsymbol{M}^{s_1}\boldsymbol{M}^{s_2}\ldots\boldsymbol{M}^{s_{L-1}}\boldsymbol{M}^{s_L} \ . \tag{4.2.2}$$

This seems to be cumbersome at first, but it has the advantage that the matrices $\boldsymbol{M}^{s_l}$ are local,[3] as indicated by the index l, allowing very efficient algorithms to be formulated for the time evolution.

[2] It does not have to be one-dimensional, but in practice, calculations based on an MPS representation become infeasible in higher dimensions.

[3] Notice that changing a local matrix nevertheless causes a global change of the state.

4.2.1 Left-canonical form

In order to derive an MPS representation, let us first note that the coefficients $c_{s_1,\ldots,s_L}$ are commonly interpreted as entries of a vector. To emphasize that, we change the notation and set, what we lay out as column or row degrees of freedom of a matrix, between brackets, e.g. $c_{(1),(s_1,\ldots,s_L)}$ for a row vector. Of course, we have the freedom to choose a more general matrix shape, as well, such as $c_{(s_1),(s_2,\ldots,s_L)}$, which is obtained from the previous representation by regrouping the first-site indices. This is the first step in the construction of an MPS, which is outlined in Eq. (4.2.6). Next, a singular value decomposition (4.1.1) is performed, the resulting $\boldsymbol{U}$ is split into d row vectors $\boldsymbol{A}^{s_1}$ of dimension r_1 (the corresponding Schmidt rank) and $\boldsymbol{\Lambda}\boldsymbol{V}^\dagger$ is multiplied to give the residual coefficient matrix $c_{(a_1),(s_2,\ldots,s_L)}$. We again reshape this coefficient matrix by regrouping the second-site indices to $c_{(a_1,s_2),(s_3,\ldots,s_L)}$ and subject it to an SVD. Again, d matrices $\boldsymbol{A}^{s_2}$ of dimension $r_1 \times r_2$ are extracted from $\boldsymbol{U}$ and $\boldsymbol{\Lambda}\boldsymbol{V}^\dagger$ is multiplied to become the new residual coefficient matrix. Performing this procedure for all lattice sites yields

$$c_{s_1,\ldots,s_L} = \boldsymbol{A}^{s_1}\boldsymbol{A}^{s_2}\ldots\boldsymbol{A}^{s_{L-1}}\boldsymbol{A}^{s_L}\,. \tag{4.2.3}$$

This is an exact representation of (4.2.1) as a matrix product state. Since the matrices $\boldsymbol{A}^{s_l}$ are derived from the $\boldsymbol{U}$s of the SVD, which fulfill $\boldsymbol{U}^\dagger\boldsymbol{U} = \mathbb{1}$, they have the property

$$\sum_{s_l} \boldsymbol{A}^{s_l\dagger}\boldsymbol{A}^{s_l} = \mathbb{1}\,, \tag{4.2.4}$$

which we call *left-normalized*. Matrix product states consisting only of left-normalized matrices, such as Eq. (4.2.3), are called *left-canonical*.

For even L, these matrices have at most the following dimensions, from the left to the right,

$$1\times d,\ d\times d^2,\ldots,\ d^{\frac{L}{2}-1}\times d^{\frac{L}{2}},\ d^{\frac{L}{2}}\times d^{\frac{L}{2}-1},\ldots,\ d^2\times d,\ d\times 1 \tag{4.2.5}$$

So, an exponentially large *bond dimension* of $d^{\frac{L}{2}}$ can be reached in the center of the MPS. Maximal values only occur, if all singular values are non-zero.

Derivation of a left-canonical MPS:

$$
\begin{aligned}
& & & & & & & & [1\times d^L] \\
& c_{s_1,\ldots,s_L} & = & & c_{(1),(s_1,\ldots,s_L)} & & & & \\
& \underbrace{c_{(s_1),(s_2,\ldots,s_L)}}_{[d\times d^{L-1}]} & = & \sum_{a_1}^{r_1} & \underbrace{U_{(s_1),(a_1)}}_{[d\times r_1]} & \underbrace{\lambda_{a_1} V^\dagger_{(a_1),(s_2,\ldots,s_L)}}_{[r_1\times d^{L-1}]} & & \\
& & & & \to A^{s_1}_{1,a_1} & = c_{(a_1),(s_2,\ldots,s_L)} & & \\
& \underbrace{c_{(a_1,s_2),(s_3,\ldots,s_L)}}_{[r_1 d\times d^{L-2}]} & = & \sum_{a_2}^{r_2} & \underbrace{U_{(a_1,s_2),(a_2)}}_{[r_1 d\times r_2]} & \underbrace{\lambda_{a_2} V^\dagger_{(a_2),(s_3,\ldots,s_L)}}_{[r_2\times d^{L-2}]} & & \\
& & & & \to A^{s_2}_{a_1,a_2} & = c_{(a_2),(s_3,\ldots,s_L)} & & \\
& \underbrace{c_{(a_2,s_3),(s_4,\ldots,s_L)}}_{[r_2 d\times d^{L-3}]} & = & \sum_{a_3}^{r_3} & \underbrace{U_{(a_2,s_3),(a_3)}}_{[r_2 d\times r_3]} & \underbrace{\lambda_{a_3} V^\dagger_{(a_3),(s_4,\ldots,s_L)}}_{[r_3\times d^{L-3}]} & & \\
& & & & \to A^{s_3}_{a_2,a_3} & = c_{(a_3),(s_4,\ldots,s_L)} & & \\
& & & & \vdots & & & & \\
& \underbrace{c_{(a_{L-2},s_{L-1}),(s_L)}}_{[r_{L-2} d\times d]} & = & \sum_{a_{L-1}}^{r_{L-1}} & \underbrace{U_{(a_{L-2},s_{L-1}),(a_{L-1})}}_{[r_{L-2} d\times r_{L-1}]} & \underbrace{\lambda_{a_{L-1}} V^\dagger_{(a_{L-1}),(s_L)}}_{[r_{L-1}\times d]} & & \\
& & & & \to A^{s_{L-1}}_{a_{L-2},a_{L-1}} & = c_{(a_{L-1}),(s_L)} & & \\
& & & & \underbrace{c_{(a_{L-1},s_L),(1)}}_{[r_{L-1} d\times 1]} & \to A^{s_L}_{a_{L-1},1} & &
\end{aligned}
\tag{4.2.6}
$$

There is a very intuitive graphical representation of a matrix product state, whose actual power will become clear later. It is depicted in Fig. 4.2, see also Fig. 4.3. Here, each circle corresponds to a site, where a matrix $\boldsymbol{M}^{s_l}$

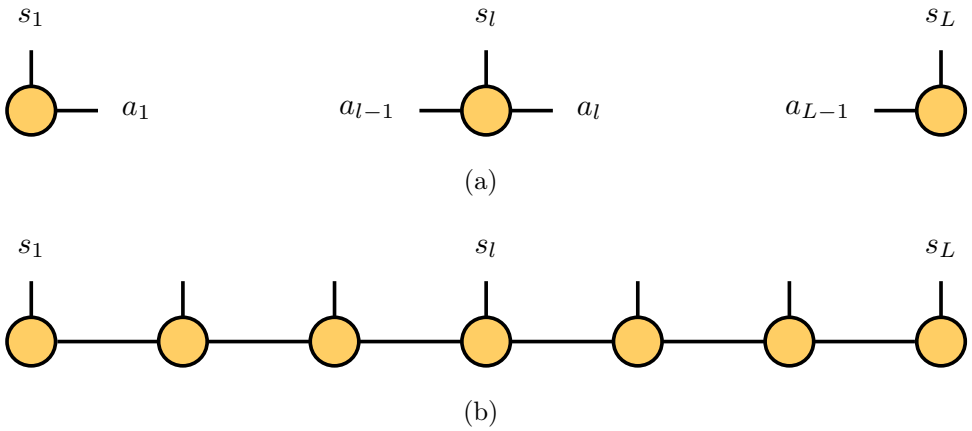

Figure 4.2: Graphical representation of an MPS. (a) Row vector $M^{s_1}_{1,a_1}$ (left), matrix $M^{s_l}_{a_{l-1},a_l}$ (center), column vector $M^{s_L}_{a_{L-1},1}$ (right) and (b) whole matrix product state. This representation is, i.a., typically used for $\boldsymbol{A}$ and $\boldsymbol{B}$ matrices. It was adapted from [92].

lives. The *physical* index s_l sticks out as a vertical line and the *auxiliary* row and column indices of the matrix a_{l-1} and a_l, are represented as horizontal lines.[4] Connected lines are summed over, which is known as *contraction*.

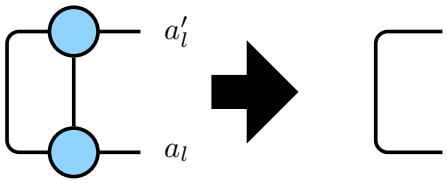

Figure 4.3: Contraction of two left-normalized matrices, $\boldsymbol{A}^{s_l\dagger}$ and $\boldsymbol{A}^{s_l}$, over their left index and the physical indices (pointing downwards for the conjugate matrix). The result is a $\delta_{a'_l a_l}$ line, see Eq. (4.2.4). This representation was adapted from [92].

[4]The a_l are called auxiliary indices, since they are artificially introduced via SVDs and vanish upon evaluating the coefficient $c_{s_1,\ldots,s_L}$ by actually performing the matrix products.

4.2.2 Right-canonical form

Notice that one could also start with $c_{(s_1,\ldots,s_L),(1)}$, split off row indices from the right hand side, starting with s_L, and regroup them to become column indices. Then one would carry out an SVD, such as before, and decompose $\boldsymbol{V}^\dagger$ into a set of matrices $\boldsymbol{B}^{s_L}$, while multiplying $\boldsymbol{U}\boldsymbol{\Lambda}$ to be the new coefficient matrix and so on and so forth, see Eq. (4.2.9). The representation achieved in this way,

$$c_{s_1,\ldots,s_L} = \boldsymbol{B}^{s_1}\boldsymbol{B}^{s_2}\ldots\boldsymbol{B}^{s_{L-1}}\boldsymbol{B}^{s_L}\,, \tag{4.2.7}$$

is, what we call *right-normalized*, since $\boldsymbol{V}^\dagger\boldsymbol{V} = \mathbb{1}$ holds for each singular value decomposition, leading to the relation (see also Fig. 4.4)

$$\sum_{s_l} \boldsymbol{B}^{s_l}\boldsymbol{B}^{s_l\dagger} = \mathbb{1}\,. \tag{4.2.8}$$

Matrix product states consisting only of right-normalized matrices are called *right-canonical*. The $\boldsymbol{B}$ matrices have the same bounds as the $\boldsymbol{A}$ matrices, Eq. (4.2.5), and their graphical representation is analogous, see Fig. 4.2.

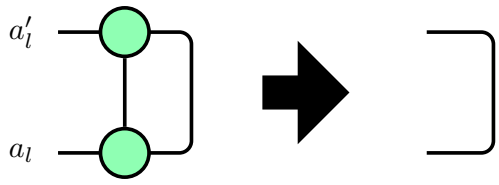

Figure 4.4: Contraction of two right-normalized matrices, $\boldsymbol{B}^{s_l}$ and $\boldsymbol{B}^{s_l\dagger}$, over their right index and the physical indices (pointing downwards for the conjugate matrix). The result is a $\delta_{a_l' a_l}$ line, see Eq. (4.2.8). This representation was adapted from [92].

Derivation of a right-canonical MPS:

$$
\begin{aligned}
& & & & & & & & [d^L \times 1] & & \\
& & c_{s_1,\ldots,s_L} & = & c_{(s_1,\ldots,s_L),(1)} & & & & & & \\
& \underbrace{c_{(s_1,\ldots,s_{L-1}),(s_L)}}_{[d^{L-1}\times d]} & = & \sum_{a_{L-1}}^{r_{L-1}} & \underbrace{U_{(s_1,\ldots,s_{L-1}),(a_{L-1})}\lambda_{a_{L-1}}}_{[d^{L-1}\times r_{L-1}]} & & \underbrace{V^\dagger_{(a_{L-1}),(s_L)}}_{[r_{L-1}\times d]} & & \\
& & & & = c_{(s_1,\ldots,s_{L-1}),(a_{L-1})} & & \to B^{s_L}_{a_{L-1},1} & & \\
& \underbrace{c_{(s_1,\ldots,s_{L-2}),(s_{L-1},a_{L-1})}}_{[d^{L-2}\times d\, r_{L-1}]} & = & \sum_{a_{L-2}}^{r_{L-2}} & \underbrace{U_{(s_1,\ldots,s_{L-2}),(a_{L-2})}\lambda_{a_{L-2}}}_{[d^{L-2}\times r_{L-2}]} & & \underbrace{V^\dagger_{(a_{L-2}),(s_{L-1},a_{L-1})}}_{[r_{L-2}\times d\, r_{L-1}]} & & \\
& & & & = c_{(s_1,\ldots,s_{L-2}),(a_{L-2})} & & \to B^{s_{L-1}}_{a_{L-2},a_{L-1}} & & \\
& \underbrace{c_{(s_1,\ldots,s_{L-3}),(s_{L-2},a_{L-2})}}_{[d^{L-3}\times d\, r_{L-2}]} & = & \sum_{a_{L-3}}^{r_{L-3}} & \underbrace{U_{(s_1,\ldots,s_{L-3}),(a_{L-3})}\lambda_{a_{L-3}}}_{[d^{L-3}\times r_{L-3}]} & & \underbrace{V^\dagger_{(a_{L-3}),(s_{L-2},a_{L-2})}}_{[r_{L-3}\times d\, r_{L-2}]} & & \\
& & & & = c_{(s_1,\ldots,s_{L-3}),(a_{L-3})} & & \to B^{s_{L-2}}_{a_{L-3},a_{L-2}} & & \\
& & & & \vdots & & & & & & \\
& \underbrace{c_{(s_1),(s_2,a_2)}}_{[d\times d\, r_2]} & = & \sum_{a_1}^{r_1} & \underbrace{U_{(s_1),(a_1)}\lambda_{a_1}}_{[d\times r_1]} & & \underbrace{V^\dagger_{(a_1),(s_2,a_2)}}_{[r_1\times d\, r_2]} & & \\
& & & & = c_{(s_1),(a_1)} & & \to B^{s_2}_{a_1,a_2} & & \\
& & & & \underbrace{c_{(1),(s_1,a_1)}}_{[1\times d\, r_1]} & & \to B^{s_1}_{1,a_1} & &
\end{aligned}
\tag{4.2.9}
$$

4.2.3 Mixed-canonical form

It is also possible to combine the derivation of an MPS from the left and the right side and arrive at a representation in so-called *mixed canonical* form,

$$c_{s_1,\ldots,s_L} = \boldsymbol{A}^{s_1} \ldots \boldsymbol{A}^{s_l} \boldsymbol{\Lambda}^{[l]} \boldsymbol{B}^{s_{l+1}} \ldots \boldsymbol{B}^{s_L} \,. \tag{4.2.10}$$

The diagonal matrix $\boldsymbol{\Lambda}^{[l]}$ contains the singular values at the bond $(l, l+1)$. If $\boldsymbol{\Lambda}^{[l]}$ is multiplied with $\boldsymbol{A}^{s_l}$, the position l is referred to as *orthogonality center*.[5] A special feature of this representation is that the Schmidt decomposition into subsystems A and B may be read off directly,

$$\begin{aligned} |a_l\rangle_A &= \sum_{\boldsymbol{s}} (\boldsymbol{A}^{s_1} \ldots \boldsymbol{A}^{s_l})_{1,a_l} |s_1, \ldots, s_l\rangle \,, \\ |a_l\rangle_B &= \sum_{\boldsymbol{s}} (\boldsymbol{B}^{s_{l+1}} \ldots \boldsymbol{B}^{s_L})_{a_l,1} |s_{l+1}, \ldots, s_L\rangle \,, \\ |\psi\rangle &= \sum_{a_l} \lambda_{a_l} |a_l\rangle_A \otimes |a_l\rangle_B \,. \end{aligned} \tag{4.2.11}$$

The states $\{|a_l\rangle_A\}$ form an orthonormal basis of A[6] and so do the states $\{|a_l\rangle_B\}$ of B. This is a consequence of the left- and right-normalization property of the respective matrices, Eqs. (4.2.4) and (4.2.8). Further, the reduced density operators[7] and the von Neumann entropy of entanglement[8] are readily accessed in these bases,[9]

$$\begin{aligned} \boldsymbol{\rho}_A^{[l]} &= \left(\boldsymbol{\Lambda}^{[l]}\right)^2 = \boldsymbol{\rho}_B^{[l]} \,, \\ S_A &= -\operatorname{Tr}\left[\left(\boldsymbol{\Lambda}^{[l]}\right)^2 \log\left(\boldsymbol{\Lambda}^{[l]}\right)^2\right] = S_B \,. \end{aligned} \tag{4.2.12}$$

There is also a special graphical representation of MPS in mixed-canonical form, see Fig. 4.5. It looks quite similar to the left- and right-canonical cases, Fig. 4.2; the additional matrix $\boldsymbol{\Lambda}^{[l]}$ is represented as a diamond.

[5] multiplying $\boldsymbol{\Lambda}^{[l]}$ with $\boldsymbol{B}^{s_{l+1}}$ makes $l+1$ the orthogonality center.
[6] if they are complete
[7] $\hat{\rho}_A = \operatorname{Tr}_B \hat{\rho}$ with $\hat{\rho} = |\psi\rangle\langle\psi|$
[8] $S_A = -\operatorname{Tr}_A [\hat{\rho}_A \log \hat{\rho}_A]$
[9] $\{|a_l\rangle_A\}$ is the eigenbasis of $\hat{\rho}_A$ and $\{|a_l\rangle_B\}$ of $\hat{\rho}_B$. They share the eigenvalues λ_{a_l}.

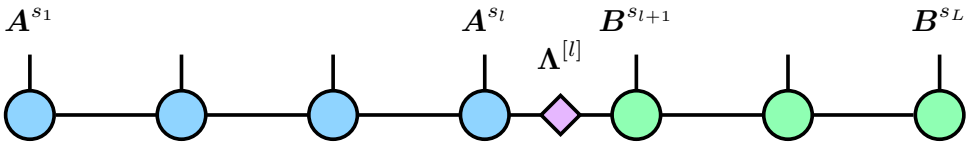

Figure 4.5: MPS in mixed-canonical form, adapted from [92].

4.2.4 Canonical form

Another possibility is to split the singular values off all $\boldsymbol{A}$ and/or $\boldsymbol{B}$ matrices [93]. This is useful, because it enables us to access all possible bipartitionings into subsystems A and B at a glance. Substituting

$$\begin{aligned} \boldsymbol{A}^{s_l} &= \boldsymbol{\Lambda}^{[l-1]}\boldsymbol{\Gamma}^{s_l} \\ \boldsymbol{B}^{s_l} &= \boldsymbol{\Gamma}^{s_l}\boldsymbol{\Lambda}^{[l]} \end{aligned} \tag{4.2.13}$$

and additionally introducing $\boldsymbol{\Lambda}^{[0]} = \boldsymbol{\Lambda}^{[L]} = 1$, formally[10] results in an MPS in *canonical* form or $\Gamma - \Lambda$ representation,

$$c_{s_1,\ldots,s_L} = \boldsymbol{\Gamma}^{s_1}\boldsymbol{\Lambda}^{[1]}\boldsymbol{\Gamma}^{s_2}\ldots\boldsymbol{\Gamma}^{s_{L-1}}\boldsymbol{\Lambda}^{[L-1]}\boldsymbol{\Gamma}^{s_L}\,. \tag{4.2.14}$$

In this representation, both a left- and a right-normalization condition hold, as a consequence of Eqs. (4.2.4) and (4.2.8), and are expressed, according to

$$\begin{aligned} \sum_{s_l} \boldsymbol{\Gamma}^{s_l\dagger}\boldsymbol{\rho}_B^{[l-1]}\boldsymbol{\Gamma}^{s_l} &= \mathbb{1}\,, \\ \sum_{s_l} \boldsymbol{\Gamma}^{s_l}\,\boldsymbol{\rho}_A^{[l]}\boldsymbol{\Gamma}^{s_l\dagger} &= \mathbb{1}\,. \end{aligned} \tag{4.2.15}$$

The Schmidt decomposition, the reduced density operators and the entanglement entropy are again given by Eqs. (4.2.11), (4.2.12),[11] with the substitution (4.2.13). MPS in canonical form have an individual graphical representation, see Fig. 4.6, where the $\boldsymbol{\Lambda}$ matrices with the singular values live on the bonds between the $\boldsymbol{\Gamma}$ matrices.

[10] In practice, SVDs have to be performed, in order to extract the singular values.
[11] but for arbitrary l

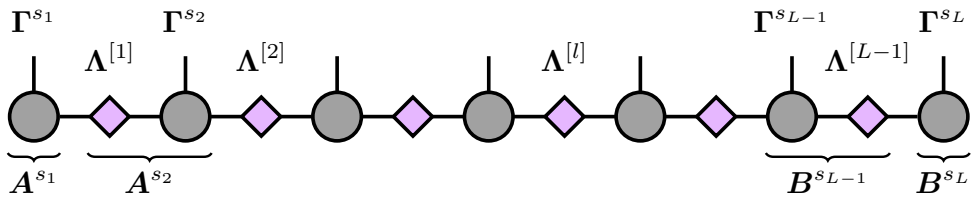

Figure 4.6: MPS in canonical form, i.e. $\Gamma - \Lambda$ form, adapted from [92].

4.2.5 Conversion

We have seen that the representation as a matrix product state is not unique. In general, a gauge degree of freedom exists. Specifically, the transformation with an invertible matrix $\boldsymbol{X}$ of adequate dimension, according to

$$\begin{aligned} \boldsymbol{A}^{s_l} &\to \boldsymbol{A}^{s_l}\boldsymbol{X} \\ \boldsymbol{A}^{s_{l+1}} &\to \boldsymbol{X}^{-1}\boldsymbol{A}^{s_{l+1}} \end{aligned} \tag{4.2.16}$$

leaves the coefficient unchanged, since $\boldsymbol{A}^{s_l}\boldsymbol{X}\boldsymbol{X}^{-1}\boldsymbol{A}^{s_{l+1}} = \boldsymbol{A}^{s_l}\boldsymbol{A}^{s_{l+1}}$. The canonical forms presented in Secs. 4.2.1-4.2.4 are only special cases of such a transformation. They are usually preferred, since they provide useful features, e.g.: The normalization properties can be exploited to efficienty calculate overlaps; Schmidt decompositions and the entanglement entropy are interesting for MPS approximations, see Sec. 4.3. Fig. 4.7 sketches, how different MPS representations relate to each other.

4.3 Approximation of matrix product states

In Sec. 4.2, it was shown, how to derive an MPS representation exactly for an arbitrary (normalized) state. We saw that the matrices can become exponentially large, which is unfavorable or even unmanageable in computational practice. Therefore, we wish to approximate these matrices by smaller ones, while keeping all important information.

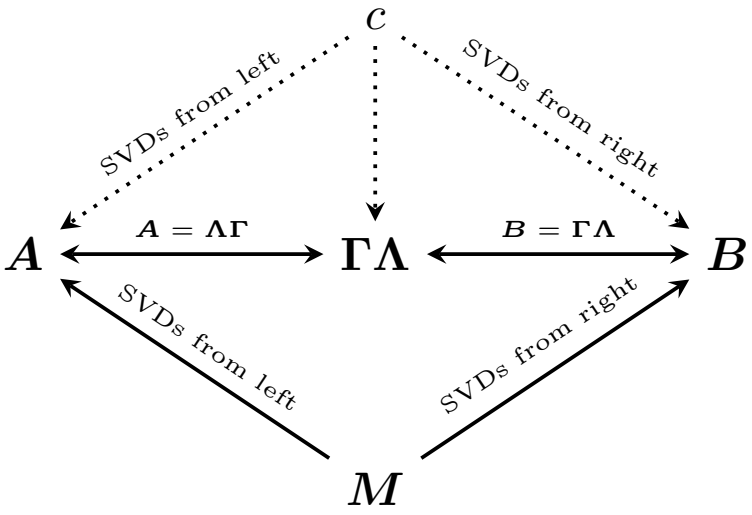

Figure 4.7: Conversion between MPS representations, adapted from [92]. Here, c is the coefficient of the state, $\boldsymbol{M}$ indicates an MPS representation with general matrices and $\boldsymbol{A}$, $\boldsymbol{B}$, $\boldsymbol{\Gamma}$ and $\boldsymbol{\Lambda}$ are defined as in Sec. 4.2. The conversion $\boldsymbol{\Gamma\Lambda} \to \boldsymbol{A}, \boldsymbol{B}$ is carried out easily, whereas, vice versa, SVDs and the division by singular values are required.

Truncation: According to Sec. 4.1, the optimal approximation of a matrix by a smaller one of given dimensions is achieved by truncating the singular value spectrum, accordingly. Keeping only the largest D_l singular values at bond $(l, l+1)$ of an MPS results in an error

$$\epsilon_l = \sum_{a_l=D_l+1}^{r_l} \lambda_{a_l}^2 \quad = 1 - \sum_{a_l=1}^{D_l} \lambda_{a_l}^2 \,, \tag{4.3.1}$$

which is referred to as *discarded weight*.[12] After the truncation, the remaining singular values have to be renormalized, in order to keep the state normalized,

$$\lambda_{a_l} \to \frac{\lambda_{a_l}}{\sqrt{1-\epsilon_l}} \,. \tag{4.3.2}$$

Performing the truncation at all $L-1$ bonds of a matrix product state is known as *compression*. In this procedure, an overall error is accumulated,

[12] The second equality follows from the normalization of the reduced density operators, Eq. (4.2.12).

which can be shown to be bounded [94],

$$\| |\psi\rangle - |\psi\rangle_{\text{trunc}} \|^2 \leq 2 \sum_{l=1}^{L} \epsilon_l \,. \tag{4.3.3}$$

The compression can either be done by setting a threshold $\epsilon_l = \epsilon$ for all bonds, which implicitly defines a bond dimension D_l that may vary along the MPS. Alternatively, one can choose a fixed maximum bond dimension $D_l = D$ for all bonds, while keeping track of the discarded weight ϵ_l. Of course, the first option, computing at a specified maximum error, is preferable, but also the matrix dimensions should be bounded. In the ideal case, this upper bound is not reached in the course of the simulation.

Entanglement: The matrix size, which is necessary to faithfully represent a state, depends on the entanglement in the system. Therefore, this quantity should be considered, when approximating an MPS by another one with smaller bond dimension. The entanglement entropy (4.2.12) at bond $(l, l+1)$ has a maximum, if all singular values are equal, $\lambda_{a_l}^2 = D_l^{-1}$, $S_l = \log(D_l)$ leading to

$$D_l \sim \exp(S_l) \,. \tag{4.3.4}$$

In this worst-case scenario, the required bond dimension scales exponentially with the entropy. So, MPS are an efficient representation only for states with a low bipartite entanglement entropy.

Ground states of Hamiltonians with short-range couplings and an excitation gap can be shown to obey *area laws* [95–99]. These laws predict that the entanglement entropy does not grow with the volume, but with the surface area of a bipartition, $S_l \sim L^{\dim-1}$. For one-dimensional systems, this is only a point and $S_l \sim$ const., which makes them suitable candidates for MPS.

However, these area laws do not extend to excited states, which are interesting for dynamical correlation functions, or to open quantum systems, which we study in this thesis. So, there is no guarantee that MPS provide an efficient representation. Nontheless, for the impurity models considered here, Ref. [64] states that the entanglement increases with L slower than linear and

that the situation is even less severe for steady state correlation functions. This moderate increase was achieved by imposing geometric restrictions on the bath, in particular, by choosing a (quasi) one-dimensional structure.[13]

4.4 Matrix product operators

Here, we introduce matrix product operators, for the sake of completeness. We do not employ them in this thesis, but there are very interesting algorithms based on MPOs that could be relevant for future studies.[14]

In analogy to MPS, also the expansion coefficients of operators may be encoded as products of local matrices [102–106], each one having two physical indices s_l and s'_l now:

$$\begin{aligned} \hat{O} &= \sum_{\boldsymbol{s},\boldsymbol{s}'} c_{(s_1,\ldots,s_L),(s'_1,\ldots,s'_L)} \left|s_1,\ldots,s_L\right\rangle\!\left\langle s'_1,\ldots,s'_L\right| \\ c_{(s_1,\ldots,s_L),(s'_1,\ldots,s'_L)} &= \boldsymbol{W}^{s_1 s'_1}\boldsymbol{W}^{s_2 s'_2}\ldots\boldsymbol{W}^{s_{L-1}s'_{L-1}}\boldsymbol{W}^{s_L s'_L} \end{aligned} \tag{4.4.1}$$

The primed indices correspond to the bra-vector and are, therefore, called ingoing, whereas the outgoing indices relate to the ket-vector. Canonical forms of MPOs are obtained in the same way as for MPS, but regrouping the double index $(s_l\, s'_l)$, instead of the single one (s_l), see, e.g., Eq. (4.2.6). There is also an analogous graphical representation, Fig. 4.8, again with the implicit rule that connected lines are summed over.

The application of an MPO (4.4.1) to an MPS (4.2.2) yields another MPS,

$$\begin{aligned} \hat{O}\left|\psi\right\rangle &= \sum_{\boldsymbol{s},\boldsymbol{s}'} \boldsymbol{W}^{s_1 s'_1}\ldots\boldsymbol{W}^{s_L s'_L}\boldsymbol{M}^{s'_1}\ldots\boldsymbol{M}^{s'_L}\left|s_1,\ldots,s_L\right\rangle \\ &= \sum_{\boldsymbol{s}} \boldsymbol{N}^{s_1}\ldots\boldsymbol{N}^{s_L}\left|s_1,\ldots,s_L\right\rangle \\ &= \left|\phi\right\rangle \end{aligned} \tag{4.4.2}$$

with $N^{s_l}_{(b_{l-1}a_{l-1}),(b_l a_l)} = \sum_{s'_l} W^{s_l s'_l}_{b_{l-1}b_l} M^{s'_l}_{a_{l-1}a_l}$, see also Fig. 4.9. The bond di-

[13] No area law was found, but that the entropy grows slower than the volume for the considered cases.

[14] such as the time-dependent variational principle (TDVP) [100, 101]

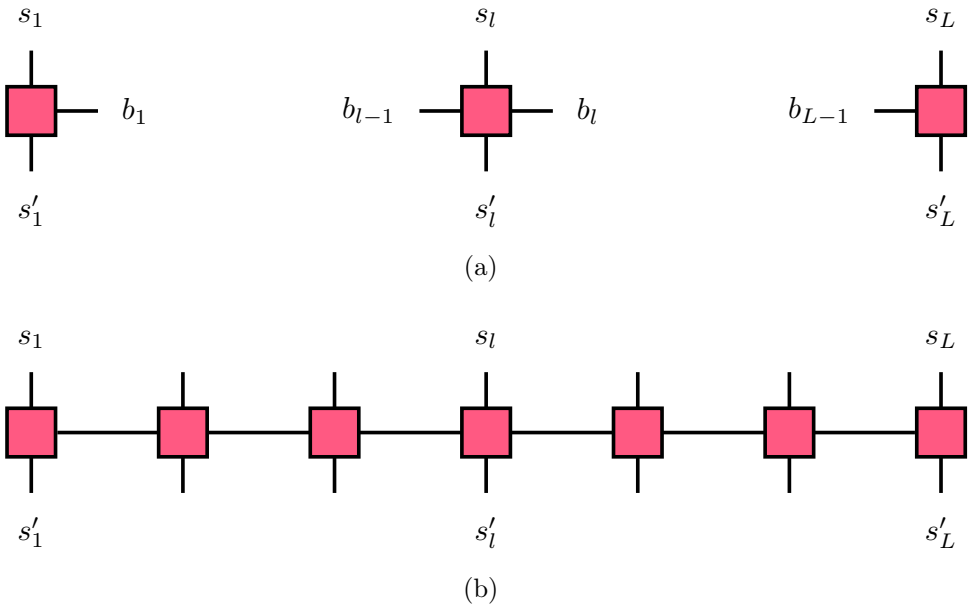

Figure 4.8: Graphical representation of an MPO, adapted from Ref. [92]. (a) Corner MPO $W^{s_1 s'_1}_{1,b_1}$ (left), bulk MPO $W^{s_l s'_l}_{b_{l-1},b_l}$ (center), corner MPO $W^{s_L s'_L}_{b_{L-1},1}$ (right) and (b) whole MPO.

mension of this new MPS (n) is the product of the bond dimensions of the MPO (w) and the initial MPS (m), $n = w \cdot n$. Since bond dimensions are multiplicative, the successive application of MPOs results in an exponential growth of matrices. Therefore, it is advisable to truncate an MPS after the application of an MPO.[15]

In Fig. 4.9, the power of the graphical representations becomes evident. Given the rule that connected lines are summed over, we immediately see that the upper physical indices of the operator will survive and the outcome of the depicted operation will again be a state. In the special case of an overlap, the operator reduces to a bra-vector, which does not possess any upper physical indices. So, all lines in the graph are connected and the outcome is obviously a scalar.

[15]For that purpose, first the normalization needs to be restored, which, in general, is destroyed by the MPO.

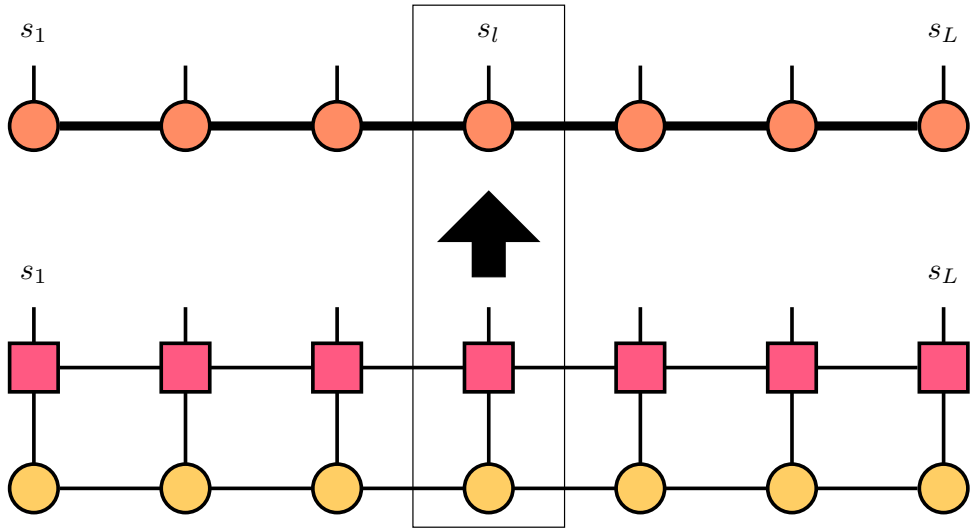

Figure 4.9: MPO applied to an MPS. The matching physical indices are contracted and a new MPS emerges, whose bond dimension is the product of the bond dimensions of the MPO and the original MPS, see Eq. (4.4.2). This representation was adapted from [92].

4.5 Time evolution

Employing matrix product states, it is possible to perform the time evolution of a system very efficiently. In this section, according algorithms are presented and discussed, which rely on a decomposition of the generator.

4.5.1 Suzuki-Trotter decomposition

In this thesis, we employ a Suzuki-Trotter decomposition of the time evolution operator [93, 102, 107–109]. We consider a Hamiltonian[16] that contains only nearest-neighbor couplings,

$$\hat{H} = \sum_l \hat{h}_l \,, \tag{4.5.1}$$

[16] An analogous procedure may be applied for a Lindbladian $\hat{L}$ in super-fermion representation, instead of the Hamiltonian, and a corresponding state $|\rho(t)\rangle$, see Sec. 3.5.

where $\hat{h}_l$ lives on the bond between sites l and $l+1$ including, e.g., operator pairs $\hat{c}_l^\dagger \hat{c}_{l+1}$. We would like to decompose the time evolution due to this Hamiltonian into smaller pieces, so-called *gates*, acting only on a couple of (ideally two) sites at a time, since this is computationally cheaper. However, such a splitting cannot be carried out exactly,[17]

$$e^{-i\hat{H}\Delta t} \neq \prod_l e^{-i\hat{h}_l \Delta t}\,, \tag{4.5.2}$$

since $[\hat{h}_l, \hat{h}_{l+1}] \neq 0$. On the other hand, $[\hat{h}_l, \hat{h}_{l+2}] = 0$ is fulfilled, since (4.5.1) has only nearest-neighbor contributions. So, if we split the Hamiltonian into even and odd terms in the sense that l is either even or odd,

$$\hat{H} = \hat{H}_{\text{even}} + \hat{H}_{\text{odd}} = \sum_{l \text{ even}} \hat{h}_l + \sum_{l \text{ odd}} \hat{h}_l\,, \tag{4.5.3}$$

the following relations hold

$$\begin{aligned} e^{-i\hat{H}_{\text{even}}\Delta t} &= \prod_{l \text{ even}} e^{-i\hat{h}_l \Delta t}\,, \\ e^{-i\hat{H}_{\text{odd}}\Delta t} &= \prod_{l \text{ odd}} e^{-i\hat{h}_l \Delta t}\,. \end{aligned} \tag{4.5.4}$$

This means that the time evolution on all even bonds can be carried out at once or sequentially without accumulating an error and so does the time evolution on the odd bonds.

The simplest approximation for the time evolution on the entire lattice, containing even as well as odd bonds, is given by the *first-order Suzuki-Trotter* formula

$$e^{-i\hat{H}\Delta t} = e^{-i\hat{H}_{\text{even}}\Delta t} e^{-i\hat{H}_{\text{odd}}\Delta t} + \mathcal{O}\left((\Delta t)^2\right)\,. \tag{4.5.5}$$

Higher-order decompositions yield better approximations with a smaller error, such as the *second-order Suzuki-Trotter* formula[18]

$$e^{-i\hat{H}\Delta t} = e^{-i\hat{H}_{\text{odd}}\frac{\Delta t}{2}} e^{-i\hat{H}_{\text{even}}\Delta t} e^{-i\hat{H}_{\text{odd}}\frac{\Delta t}{2}} + \mathcal{O}\left((\Delta t)^3\right)\,, \tag{4.5.6}$$

[17] For the sake of readability, we set $\hbar = 1$ in the whole Sec. 4.5.

[18] Both of them are based on the Baker-Campbell-Hausdorff formulas.

which we employ in Ch. 5 and Ch. 6. To keep the error as small as possible, the time span Δt should be kept rather small. To still be able to evolve up to large times t, the following trick is employed,[19]

$$e^{-i\hat{H}t} = \left(e^{-i\hat{H}\Delta t}\right)^N , \tag{4.5.7}$$

where $t = N\Delta t$. So, we apply the whole sequence of gates $e^{-i\hat{h}_l\Delta t}$ in Eq. (4.5.5) or (4.5.6) for small Δt, but N times.

Notice that the Suzuki-Trotter decomposition is not restricted to even and odd terms, only. In general, it is employed to group exponentials of commuting operators and separate non-commuting groups. In this respect, it might also be employed for other types of couplings.

4.5.2 Gates

Apart from the time evolution gates introduced in Sec. 4.5.1, also *swap gates* are employed in this thesis. In the following, we take a closer look at these gates and on the application of gates, in general.

Time evolution gates: The gates for the time evolution of the system are defined as operators $\hat{g}_l(\Delta t) = e^{-i\hat{h}_l\Delta t}$, involving the neighboring sites l and $l+1$.

Swap gates: In order to deal also with longer-ranged couplings beyond nearest-neighbors, such as those in Ch. 6, swap gates can be employed [110]. Applied to a pair of sites (j,k), a swap gate exchanges the states $|s_j\rangle$ and $|s_k\rangle$, i.e. it swaps the physical indices of the local matrices in an MPS, see also Fig. 4.10,

$$\begin{aligned} \hat{S}_{jk} &= \sum_{\boldsymbol{s},\boldsymbol{s}'} c_{(s_j s_k),(s'_j s'_k)} \, |s_j s_k\rangle\langle s'_j s'_k| \, , \\ c_{(s_j s_k),(s'_j s'_k)} &= \zeta_{jk} \, \delta_{s_j s'_k} \delta_{s'_j s_k} \, , \end{aligned} \tag{4.5.8}$$

[19] This is valid, if $[\hat{H}(t_1), \hat{H}(t_2)] = 0$ for all considered times t_1, t_2, particularly, if the Hamiltonian is independent of time, such as in the scenarios considered, here.

The prefactor $\zeta_{jk} = \pm 1$ may contain a fermionic sign, depending on the nature of the states. For splinless fermions, $\zeta_{jk} = -1$, if both sites are occupied. For more complex systems, such as the one studied in Ref. [3], Ch. 6, swap gates have a more complicated structure, see Sec. 4.6. The swap operator (4.5.8) is unitary and its own inverse.

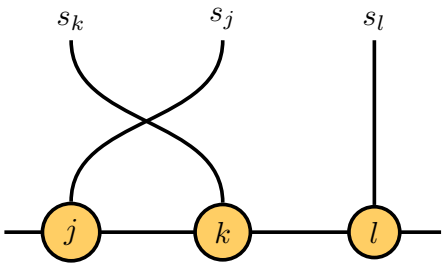

Figure 4.10: Swap gate, adapted from [111]. $\hat{S}_{jk}$ swaps states of neighboring sites j and k, e.g., in order to apply a time evolution gate between j and l, whose states are nearest neighbors in the new MPS representation.

Gate application: The change of a state in MPS form (4.2.1)-(4.2.2) due to the action of a gate may, in principle, be expressed with an MPO (4.4.1)-(4.4.2) modifying the local matrices as

$$\boldsymbol{N}^{s_l}\boldsymbol{N}^{s_{l+1}} = \left[\sum_{s'_l} \boldsymbol{W}^{s_l\, s'_l}\boldsymbol{M}^{s'_l}\right]\left[\sum_{s'_{l+1}} \boldsymbol{W}^{s_{l+1}s'_{l+1}}\boldsymbol{M}^{s'_{l+1}}\right], \tag{4.5.9}$$

see Sec. 4.4. This has the advantage that the MPS structure is preserved. The extended bond dimension is reduced via SVD. Alternatively, one can also contract the matrices at sites l and $l+1$ of the initial MPS and the MPO before the application of the gate,

$$\begin{aligned}
\overline{\boldsymbol{W}}^{s_l\, s_{l+1}s'_l s'_{l+1}} &= \boldsymbol{W}^{s_l\, s'_l}\boldsymbol{W}^{s_{l+1}s'_{l+1}} \\
\overline{\boldsymbol{M}}^{s'_l s'_{l+1}} &= \boldsymbol{M}^{s'_l}\boldsymbol{M}^{s'_{l+1}} \\
\overline{\boldsymbol{N}}^{s_l\, s_{l+1}} &= \sum_{s'_l s'_{l+1}} \overline{\boldsymbol{W}}^{s_l\, s_{l+1}s'_l s'_{l+1}}\overline{\boldsymbol{M}}^{s'_l s'_{l+1}}
\end{aligned} \tag{4.5.10}$$

or work with scalar coefficients $c_{(s_l\, s_{l+1}),(s'_l s'_{l+1})}$ directly. This results in an operator matrix $\overline{\boldsymbol{W}}$ (or scalar coefficients) with four physical indices and state matrices $\overline{\boldsymbol{M}}$, $\overline{\boldsymbol{N}}$ with two. Upon splitting the new state matrix $\overline{\boldsymbol{N}}^{s_l s_{l+1}} = \boldsymbol{N}^{s_l}\boldsymbol{N}^{s_{l+1}}$ via SVD, in order to restore the MPS structure, also the bond dimension is reduced, see Fig. 4.11.

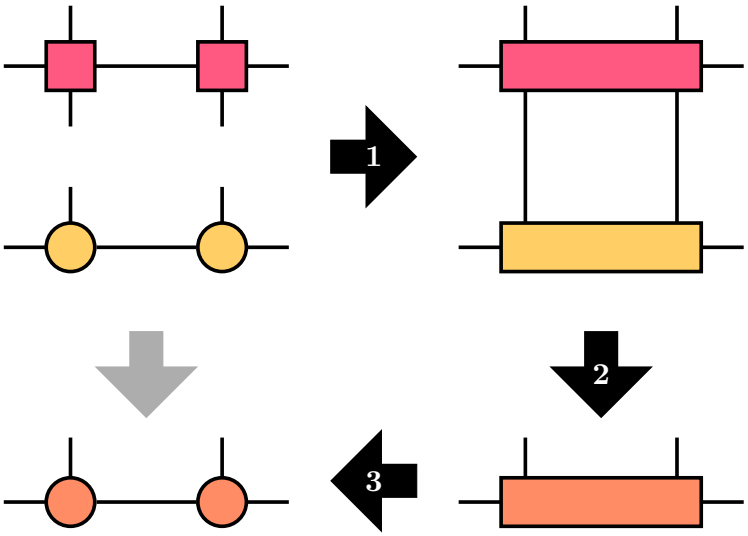

Figure 4.11: Application of a gate to an MPS. (1) Contraction of neighboring matrices, (2) Application of the gate and (3) SVD to recover the original MPS structure and compression. This representation was adapted from [111].

4.5.3 Time-dependent density-matrix renormalization group algorithm

Here (and also in Sec. 4.5.4), we consider a single element in the Suzuki-Trotter sequence of time evolutions, more precisely, the time evolution operator acting on the bond $(l+1, l+2)$,

$$e^{-i\hat{h}_{l+1}\Delta t} = \sum_{\boldsymbol{s},\boldsymbol{s}'} c_{(s_{l+1}s_{l+2}),(s'_{l+1}s'_{l+2})}\, |s_{l+1}s_{l+2}\rangle\langle s'_{l+1}s'_{l+2}| \ . \tag{4.5.11}$$

The time-dependent density-matrix renormalization group (tDMRG) algorithm [108, 109], which we employ in Ref. [3], Ch. 6, operates on states in the

mixed-canonical form, Eq. (4.2.10). Computing $\boldsymbol{\psi}^{s_{l+1}s_{l+2}} = \boldsymbol{A}^{s_{l+1}}\boldsymbol{\Lambda}^{[l+1]}\boldsymbol{B}^{s_{l+2}}$, this form is modified as

$$|\psi\rangle = \sum_{\boldsymbol{s}} \boldsymbol{A}^{s_1} \dots \boldsymbol{A}^{s_l}\boldsymbol{\psi}^{s_{l+1}s_{l+2}}\boldsymbol{B}^{s_{l+3}} \dots \boldsymbol{B}^{s_L} |\boldsymbol{s}\rangle \ . \tag{4.5.12}$$

The action of the time evolution operator (4.5.11) on this state can be expressed as a transformation of the matrix $\boldsymbol{\psi}^{s_{l+1}s_{l+2}}$ as follows (see also Sec. 4.5.2)

$$\phi^{s_{l+1}s_{l+2}}_{a_l a_{l+2}} = \sum_{s'_{l+1}s'_{l+2}} c_{(s_{l+1}s_{l+2}),(s'_{l+1}s'_{l+2})}\psi^{s'_{l+1}s'_{l+2}}_{a_l a_{l+2}} \tag{4.5.13}$$

resulting in a new state of the same structure as $|\psi\rangle$,

$$|\phi\rangle = \sum_{\boldsymbol{s}} \boldsymbol{A}^{s_1} \dots \boldsymbol{A}^{s_l}\boldsymbol{\phi}^{s_{l+1}s_{l+2}}\boldsymbol{B}^{s_{l+3}} \dots \boldsymbol{B}^{s_L} |\boldsymbol{s}\rangle \ . \tag{4.5.14}$$

In order to compute the time evolution on the next bond $(l+3, l+4)$ in the same way, we need to define a $\boldsymbol{\phi}$ matrix on this bond, and valid $\boldsymbol{A}$ and $\boldsymbol{B}$ matrices on the remaining sites. This can be achieved via an SVD,

$$\begin{aligned}\phi^{s_{l+1}s_{l+2}}_{a_l a_{l+2}} \to \phi_{(a_l s_{l+1}),(a_{l+2}s_{l+2})} &= \sum_{a_{l+1}} U_{(a_l s_{l+1})(a_{l+1})}\lambda_{a_{l+1}}(\boldsymbol{V}^\dagger)_{(a_{l+1}),(a_{l+2}s_{l+2})} \\ &= \sum_{a_{l+1}} A^{s_{l+1}}_{a_l a_{l+1}}\lambda_{a_{l+1}}(\boldsymbol{V}^\dagger)^{s_{l+2}}_{a_{l+1}a_{l+2}} \ .\end{aligned} \tag{4.5.15}$$

In the last step $\boldsymbol{\phi}^{s_{l+1}s_{l+2}}$ is truncated by discarding the smallest singular values. Further $\boldsymbol{A}^{s_{l+1}}$ is formed from the $\boldsymbol{U}$ matrix and $\boldsymbol{\Lambda}^{[l+1]}$, $\boldsymbol{V}^\dagger$ and the next $\boldsymbol{B}$ matrix are combined to

$$\phi^{s_{l+2}s_{l+3}}_{a_{l+1}a_{l+3}} = \sum_{a_{l+2}} \lambda_{a_{l+1}}(\boldsymbol{V}^\dagger)^{s_{l+2}}_{a_{l+1}a_{l+2}}B^{s_{l+3}}_{a_{l+2}a_{l+3}} \ . \tag{4.5.16}$$

The outlined procedure yields a new matrix product state, where $\boldsymbol{\phi}$ is shifted to the next bond,

$$|\phi\rangle = \sum_{\boldsymbol{s}} \boldsymbol{A}^{s_1} \dots \boldsymbol{A}^{s_{l+1}}\boldsymbol{\phi}^{s_{l+2}s_{l+3}}\boldsymbol{B}^{s_{l+4}} \dots \boldsymbol{B}^{s_L} |\boldsymbol{s}\rangle \ . \tag{4.5.17}$$

However, in order to apply $e^{-i\hat{h}_{l+3}\Delta t}$, it has to be shifted once more. So, the procedure in Eqs. (4.5.15)-(4.5.17) is repeated, starting with an SVD,

$$\begin{aligned}\phi^{s_{l+2}s_{l+3}}_{a_{l+1}a_{l+3}} \rightarrow \phi_{(a_{l+1}s_{l+2}),(a_{l+3}s_{l+3})} &= \sum_{a_{l+2}} U_{(a_{l+1}s_{l+2})(a_{l+2})}\lambda_{a_{l+2}}(\boldsymbol{V}^\dagger)_{(a_{l+2}),(a_{l+3}s_{l+3})} \\ &= \sum_{a_{l+2}} A^{s_{l+2}}_{a_{l+1}a_{l+2}}\lambda_{a_{l+2}}(\boldsymbol{V}^\dagger)^{s_{l+3}}_{a_{l+2}a_{l+3}} \,.\end{aligned} \tag{4.5.18}$$

Again, $\boldsymbol{\phi}^{s_{l+2}s_{l+3}}$ is truncated by discarding the smallest singular values. We can immediately extract $\boldsymbol{A}^{s_{l+2}}$, in the same way as before, and upon defining

$$\phi^{s_{l+3}s_{l+4}}_{a_{l+2}a_{l+4}} = \sum_{a_{l+3}} \lambda_{a_{l+2}}(\boldsymbol{V}^\dagger)^{s_{l+3}}_{a_{l+2}a_{l+3}} B^{s_{l+4}}_{a_{l+3}a_{l+4}} \tag{4.5.19}$$

we end up with the required MPS structure,

$$|\phi\rangle = \sum_{\boldsymbol{s}} \boldsymbol{A}^{s_1}\ldots\boldsymbol{A}^{s_{l+2}}\boldsymbol{\phi}^{s_{l+3}s_{l+4}}\boldsymbol{B}^{s_{l+5}}\ldots\boldsymbol{B}^{s_L}\,|\boldsymbol{s}\rangle \,. \tag{4.5.20}$$

So, in tDMRG two singular value decompositions are necessary after the application of each time evolution gate, in order to restore the structure needed to apply the next gate.

4.5.4 Time-evolving block decimation algorithm

The starting point for the time-evolving block decimation (TEBD) algorithm [93, 107], which we employ in Refs. [1], Ch. 5, is a state in the canonical $\Gamma\Lambda$ - representation, Eq. (4.2.14), which we modify as follows

$$|\psi\rangle = \sum_{\boldsymbol{s}} \boldsymbol{\Gamma}^{s_1}\boldsymbol{\Lambda}^{[1]}\ldots\boldsymbol{\Gamma}^{s_l}\boldsymbol{\psi}^{s_{l+1}s_{l+2}}\boldsymbol{\Gamma}^{s_{l+3}}\boldsymbol{\Lambda}^{[l+3]}\ldots\boldsymbol{\Gamma}^{s_L}\,|\boldsymbol{s}\rangle \tag{4.5.21}$$

with $\boldsymbol{\psi}^{s_{l+1}s_{l+2}} = \boldsymbol{\Lambda}^{[l]}\boldsymbol{\Gamma}^{s_{l+1}}\boldsymbol{\Lambda}^{[l+1]}\boldsymbol{\Gamma}^{s_{l+2}}\boldsymbol{\Lambda}^{[l+2]}$. Upon applying the time evolution operator (4.5.11), $\boldsymbol{\psi}^{s_{l+1}s_{l+2}}$ transforms, according to Eq. (4.5.13), resulting in the new state

$$|\phi\rangle = \sum_{\boldsymbol{s}} \boldsymbol{\Gamma}^{s_1}\boldsymbol{\Lambda}^{[1]}\ldots\boldsymbol{\Gamma}^{s_l}\boldsymbol{\phi}^{s_{l+1}s_{l+2}}\boldsymbol{\Gamma}^{s_{l+3}}\boldsymbol{\Lambda}^{[l+3]}\ldots\boldsymbol{\Gamma}^{s_L}\,|\boldsymbol{s}\rangle \,. \tag{4.5.22}$$

An SVD of $\boldsymbol{\phi}^{s_{l+1}s_{l+2}}$ gives Eq. (4.5.15), to which we apply $\mathbb{1} = \boldsymbol{\Lambda}^{[l]}\big(\boldsymbol{\Lambda}^{[l]}\big)^{-1}$ from the left and $\mathbb{1} = \big(\boldsymbol{\Lambda}^{[l+2]}\big)^{-1}\boldsymbol{\Lambda}^{[l+2]}$ from the right side, to obtain new $\boldsymbol{\Gamma}$ matrices as

$$\boldsymbol{\phi}^{s_{l+1}s_{l+2}} = \boldsymbol{\Lambda}^{[l]}\underbrace{\big(\boldsymbol{\Lambda}^{[l]}\big)^{-1}\boldsymbol{U}^{s_{l+1}}}_{\boldsymbol{\Gamma}^{s_{l+1}}}\boldsymbol{\Lambda}^{[l+1]}\underbrace{\boldsymbol{V}^{s_{l+2}\dagger}\big(\boldsymbol{\Lambda}^{[l+2]}\big)^{-1}}_{\boldsymbol{\Gamma}^{s_{l+2}}}\boldsymbol{\Lambda}^{[l+2]}\,. \tag{4.5.23}$$

So, the canonical form, Eq. (4.2.14), is restored with a single SVD, only. $\boldsymbol{\Lambda}^{[l+1]}$ is truncated, as usual, as well as the neighboring matrices. By computing $\boldsymbol{\phi}^{s_{l+3}s_{l+4}} = \boldsymbol{\Lambda}^{[l+2]}\boldsymbol{\Gamma}^{s_{l+3}}\boldsymbol{\Lambda}^{[l+3]}\boldsymbol{\Gamma}^{s_{l+4}}\boldsymbol{\Lambda}^{[l+4]}$, we can define

$$|\phi\rangle = \sum_{\boldsymbol{s}} \boldsymbol{\Gamma}^{s_1}\boldsymbol{\Lambda}^{[1]}\ldots\boldsymbol{\Gamma}^{s_{l+2}}\boldsymbol{\phi}^{s_{l+3}s_{l+4}}\boldsymbol{\Gamma}^{s_{l+5}}\boldsymbol{\Lambda}^{[l+5]}\ldots\boldsymbol{\Gamma}^{s_L}\,|\boldsymbol{s}\rangle \tag{4.5.24}$$

as initial state for the next gate $e^{-i\hat{h}_{l+3}\Delta t}$ acting on bond $(l+3, l+4)$. For small singular values a direct calculation of $\boldsymbol{\Gamma}$ matrices via Eq. (4.5.23) may cause numerical instabilities. However, this can be avoided with slight modifications to the algorithm, see, e.g., Ref. [112].

4.5.5 Comparison of algorithms

Both algorithms, TEBD, which was historically first, and tDMRG, are based on the representation of states as MPS. Further, they both rely on a decomposition of the global time evolution of the lattice into a sequence of small time evolutions on bonds, the gates. In this way, a Trotter error is introduced and, as a result of the compression after each gate, a truncation error. Comparing these algorithms step by step, it is obvious that they are mathematically equivalent [92]. From a numerical perspective, these are distinct algorithms. Whereas TEBD is build upon the $\Gamma\Lambda$-representation, tDMRG operates on matrix product states in the mixed canonical form. As a consequence, the TEBD algorithm allows to apply all even gates in parallel, and so the odd ones. In tDMRG, the orthogonality center needs to be shifted to one of the sites at the respective bond, before a gate can be applied, hindering a parallelization at this level. Further, tDMRG requires two SVDs to restore

the MPS structure after each gate, whereas in TEBD one suffices. Here, a division by singular values is carried out instead of the second SVD, which can give rise to numerical instabilities, if the singular values become very small. A way to circumvent this problem is presented in Ref. [112]. For a more rigorous comparison of the most recent algorithms including such that are not based on a Suzuki-Trotter decomposition we refer to Ref. [101].

4.6 This work

This thesis is concerned with the simulation of open quantum systems, which are described by a Lindblad master equation, in particular, the Anderson impurity model under bias voltage.

It is easily shown that the MPS techniques for closed quantum systems can be extended to treat open quantum systems as well, but the numeric is more involved in the latter case. Approaches have been suggested that are based on MPOs [100, 102], on some kind of super-fermion representation [64, 113] or on a stochastic evolution of the wave function [2, 114]. Here, we focus on approaches based on a super-fermion representation. In this case, the presented algorithms for the time evolution, TEBD and tDMRG, can be used, substituting $|\psi\rangle \to |\rho\rangle$ and the Hamiltonian with the Lindbladian $\hat{H} \to \hat{L}$, see Sec. 3.5.

Magnetic field: For Ref. [1], Ch. 5, we employed the canonical MPS representation and the TEBD algorithm. We decided for the following ordering of basis states,

$$\left(c_{1\downarrow}^\dagger \tilde{c}_{1\downarrow}^\dagger\right)^{n_{1\downarrow}} \left(c_{1\uparrow}^\dagger \tilde{c}_{1\uparrow}^\dagger\right)^{n_{1\uparrow}} \dots \left(c_{L\downarrow}^\dagger \tilde{c}_{L\downarrow}^\dagger\right)^{n_{L\downarrow}} \left(c_{L\uparrow}^\dagger \tilde{c}_{L\uparrow}^\dagger\right)^{n_{L\uparrow}} |0\rangle \otimes |\tilde{0}\rangle \ , \tag{4.6.1}$$

where the tilde refers to objects in the auxiliary Hilbert space. Now it is important to realize that the lattice sites do not necessarily have to coincide with the matrix sites of an MPS representation. Here, we combine spin and

tilde degrees of freedom of a lattice site in a single MPS site by defining:

$$\begin{aligned} |s_l\rangle &= \left(c^\dagger_{l\downarrow}\tilde{c}^\dagger_{l\downarrow}\right)^{n_{l\downarrow}} \left(c^\dagger_{l\uparrow}\tilde{c}^\dagger_{l\uparrow}\right)^{n_{l\uparrow}} |0\rangle \otimes |\tilde{0}\rangle \\ s_l &= (n_{l\downarrow}, \tilde{n}_{l\downarrow}, n_{l\uparrow}, \tilde{n}_{l\uparrow}) \end{aligned} \tag{4.6.2}$$

Then each physical index s_l involves four different particle numbers; the local Hilbert space dimension is $2^4 = 16$. No swap gates are required in this implementation, since there are no long-range couplings of MPS sites.

Pseudogap: In Ref. [3], Ch. 6, we decided to separate the spin degrees of freedom and chose a different ordering of states. Without going into further details - these are presented in Sec. 6.3.3.1 - the basis states read:

$$\left(c^\dagger_{1\downarrow}\tilde{c}^\dagger_{1\downarrow}\right)^{n_{1\downarrow}} \left(c^\dagger_{2\downarrow}\tilde{c}^\dagger_{2\downarrow}\right)^{n_{2\downarrow}} \dots \left(c^\dagger_{L-1\uparrow}\tilde{c}^\dagger_{L-1\uparrow}\right)^{n_{L-1\uparrow}} \left(c^\dagger_{L\uparrow}\tilde{c}^\dagger_{L\uparrow}\right)^{n_{L\uparrow}} |0\rangle \otimes |\tilde{0}\rangle \tag{4.6.3}$$

We define an MPS site,

$$\begin{aligned} |s_{l\sigma}\rangle &= \left(c^\dagger_{l\sigma}\tilde{c}^\dagger_{l\sigma}\right)^{n_{l\sigma}} |0\rangle \otimes |\tilde{0}\rangle \\ s_{l\sigma} &= (n_{l\sigma}, \tilde{n}_{l\sigma}) \end{aligned} \tag{4.6.4}$$

with a local Hilbert space dimension of $2^2 = 4$. So, in comparison to Eq. (4.6.2), the number of MPS sites is doubled. Here, swap gates are necessary, since long-range couplings were introduced by the separation of spins. The swap operator, see Sec. 4.5.2, is a 16×16 matrix in the local basis $|s_{j\sigma}s_{kv}\rangle$, since 2 MPS sites are involved, but only 16 elements are non-zero, see Eq. (4.6.5). The necessity to employ swap gates is the disadvantage of this scheme. The main advantage is the possibly lower bond dimension.[20]

[20] At $U = 0$, it is the square root of the bond dimension of the matrices in case of (4.6.2).

$$
\begin{aligned}
\hat{S}_{jk}\,|0000\rangle &= |0000\rangle & \hat{S}_{jk}\,|0100\rangle &= |0001\rangle \\
\hat{S}_{jk}\,|0001\rangle &= |0100\rangle & \hat{S}_{jk}\,|0101\rangle &= -|0101\rangle \\
\hat{S}_{jk}\,|0010\rangle &= |1000\rangle & \hat{S}_{jk}\,|0110\rangle &= -|1001\rangle \\
\hat{S}_{jk}\,|0011\rangle &= |1100\rangle & \hat{S}_{jk}\,|0111\rangle &= |1101\rangle \\
\hat{S}_{jk}\,|1100\rangle &= |0011\rangle & \hat{S}_{jk}\,|1000\rangle &= |0010\rangle \\
\hat{S}_{jk}\,|1101\rangle &= |0111\rangle & \hat{S}_{jk}\,|1001\rangle &= -|0110\rangle \\
\hat{S}_{jk}\,|1110\rangle &= |1011\rangle & \hat{S}_{jk}\,|1010\rangle &= -|1010\rangle \\
\hat{S}_{jk}\,|1111\rangle &= |1111\rangle & \hat{S}_{jk}\,|1011\rangle &= |1110\rangle
\end{aligned}
\tag{4.6.5}
$$

Chapter 5

Nonequilibrium Kondo effect in a magnetic field: Auxiliary master equation approach

Here, I present the first out of two main papers constituting this thesis, which was published in [1]. In this paper, we study the influence of an external magnetic field as well as a bias voltage on the Kondo effect manifest in quantum dots.

The results were obtained with an MPS solver to the AMEA Lindblad problem of a single, correlated impurity. I adjusted this solver, implemented by A. Dorda, to the new challenges of a magnetic field with his support and performed the calculations. Further, I was the main contributor in writing the paper. F. Schwarz performed NRG-tDMRG quench calculations for comparison and wrote the corresponding Sec. 5.3.4 guided by J. von Delft. E. Arrigoni initiated this work and wrote Sec. 5.2. All authors contributed to the discussion and conclusions of the paper and provided revisions. Major revisions were conducted by E. Arrigoni.

In the following, Ref. [1] is included literally in its entity.[1] In order to obtain a single, coherent bibliography, the citations are merged into one list of references at the end of this thesis. Furthermore, citations of articles published in the meanwhile are changed accordingly.

[1] For simplicity, we don't put this pasted text between quotation marks.

5.1 Abstract

We study the single-impurity Anderson model out of equilibrium under the influence of a bias voltage ϕ and a magnetic field B. We investigate the interplay between the shift (ω_B) of the Kondo peak in the spin-resolved density of states (DOS) and the one (ϕ_B) of the conductance anomaly. In agreement with experiments and previous theoretical calculations we find that, while the latter displays a rather linear behavior with an almost constant slope as a function of B down to the Kondo scale, the DOS shift first features a slower increase reaching the same behavior as ϕ_B only for $|g|\mu_B B \gg k_B T_K$.

Our auxiliary master equation approach yields highly accurate nonequilibrium results for the DOS and for the conductance all the way from within the Kondo up to the charge fluctuation regime, showing excellent agreement with a recently introduced scheme based on a combination of numerical renormalization group with time-dependent density matrix renormalization group.

5.2 Introduction

Since its discovery almost one century ago, the Kondo effect has been measured in many physical systems ranging from bulk materials to nanostructures. The latter are especially attractive to study, because the parameters controlling the effect can be precisely tuned in the laboratory. There is a variety of experiments on nanowires [115–117], two-dimensional electron gases confined in heterostructures [67, 118], carbon nanotubes [119] and also organic molecules [120] to mention a few. Whereas a finite temperature and a bias voltage to probe the effect are perturbations that naturally arise in these experiments and should therefore be studied, it is also interesting to study the effect of an additional magnetic field.

It is known from these experiments that upon introducing a Zeeman magnetic field B the zero-bias conductance anomaly (i.e. the peak of the conductance G as a function of bias voltage ϕ) splits into two peaks located at $\pm\phi_B$, where ϕ_B increases almost linearly with B [115–117, 121]. Theoretical calculations [54, 60, 80, 116, 122–125] confirm this behavior showing an

essentially constant slope, $e\phi_B \approx |g|\mu_B B$, almost all the way down to the point where the splitting disappears at $|g|\mu_B B \sim k_B T_K$, where T_K is the Kondo temperature that characterizes the width of the zero-bias anomaly at zero temperature and zero field. At the same time, the magnetic field produces a similar split in the total impurity density of states (spectral function), which again starts developing for magnetic fields of the order of the Kondo scale, and which corresponds to a shift $\pm\hbar\omega_B$ in the spin-resolved impurity density of states. However, in contrast to ϕ_B, this shift does not show the same strictly linear behavior. Accurate calculations based on Bethe ansatz and the numerical renormalization group (NRG) [126–128] show that ω_B is initially smaller, starting as $\hbar\omega_B \approx \frac{2}{3}|g|\mu_B B$ and reaching $|g|\mu_B B$ for $|g|\mu_B B \gg k_B T_K$ (up to logarithmic corrections [129]). Notice that less sophisticated equations of motion approaches [130] yield instead a constant slope of ω_B as well. On the other hand, the different behavior of ω_B and ϕ_B is in contradiction with the simple expectation [130] that the enhancement of the conductance should occur when the chemical potential difference reaches the splitting in the spectral function. Kondo physics out of equilibrium is a challenging issue from the theoretical point of view and it is hard to obtain accurate results for both the spectral function and the conductance for voltages beyond the linear-response regime, most nonequilibrium steady-state approaches being perturbative or their accuracy being uncontrolled.

In this paper, we investigate the single-impurity Anderson model (SIAM) in the presence of both a magnetic field B and a finite bias voltage ϕ. We adopt the recently introduced auxiliary master equation approach (AMEA), which has been shown to produce very accurate results for spectral functions and current characteristrics both in as well as out of equilibrium [64]. To confirm the accuracy of our results we compare them with the ones obtained within a hybrid method that combines NRG with the time-dependent density matrix renormalization group (tDMRG) [30] to address quantum impurities out of equilibrium. The two approaches compare excellently (see Fig. 5.6) also at zero bias voltage, where we directly compare the spectral function with NRG. Our results confirm the different behavior of ω_B and ϕ_B, showing that there is no incompatibility. We also evaluate the magnetization in the

high and low field limit, confirming the presence of a plateau at high fields for bias voltages $e\phi \lesssim |g|\mu_B B$ observed in previous theoretical results [123].

This work is organized as follows: In Sec. 5.3 the model and the solution method are described. We start with an introduction to the model, Sec. 5.3.1, followed by a part about Keldysh Green's functions, Sec. 5.3.2. Then the general idea of AMEA and the solution method are sketched, Sec. 5.3.3. In Sec. 5.3.4 the hybrid NRG-tDMRG method, which we use for comparison, is described. Sec. 5.4 contains the results and Sec. 5.5 a summary and our conclusions.

5.3 Model and Method

5.3.1 Model

We study the single-impurity Anderson model (SIAM) in a magnetic field and out of equilibrium. Throughout this paper we use units of $\hbar = e = k_B = \mu_B|g| = 1$ and $\Gamma = 1$, see Eqs. (5.3.6) and (5.3.15). The model is described by the following hamiltonian,

$$H = H_{\text{imp}} + H_{\text{leads}} + H_{\text{coup}}\,. \tag{5.3.1}$$

H_{imp} is the hamiltonian of the impurity. It is a single-site Hubbard hamiltonian with a spin-dependent on-site energy, accounting for the magnetic field,

$$H_{\text{imp}} = \sum_{\sigma\in\{\uparrow,\downarrow\}} \varepsilon_{f\sigma} f_\sigma^\dagger f_\sigma + U n_{f\uparrow} n_{f\downarrow}\,, \tag{5.3.2}$$

with $\varepsilon_{f\sigma} = -\frac{1}{2}(U + \sigma B)$. $f_\sigma^{(\dagger)}$ is the fermionic annihilation (creation) operator at the impurity for spin σ, $n_{f\sigma} = f_\sigma^\dagger f_\sigma$, U is the interaction strength and B the magentic field. The on-site energy $\varepsilon_{f\sigma}$ is chosen such that the system is particle-hole symmetric at $B = 0$. The impurity is connected to two leads described by

$$H_{\text{leads}} = \sum_{\lambda\in\{L,R\}} \sum_{k\sigma} \varepsilon_{\lambda k} d_{\lambda k\sigma}^\dagger d_{\lambda k\sigma}\,. \tag{5.3.3}$$

$d^{(\dagger)}_{\lambda k\sigma}$ is the annihilation (creation) operator for electrons with spin σ in lead $\lambda \in \{L, R\}$ at level k (out of N energy levels); $\varepsilon_{\lambda k}$ is the energy of level k. The leads have different chemical potentials μ_λ, realizing a bias voltage $\phi = \mu_R - \mu_L$ across the impurity. The hamiltonian mediating the coupling between the impurity and the leads is given by

$$H_{\text{coup}} = \frac{1}{\sqrt{N}} \sum_{\lambda\in\{L,R\}} t'_\lambda \sum_{k\sigma} \left(d^\dagger_{\lambda k\sigma} f_\sigma + \text{H.c.} \right) \tag{5.3.4}$$

with a symmetric hopping $t'_L = t'_R$. We assume that H_{leads} produces a flat density of states (DOS) $\rho_\lambda(\omega)$ in the disconnected leads with a bandwidth of $2D$,

$$\rho_\lambda(\omega) = \frac{1}{2D} \Theta(D - |\omega|)\,, \tag{5.3.5}$$

where Θ is the Heaviside step function. In this flat-band model the hybridization strength Γ, defined in Eq. (5.3.15), is given by,

$$\Gamma = \frac{\pi}{2D} \left({t'_L}^2 + {t'_R}^2 \right) . \tag{5.3.6}$$

Using $\Gamma = 1$ as unit of energy yields $t'_\lambda = \sqrt{\frac{D}{\pi}}$ for the hopping to the leads. Throughout this paper we take $D = 10$.
We furthermore use the following definition of the Kondo temperature T_K,

$$G(T = T_K, \phi = 0) = \frac{1}{2} G_0\,, \tag{5.3.7}$$

at $B = 0$. G is the linear-response differential conductance, Eq. (5.3.18), $G_0 = G(T = 0, \phi = 0) = 1/\pi$.

5.3.2 Keldysh Green's functions

While there is only one independent Green's function in equilibrium, there are two in nonequilibrium: The retarded and the Keldysh Green's function, G^R and G^K, e.g., are independent of each other. At finite magnetic field they are furthermore different for both spin kinds. In steady state, when the

system is time-translation invariant, they are defined as

$$\begin{aligned} G_\sigma^R(t) &= -i\Theta(t)\left\langle\left\{f_\sigma(t), f_\sigma^\dagger\right\}\right\rangle , \\ G_\sigma^K(t) &= -i\left\langle\left[f_\sigma(t), f_\sigma^\dagger\right]\right\rangle , \end{aligned} \tag{5.3.8}$$

and in Fourier space,

$$G_\sigma^\alpha(\omega) = \int G_\sigma^\alpha(t)\exp(i\omega t)\,dt\,, \tag{5.3.9}$$

with $\alpha \in \{R, K\}$. Upon introducing the Keldysh contour, these Green's functions can be arranged in a matrix structure, according to

$$\underline{G}_\sigma(\omega) = \begin{pmatrix} G_\sigma^R(\omega) & G_\sigma^K(\omega) \\ 0 & G_\sigma^A(\omega) \end{pmatrix} , \tag{5.3.10}$$

where the advanced Green's function is related to the retarded one by $G_\sigma^A(\omega) = G_\sigma^R(\omega)^\dagger$. In this way, the familiar form of Dyson's equation is maintained,

$$\begin{aligned} \underline{G}_\sigma^{-1}(\omega) &= \underline{g}_{0\sigma}^{-1}(\omega) - \underline{\Delta}(\omega) - \underline{\Sigma}(\omega) \\ &= \underline{G}_{0\sigma}^{-1}(\omega) - \underline{\Sigma}(\omega)\,. \end{aligned} \tag{5.3.11}$$

$\underline{G}_\sigma(\omega)$ is the full interacting Green's function of the impurity connected to the leads, $\underline{g}_{0\sigma}(\omega)$ is the noninteracting Green's function of the disconnected impurity, $\underline{\Delta}(\omega)$ is the hybridization of the impurity by the leads and $\underline{\Sigma}(\omega)$ accounts for the interaction at the impurity. The noninteracting Green's functions are combined to $\underline{G}_{0\sigma}(\omega) = \underline{g}_{0\sigma}^{-1}(\omega) - \underline{\Delta}(\omega)$. The hybridization function is given by

$$\underline{\Delta}(\omega) = \sum_\lambda {t'_\lambda}^2 \underline{g}_\lambda(\omega)\,, \tag{5.3.12}$$

where $\underline{g}_\lambda(\omega)$ is the (noninteracting) Green's function of the decoupled leads. Since these are in equilibrium, its components obey the fluctuation-dissipation theorem,

$$g_\lambda^K(\omega) = 2\pi i\left(2f_\lambda(\omega, T) - 1\right)\rho_\lambda(\omega)\,, \tag{5.3.13}$$

where $f_\lambda = [\exp[(\omega - \mu_\lambda)/T] + 1]^{-1}$ denotes the Fermi function at temperature T and chemical potential μ_λ. The DOS in the leads is connected to $g^R_\lambda(\omega)$,

$$\rho_\lambda(\omega) = -\frac{1}{\pi}\Im g^R_\lambda(\omega). \tag{5.3.14}$$

Therefore in equilibrium only one independent Green's function persists. The hybridization strength Γ is defined, using Eq. (5.3.12),

$$\Gamma = -\Im\Delta^R(\omega = 0). \tag{5.3.15}$$

Given the full interacting Green's function at the impurity, the spin-resolved and total spectral functions are calculated as

$$A_\sigma(\omega) = -\frac{1}{\pi}\Im G^R_\sigma(\omega), \qquad A_{\uparrow\downarrow} = \frac{1}{2}\left(A_\uparrow + A_\downarrow\right). \tag{5.3.16}$$

The current across the impurity is determined via the Meir-Wingreen formula [130]. In case of a bias-independent lead DOS with $\rho_L(\omega) = \rho_R(\omega)$, such as (5.3.5), it reduces to [91]

$$j = \int A_{\uparrow\downarrow}(\omega)\,\gamma(\omega)\left(f_R(\omega, T) - f_L(\omega, T)\right)d\omega\,, \tag{5.3.17}$$

where $\gamma(\omega) = -\Im\Delta^R(\omega)$. In linear-response the differential conductance $G = \frac{\partial j}{\partial \phi}$ is calculated from (5.3.17) as

$$G = \int A_{\uparrow\downarrow}(\omega)\,\gamma(\omega)\left(-\frac{\partial}{\partial\omega}f(\omega, T)\right)d\omega\,, \tag{5.3.18}$$

where $f = f_L|_{\mu_L=0} = f_R|_{\mu_R=0}$ is the Fermi function at zero bias. In the general case, we calculate the differential conductance from finite current differences using three-point Lagrange polynomials to approximate the derivative.

5.3.3 Method

We here present a short sketch of the auxiliary master equation approach (AMEA) used in this paper. For more details, we refer to Refs. [22, 63, 64, 83]. The idea is to map the physical system described by (5.3.1) to a finite and open auxiliary system that has almost the same hybridization at the impurity as the original one (5.3.12) and thereby maintains the impurity physics, which we are interested in. The auxiliary system consists of a small number of N_B bath sites connected to Markovian environments and its dynamics is governed by a Lindblad master equation. The parameters in this equation are determined to achieve a corresponding auxiliary hybridization function $\underline{\Delta}_{\mathrm{aux}}(\omega)$ such that $\underline{\Delta}_{\mathrm{aux}}(\omega) \approx \underline{\Delta}(\omega)$ as accurately as possible, cf. [83]. The physical hybridization function $\underline{\Delta}$ is calculated from the given lead DOS, Eq. (5.3.5), using Eqs. (5.3.12)-(5.3.14) and the Kramers-Kronig relation that links the real and imaginary part of a Green's function. The auxiliary hybridization function $\underline{\Delta}_{\mathrm{aux}}$ can be calculated for a general set of bath parameters by solving a noninteracting Lindblad problem, see, e.g. Refs. [63, 83, 131, 132]. The determination of these parameters and thus the mapping to the physical system is carried out with a parallel tempering algorithm [83]. The resulting Lindblad equation is solved by using matrix product states (MPS) and the time evolving block decimation algorithm (TEBD), as described in [64]. Since the auxiliary Lindblad system is essentially exactly solvable, the approximation of the method lies in the difference between $\underline{\Delta}_{\mathrm{aux}}(\omega)$ and $\underline{\Delta}(\omega)$. As shown in Ref. [83], this difference vanishes exponentially upon increasing N_B. Therefore, a moderate number of bath sites ($N_B \approx 14 - 20$) is sufficient to reach the accuracy required in the present paper.

The results we present here are in the steady state, which is determined via time evolution and formally reached with $t \to \infty$. The Green's functions are also calculated in the time domain, starting from the steady state; they are continued to large times by linear prediction and then subjected to a Fourier transformation.

The bias voltage is realized by shifting the chemical potentials in the leads

symmetrically with respect to each other, $\mu_R = -\mu_L = \frac{\phi}{2}$. Note that for each bias voltage a new $\underline{\Delta}_{\text{aux}}$ has to be determined, since ϕ enters the Keldysh part of the hybridization function.

The calculations for $B < 1$, $\phi < 1.8$ and $B > 1$, $\phi < 2.1$ are with $N_B = 20$ bath sites; for all other parameters $N_B = 14$ is sufficient. For the subsequent TEBD calculation we restrict the fit to nearest neighbour couplings.

All results shown in this paper are for the symmetric SIAM, $t'_L = t'_R$. Note that the extension to the non-symmetric model is simple and straightforward.

5.3.4 Comparison to NRG-tDMRG quench calculations

We compare our data to results obtained in a hybrid NRG-tDMRG quench setup which is described in Ref. [30]. While AMEA treats the impurity model as a truly open quantum system in the sense of a Lindblad master equation, for "small enough" time scales t one can equally well consider quenches in a closed quantum system [133, 134]. Starting with an initial state in which the two leads are in thermal equilibrium, but held at different chemical potential, standard Hamiltonian time evolution will drive the system towards its "steady state" until at some point in time finite-size effects set in. For the SIAM one faces the difficulty that the different energy and time scales inherent in the model have to be handled with care. The hybrid NRG-tDMRG approach presented in Ref. [30] meets this challenge by exploiting the fact that energy scales outside the transport window, where $f_L(\omega, T) \approx f_R(\omega, T)$, are effectively in equilibrium. Thus, they can be traced out using the numerical renormalization group (NRG) [135]. Subsequently, the non-equilibrium processes arising on the energy scale of the transport window are treated within this renormalized setup using a tDMRG [92, 107–109] quench. Both methods, NRG and tDMRG, are implemented based on MPS.

For the high-energy range outside the transport window a logarithmic discretization is used, while the transport window itself is discretized linearly. After mapping the problem onto a chain, the Hamiltonian of the first part of this chain, which represents the high-energy modes, can be diagonalized using NRG. This yields a truncated effective low-energy basis for this part of the

system, which can be seen as the local state space of a renormalized impurity (RI). This RI is coupled to the remainder of the leads, which corresponds to the energy range of the transport window and therefore has an effective bandwidth set by voltage and temperature. The quench is initialized with a state $|\Psi\rangle = |\psi_{\text{ini}}\rangle \otimes |\Omega\rangle$, where $|\psi_{\text{ini}}\rangle$ lies in the ground state sector of the RI and $|\Omega\rangle$ is the thermal state of the remaining part of the leads at different chemical potential and decoupled from the RI. This state is time-evolved using tDMRG. The relevant time scale for this quench is given by the size of the transport window.

To further simplify the MPS calculation, the leads are described in the form suggested by the thermofield approach [136–138], in which the thermal state $|\Omega\rangle$ is a pure quantum state, and, even more advantageously, a simple product state on the MPS chain. This implies that the time evolution of the tDMRG quench is started with a product state and, hence, with lowest possible entanglement.

In practice, the time evolution is typically limited, due to the entanglement growth, before finite size effects set in. So far, the approach has only been used to calculate expectation values, because the determination of spectral functions would need far more numerical resources. For all data points with $\phi > 0.14D$ there was no need to use NRG, because the transport window is of similar size as the full bandwidth. For high voltages convergence was achieved only in the current and not in the magnetization. However, the time dependence of the dot's occupation, $\langle n_\sigma \rangle (t)$, follows an exponential decay such that one can extrapolate to the steady-state value.

5.4 Results

Our approach allows for an accurate solution of the model in and out of equilibrium, below, but also above the energy scale T_K, so as to take into account the influence of charge excitations and of the Hubbard bands. At the same time, below T_K and in equilibrium our results show a remarkable agreement of the spectral function with NRG up to intermediate values of $U/\Gamma \lesssim 6$, see Fig. 5.6(a) and Ref. [64]. Here we want to study the behavior

and interplay of the spectral function and the differential conductance in the presence of a finite Zeeman magnetic field B and bias voltage ϕ. In particular, we focus on the shift of the Kondo and of the zero-bias peak.

We start by plotting the impurity spectral function in equilibrium ($\phi = 0$) for different magnetic fields B, see Fig. 5.1. Most of our results are obtained for an interaction of $U = 6$, corresponding to a Kondo temperature of $T_K \approx 0.2$. The temperature is fixed to $T/T_K \approx 0.25$. At finite magnetic field, the spin degeneracy is lifted, resulting in different spectral functions for spin-up and spin-down electrons. At particle-hole symmetry they are related to each other, according to $A_\uparrow(\omega) = A_\downarrow(-\omega)$. Upon increasing the magnetic field, the Kondo resonance is suppressed and it broadens, similarly to the effect of a bias voltage, cf. Refs. [55–65, 139–141]. Furthermore, a magnetic field causes a shift ω_B of the Kondo resonance to higher energies in the spin-resolved spectral function $A_\downarrow$ and produces a splitting δ_A in the total spectral function $A_{\uparrow\downarrow} = \frac{1}{2}(A_\uparrow + A_\downarrow)$. This splitting starts at $B \gtrsim T_K$, see also Refs. [122, 127, 142], and persists until the peaks merge with the Hubbard bands. The position of the Kondo resonance in $A_\downarrow$ becomes $\approx B$ for large B, while for decreasing B the ratio ω_B/B decreases (see Fig. 5.4), consistent with previous results, mainly on the Kondo model [54, 80, 126–128, 143]. Note that for large magnetic fields one has $\delta_A = 2\omega_B$, while for small magnetic fields δ_A is smaller, due to the overlap of the contributions from the two spin directions.

A similar splitting is produced by a bias voltage in the absence of a magnetic field [60, 63, 64], so that it is interesting to study the combined behavior of the two effects. In the presence of both, a finite bias voltage and magnetic field, one would expect 4 peaks in the total spectral function at $\pm B \pm \phi/2$. This has been observed within an equation of motion approach in Ref. [80] (see also Ref. [123]). It is not easy to observe such a four-peak structure within a numerically controlled, nonperturbative approach. In our case, for $U = 6$, the higher energy peaks merge with the Hubbard bands before the peaks are sufficiently far apart, so that they look more like shoulders than peaks. For this reason, we investigate this effect for $U = 8$. Fig. 5.2(a) shows the spin-resolved spectral functions $A_\downarrow(\omega)$ at $B = 1$ for different bias voltages

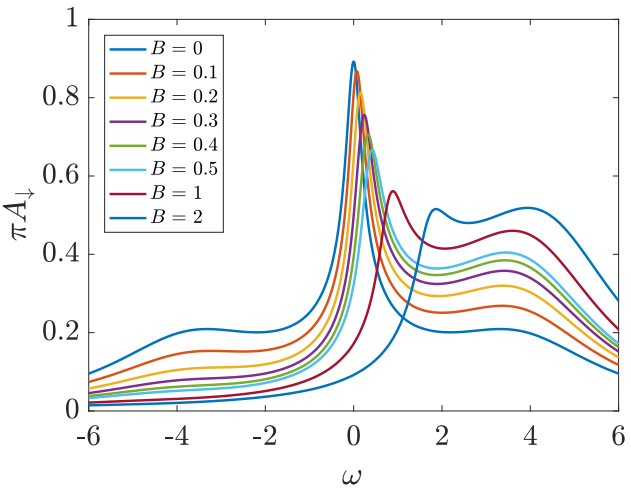

(a)

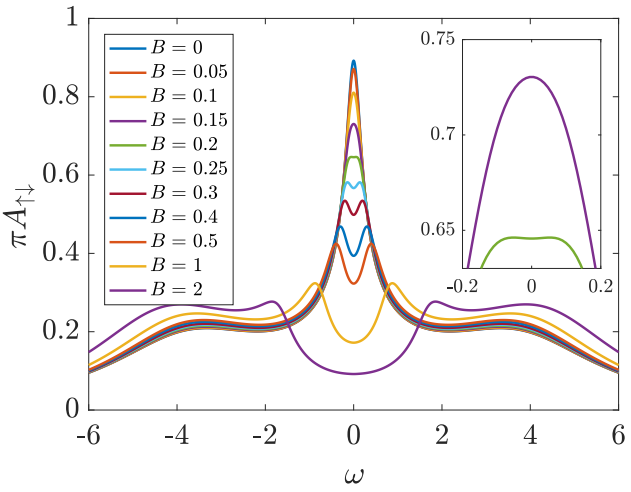

(b)

Figure 5.1: Equilibrium ($\phi = 0$) spin-resolved $A_{\downarrow}(\omega)$ (a) and total $A_{\uparrow\downarrow}(\omega)$ (b) impurity spectral function for different magnetic fields B and for $U = 6\Gamma$ and $T = 0.05\Gamma/k_B \approx T_K/4$. Note that B is in units of $\Gamma/(|g|\mu_B)$, ω is in units of $\Gamma/\hbar$ and spectral functions are in units of $\hbar/\Gamma$.

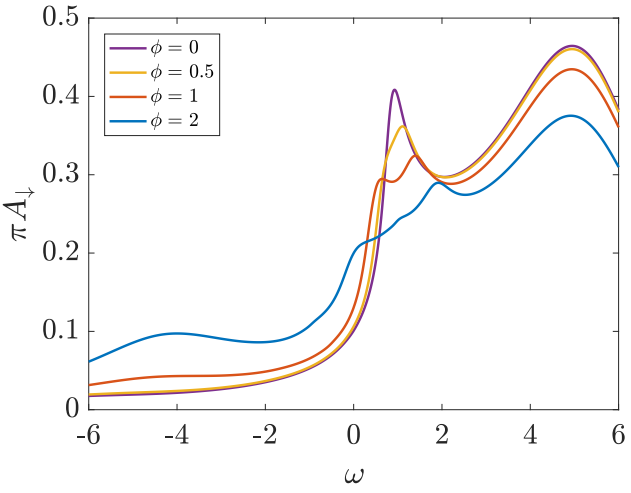

(a)

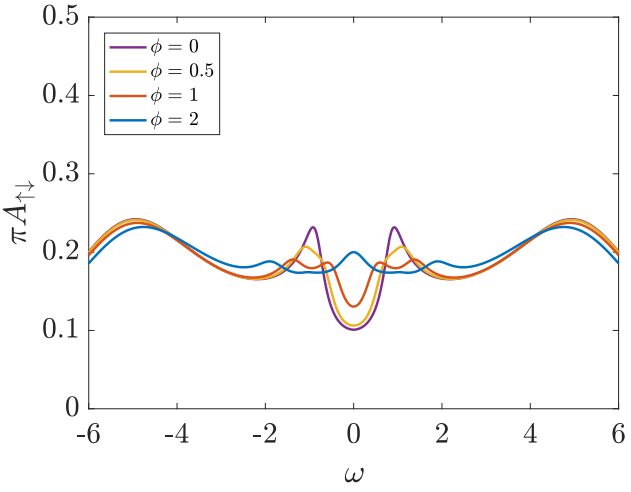

(b)

Figure 5.2: Nonequilibrium spin-resolved (a) and total (b) impurity spectral function for different values of the bias voltage ϕ and fixed magnetic field $B = \Gamma/(|g|\mu_B)$; $T = 0.05\Gamma/k_B \approx T_K/2$. Note that ϕ is in units of Γ/e. Here a larger value of $U = 8\Gamma$ is chosen, in order to resolve the four-peak structure in $A_{\uparrow\downarrow}$.

ϕ and $U = 8$. At $\phi = 0$ the position of the Kondo resonance ω_B is closer to B than for the $U = 6$ case, due to the fact that T_K is smaller here. As a result of the applied bias voltage the shifted Kondo resonance first acquires a broadening and then, starting from $\phi \approx 1$, it gets split. The two peaks have a distance of $\approx \phi$ as expected, but the splitting is not symmetric. The corresponding four-peak structure in the total spectral function can be seen in Fig. 5.2(b) with split peaks at $\omega \simeq \pm B \pm \frac{\phi}{2}$, c.f. [80].

A more direct quantity to be measured experimentally is the differential conductance G across the impurity. In Fig. 5.3 we plot the current j (a) as well as G (b) as a function of the bias voltage for different values of B. The parameters are the same as in Fig. 5.1. To test the approaches, in Fig. 5.6(b) we compare results from AMEA with the ones from the hybrid NRG-tDMRG calculation discussed in Sec. 5.3.4. Results are essentially on top of each other. The magnetic field affects the zero-bias peak in the conductance by first broadening it up to $B \gtrsim T_K$ and then producing a split [54, 60, 80, 122, 123, 125], as observed experimentally [67, 116, 117, 144]. Notice that δ_G, the splitting in G, starts at $B \approx 0.3$ and is slightly delayed in comparison to δ_A, the splitting in $A_{\uparrow\downarrow}(\omega)$, Fig. 5.1(b), which sets in at $B \approx 0.2$. The reason for the delay in the splitting is the averaging of the spectral function in the current integral (5.3.17), which smears out the effect of the split peaks. Since $G = G_\uparrow = G_\downarrow$ at particle-hole symmetry, ϕ_B, the shift in the spin-resolved conductance $G_\downarrow$, exactly fulfills $\phi_B = \frac{\delta_G}{2}$, in contrast to its spectral counterpart, $\omega_B \geq \frac{\delta_A}{2}$. On the other hand, the magnitude of the shift in G, while becoming $\sim B$ for $B \gg T_K$, as shown in Fig. 5.4, it reaches this limit faster than the shift in $A_\downarrow(\omega)$. In fact, Fig. 5.4 suggests that, within the error bars[2] ϕ_B becomes $\sim B$ as soon as it shows up, in contrast to ω_B. This is consistent with experiments [115, 116, 144], which indicate a strictly linear behavior. At $\phi \gg B$ but smaller than the bandwidth the differential conductance reaches a B-independent value of $G \approx 0.27\, G_0$.

Fig. 5.5(a) shows the magnetization $\langle n_\uparrow - n_\downarrow \rangle$ and 5.5(b) the double occu-

[2]The error bars are rough estimates of the error in the numerical derivative of j used to determine G. They are calculated under the conservative assumption that the turning points in $j(\phi)$, which determine the maxima in G, lie at most one voltage point off the calculated value.

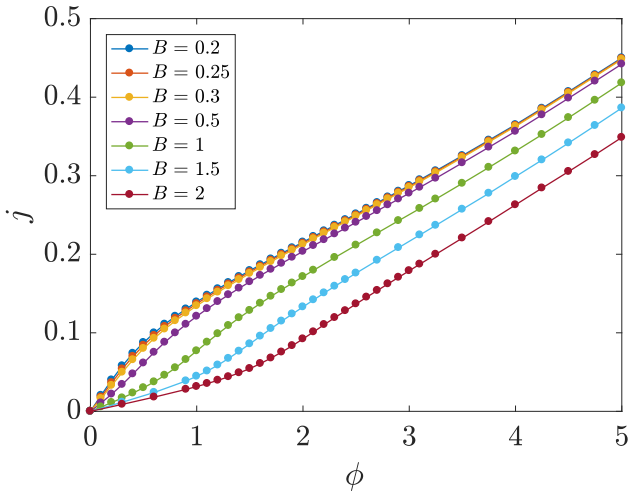

(a)

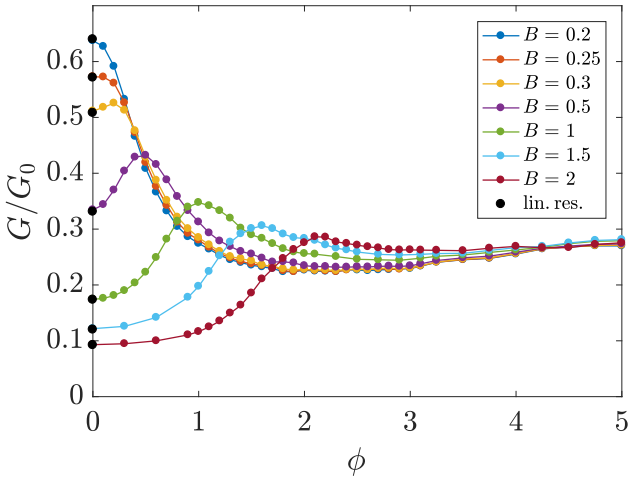

(b)

Figure 5.3: (a) Current-voltage characteristic $j(\phi)$ and (b) differential conductance $G(\phi)$ for different values of the magnetic field B. G is in units of $G_0 = G(T = 0, \phi = 0) = e^2/(\pi\hbar)$. Parameters are as in Fig. 5.1.

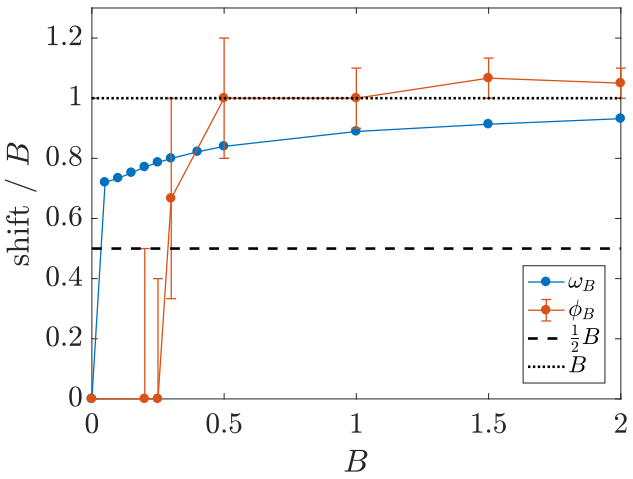

Figure 5.4: Shift ϕ_B of the conductance peak (in Fig. 5.3(b)) and ω_B of the equilibrium spectral function (in Fig. 5.1(a)) divided by the magnetic field B plotted as a function of B. Parameters are as in Fig. 5.1.

pancy $\langle n_\uparrow n_\downarrow \rangle$ at the impurity in dependence of the bias voltage for different magnetic fields. At large magnetic fields $B \gg T_K$ the magnetization shows a plateau for $\phi \lesssim B$ followed by a logarithmic decrease (straight lines in Fig. 5.5(a)), in agreement with previous results, cf. Ref. [123]. At small magnetic fields $B \lesssim T_K$ it starts to decrease for $\phi \approx T_K$. Again, we find a very good agreement between AMEA and NRG-tDMRG, see Fig. 5.6(c). For small magnetic fields the double occupancy has a minimum at $\phi \approx 2$, which seems to be independent of T_K, cf. Ref. [145]. This minimum vanishes at larger magnetic fields as the Zeeman splitting of the local level increases and hence presumably is governed by charge fluctuations.

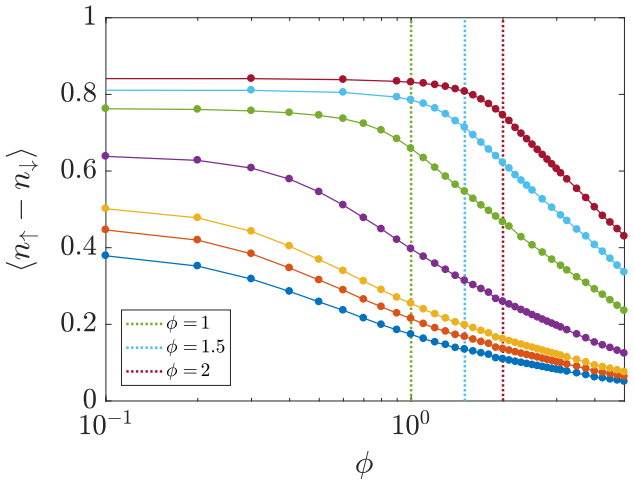

(a)

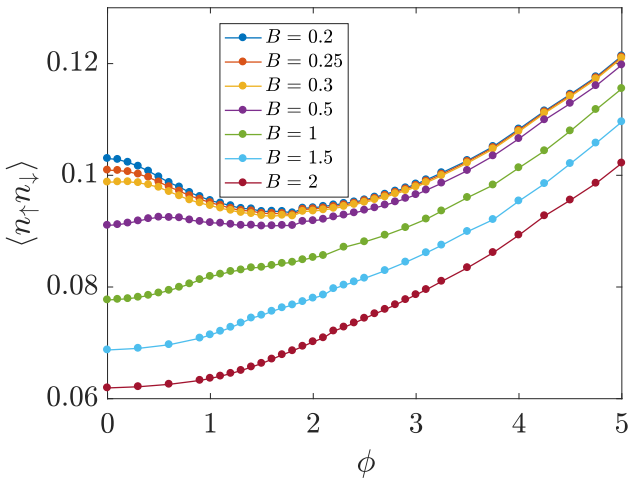

(b)

Figure 5.5: (a) Magnetization and (b) double occupancy as a function of the bias voltage ϕ for different values of the magnetic field B. (b) shares its legend with (a). Dotted lines in (a) correspond to $\phi = B$. Parameters are as in Fig. 5.1.

In Fig. 5.6 we display a comparison of results obtained within AMEA (dashed lines and circles) with results from NRG ((a) dotted lines) and the hybrid NRG-tDMRG scheme discussed in Sec. 5.3.4 ((b,c) squares). Equilibrium spectral functions (a), differential conductance (b) and magnetization (c) curves at different magnetic fields agree remarkably well between the two approaches. One can only see small deviations in the spectral functions at high energies, due to the logarithmic discretization in NRG, which makes it less accurate in this energy region. The inset in (a) shows a zoom around $\omega = 0$, where NRG is known to produce essentially exact results. In this region the two spectral functions deviate by less than 1%. The differential conductance at finite bias, being evaluated from finite current differences (see Sec. 5.3.2) in both approaches, is, in principle, more prone to errors. Nontheless, the results lie essentially on top of each other. On the other hand, as remarked in Sec. 5.3.4, the magnetization from the NRG-tDMRG scheme is not fully converged to the steady state and the data have been extrapolated assuming an exponential decay of the occupancy $\langle n_\sigma \rangle (t)$. For this reason, at high voltages, we can see that the values for the magnetization lie slightly above the AMEA results. While it is, in principle, possible to calculate spectral functions within the NRG-tDMRG scheme, it is unclear at the moment, whether this is numerically feasible. For this reason, we don't provide a comparison between the two approaches in Fig. 5.6.

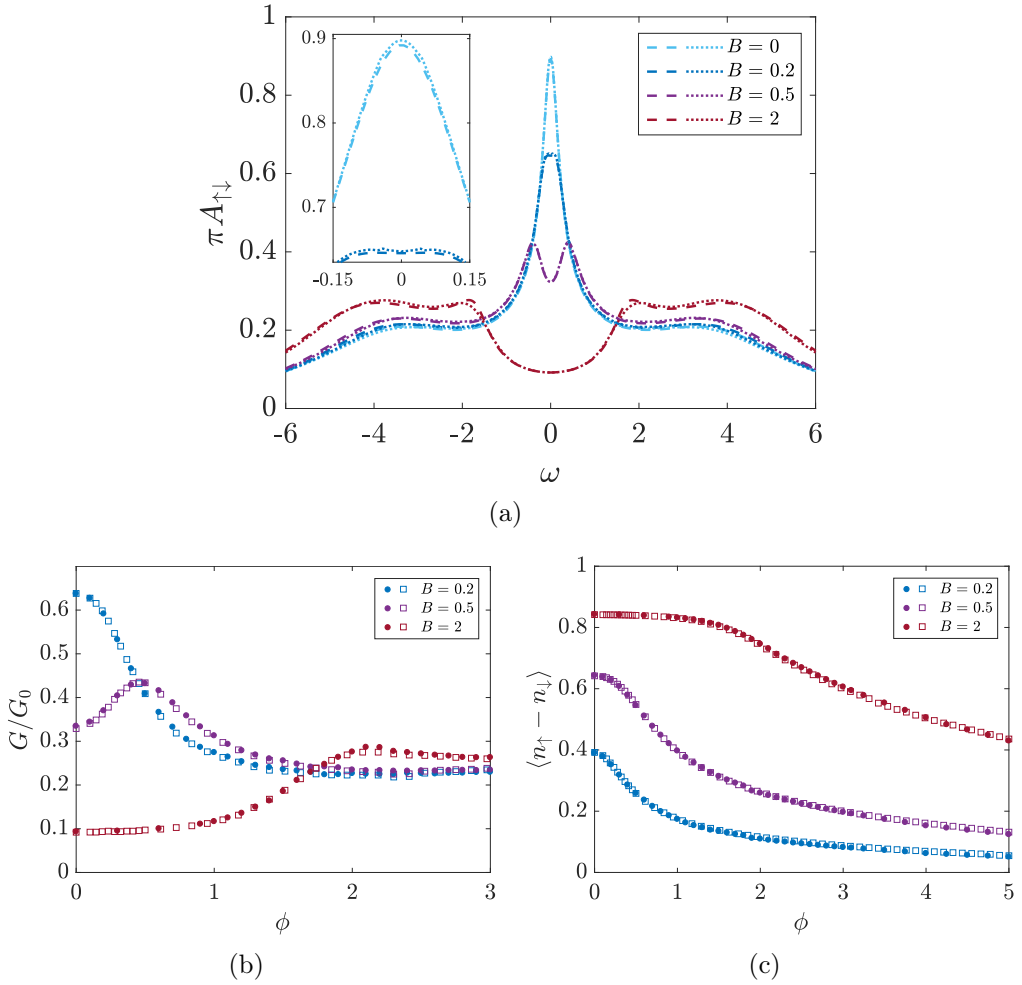

Figure 5.6: Comparison of AMEA with NRG [146] and NRG-tDMRG [30]. (a) Equilibrium total impurity spectral function $A_{\uparrow\downarrow}(\omega)$, (b) differential conductance $G(\phi)$ and (c) magnetization $\langle n_\uparrow - n_\downarrow \rangle (\phi)$ for different values of B. Dashed lines and circles correspond to AMEA, dotted lines to NRG and squares to NRG-tDMRG. Parameters are as in Fig. 5.1.

5.5 Summary and Conclusions

In this paper, we studied the Anderson impurity model out of equilibrium under the influence of a bias voltage ϕ and a magnetic field B. In particular, we addressed the issue of the different behavior of the shift of the Kondo peak in the impurity spectral function and the one in the conductance anomaly as a function of the magnetic field. We also presented explicitly results for the spectral function showing a four-peak structure resulting from the combined effects of B and ϕ.

Our results agree with previous theoretical and experimental results in the known limits $B \ll T_K$ and $B \gg T_K$, while our approach allows us to access the intermediate regime $B, \phi \gtrsim T_K$ as well. The key aspect of our auxiliary master equation approach [22, 63, 64, 83] is that we can obtain very accurate results also for the spectral functions out of equilibrium, which is difficult by other methods. The accuracy of our results in the parameter regime we considered is confirmed by an excellent comparison of spectral functions with NRG at $\phi = 0$ (up to frequencies for which NRG is supposed to yield correct results), and of expectation values with a recently introduced hybrid NRG-tDMRG scheme [30] at finite bias voltages.

The two approaches adopted here, AMEA and the NRG-tDMRG scheme, deal with the challenge of describing the long time behavior of the nonequilibrium SIAM in a different manner. While AMEA explicitly describes an open quantum system and thus is not restricted to finite time scales, the quench approach renormalizes the problem down to the relevant energy scale. In addition, AMEA is able to evaluate the impurity spectral function. While, in principle, this is also possible in the NRG-tDMRG approach, from a numerical point of view, it would be more costly. Therefore, it is unclear at the moment, whether it is realizable in practice. Also for the magnetization AMEA was able to achieve better convergence, especially at high voltages.

In summary, it is convenient to use AMEA, whenever very long time scales are needed, or when information over the full energy range is required, as it is the case in the determination of spectral functions. For example, AMEA is an interesting tool for DMFT in nonequilibrium, where spectral

functions are needed explicitly [22, 25, 73–76]. On the other hand, the NRG-tDMRG approach is more flexible with respect to the parameter regime, as it uses an explicit renormalization of the impurity. In particular, it has proven to be able to describe very strong interactions such as $U/\Gamma = 12$ and zero temperature $T = 0$, see Ref. [30]. AMEA can deal with interactions of the same strength and temperatures down to $T \sim T_K/10$ [64]. Much larger values of U and/or much lower in T are not reachable at the moment, since we are limited in the number of bath sites.[3] This is also the reason, why we could not accurately check the well-known $\sim [\ln (B/T_K)]^{-2}$ behavior of $A_\downarrow(\omega = 0)$ for $B \gg T_K$, Ref. [129] in equilibrium. Our results may be consistent with a logarithmic asymptotics, but, in order to reliably confirm this behavior, we need to consider magnetic fields that are orders of magnitude larger and at the same time $\ll U$. Therefore, at the moment, it may be preferable to use the NRG-tDMRG quench approach, whenever it gets crucial to work in the scaling limit and for very low values of the bias voltage.

The only approximation in AMEA consists in replacing the physical bath hybridization function $\underline{\Delta}$ with an auxiliary one $\underline{\Delta}_{aux}$, so that the accuracy depends on the difference between the two functions. Of course, the corresponding error in the calculated results, e.g. the spectral function, is expected to be strongly frequency dependent, so that regions around the Fermi energies are probably more strongly affected. More specifically, due to the fact that at zero bias the Kondo scale depends exponentially on the $\omega = 0$ DOS, one may expect a corresponding exponential error in this scale. This is probably not yet the case at these moderate values of $U/\Gamma \lesssim 8$ used here, as can be deduced from our results in Ref. [64]. For larger U (and more bath sites), the way to avoid this exponential problem could be to carry out the fit by constraining $\Im\Delta^R_{aux}$ to coincide with $\Im\Delta^R$ at $\omega = \mu_{R/L}$, or in any case require that the fit becomes more accurate around these points.

[3] Work is in progress on improving the Lindblad solver and achieve larger N_B. Notice that the accuracy increases exponentially with N_B.

5.6 Acknowledgments

We would like to thank M. Sorantin, I. Titvinidze and W. von der Linden for fruitful discussions. D.F., A.D. and E.A. were supported by the Austrian Science Fund (FWF) within the projects P26508 and F41 (SFB ViCoM), as well as NaWi Graz. F.S. and J.v.D. were supported by the German-Israeli-Foundation through I-1259-303.10 and NIM. The calculations were partly performed on the D-Cluster Graz and on the VSC-3 cluster Vienna.

Chapter 6

Nonequilibrium pseudogap Anderson impurity model: A master equation tensor network approach

Here, I present the second main paper constituting this thesis [3]. Similar to Ref. [1], it also deals with the Kondo effect of a single, correlated impurity in a fermionic bath, but in Ref. [3], the bath has a pseudogap in the density of states at the Fermi level. This, on the one hand, enriches the physics yielding to the generalized Kondo effect and a quantum phase transition, the numerical treatment, on the other hand, also gets more sophisticated.

To cope with the new challenges, we designed a scheme to obtain the AMEA Lindblad mapping at finite bias voltages from the solution at zero bias. I implemented this scheme following the ideas of E. Arrigoni. M. Sorantin helped with adjusting the python code for the zero-bias mapping to a geometry suitable for MPS treatment. This python code is based on the library tensorflow [147, 148] and it had been implemented by F. Scherr in the course of his Bachelor thesis. To solve the resulting many-body Lindblad problem, E. Arrigoni suggested to develop a novel MPS scheme exploiting spin separation. With support of D. Bauernfeind I designed and implemented

this scheme based on the C++ tensor network library iTensor [149]. D. Bauernfeind also provided the idea to locate the phase boundary with an extrapolation scheme and his equilibrium MPS code for comparison. I performed all calculations and I was the main contributor in writing this paper. The framework for Sec. 6.7 was provided by E. Arrigoni as well as a major revision of this paper. All authors contributed to the discussion and conclusions of the paper and provided revisions. The work was initiated by E. Arrigoni.

In the following, Ref. [3] is included literally in its entity. However, in order to obtain a single, coherent bibliography, the citations are merged into one list of references at the end of this thesis.

6.1 Abstract

We study equilibrium and nonequilibrium properties of the single-impurity Anderson model with a power-law pseudogap in the density of states. In equilibrium, the model is known to display a quantum phase transition from a generalized Kondo to a local moment phase. In the present work, we focus on the extension of these phases beyond equilibrium, i.e. under the influence of a bias voltage. Within the auxiliary master equation approach combined with a scheme based on matrix product states (MPS) we are able to directly address the current-carrying steady state. Starting with the equilibrium situation, we first corroborate our results by comparing with a direct numerical evaluation of ground state spectral properties of the system by MPS. Here, a scheme to locate the phase boundary by extrapolating the power-law exponent of the self energy produces a very good agreement with previous results obtained by the numerical renormalization group. Our nonequilibrium study as a function of the applied bias voltage is then carried out for two points on either side of the phase boundary. In the Kondo regime the resonance in the spectral function is splitted as a function of the increasing bias voltage. The local moment regime, instead, displays a dip in the spectrum near the position of the chemical potentials. Similar features are observed in the corresponding self energies. The Kondo split peaks approximately obey a

power-law behavior as a function of frequency, whose exponents depend only slightly on voltage. Finally, the differential conductance in the Kondo regime shows a peculiar maximum at finite voltages, whose height, however, is below the accuracy level.

6.2 Introduction

The single-impurity Anderson model (SIAM) was originally introduced to address the properties of metals with dilute magnetic impurities, which displayed an unusual resistance minimum upon decreasing the temperature [34, 36]. This effect was termed Kondo effect and it was traced down to the formation of a highly entangled ground state of the model, namely, a singlet state between the localized impurity electron and the conduction electrons of the host metal screening the impurity spin. This has important consequences, such as the existence of a regime, in which physical quantities obey a set of universal scaling laws, which are independent of the microscopic details of the actual physical system. In the Kondo regime, i.e. well below the so-called Kondo temperature T_K, the SIAM also behaves as a Fermi liquid. Above this energy scale, the impurity spin is no longer screened and the model displays a crossover from the Kondo to a local moment (LM) regime. In the impurity spectrum, this crossover is signaled by a strong suppression and broadening of the Kondo resonance, which, however, never completely vanishes. It is important to mention that there is no true quantum phase transition (QPT) in this model [31, 150].

In the last decades, the SIAM has drawn renewed interest, due to its application in dynamical mean-field theory (DMFT), which has paved the way to understand the properties of a variety of correlated materials [71, 151]. It has further drawn attention, due to its capability to capture the physics of quantum dots, which can now be faithfully fabricated in the laboratory [1, 118]. These applications have in common that they usually deal with a structured density of states (DOS) of the host material, instead of a flat one, as in the original model. In contrast to metals, materials with a band gap cannot (fully) display the Kondo effect, since a finite DOS in a small region

around the Fermi energy is crucial for its occurrence. However, there are also materials, such as peculiar semiconductors and superconductors [152, 153], that display a pseudogap (PSG), i.e. a DOS vanishing exactly at the Fermi energy with a certain power-law $\propto |\omega|^r$, but remaining finite, elsewhere. For this type of materials, the interaction of band fermions with a magnetic impurity produces more intriguing effects [81]. The corresponding PSG SIAM displays a rich zero-temperature phase diagram. In particular, for $0 < r < \frac{1}{2}$ it features a second-order QPT [154] from a Kondo screened phase to a LM phase depending on the interplay between the power-law exponent r, the interaction and hybridization strengths. In this model, the depletion of host states at the Fermi energy prevents the impurity spin from being entirely screened by the conduction electrons. As a consequence, the PSG SIAM does not behave as an ordinary Fermi liquid in the Kondo phase. Its behavior is captured by a natural, but non-trivial generalization of Fermi liquid theory, and the phase is referred to as a generalized Kondo (GK) phase. Also in this case, a Kondo scale and a set of universal laws for the physical observables in terms of this scale is found, which is distinct from the ordinary SIAM [81, 82, 155–176].

In this paper, we are interested in understanding the properties of the PSG SIAM, when a bias voltage ϕ is applied to drive the system out of equilibrium [26, 177–183]. This model has been studied in previous works as well with different degrees of approximation and addressing different physical questions. In Ref. [184], the PSG SIAM was studied after a local quench within a time-dependent Gutzwiller variational scheme. The author found that the system thermalizes within the GK phase, but when quenching across the phase boundary, thermalization does not occur, and a highly nontrivial dynamical behavior is observed. Refs. [185, 186] both deal with universal scaling in the nonequilibrium steady state of the PSG Kondo model, employing variants of the renormalization group and large-N techniques, respectively. In the LM phase, close to the phase boundary, Ref. [185] reports universal scaling of the differential conductance, spin susceptibility and conduction electron T matrix as a function of ϕ/T_K. In Ref. [186], on the other hand, it was discovered that the differential conductance, spin susceptibility and

Kondo-singlet strength, reproduce their equilibrium behavior in the scaling regimes of the fixed points of the model, when expressed in terms of a fixed-point specific effective temperature T_{eff}. Ref. [187], in contrast, focuses on the steady state impurity spectrum and differential conductance, the main quantities that also we are interested in within this work. Employing second-order perturbation theory, the authors find a cusp or dip structure in the impurity spectrum in the GK and LM phase, respectively, when a finite bias voltage is applied. However, in Ref. [187], when increasing the bias voltage, these structures remain located at zero frequency and no splitting occurs. According to the authors, this is, because the system is not in the limit of large interaction strength. The results of our present work, while confirming the presence of these features, present a different scenario: the structures do split as a function of voltage. One should point out that, while our calculations are carried out for values of the parameters very close to the ones used in Ref. [187], there is a difference in the way the DOS pseudogap evolves as a function of voltage. More specifically, in Ref. [187] the pseudogap is fixed at zero frequency also at finite bias voltages and only the chemical potentials are shifted by $\pm\phi/2$. In our work, on the other hand, we pin the pseudogap of each lead to the position of the respective chemical potential.

We study the PSG SIAM out of equilibrium by an approach which is non-perturbative, neither in the interaction nor in the hybridization. Specifically, we employ the auxiliary master equation approach (AMEA),[1, 22, 63, 83] in which the nonequilibrium bath is accurately represented by an open quantum system, whose many-body dynamics is controlled by a Lindblad equation. The latter is solved by an efficient matrix product states (MPS) formulation. We start by a benchmark of the approach in equilibrium. Here, in particular, we exploit the power-law exponent of the self energy to find the boundary between the GK and the LM phase. We then carry on with a qualitative analysis of the structure of the spectral function and the self energy out of equilibrium in both the GK and LM regimes. Besides these qualitative aspects, we try to fit a power-law behavior to these quantities in a region around the chemical potentials and investigate, how the corresponding power-law exponents evolve upon increasing the bias voltage. Finally, we address

the behavior of the differential conductance in dependence of the bias voltage. Our method is numerically exact, the main limitation being the fact that the pseudogap exponent in the bath DOS can be reproduced only with a limited resolution. Therefore, we are also limited in the maximum bias voltage, in which our power-law analysis makes sense.

This work is organized as follows: In Sec. 6.3 the model and the solution method are described, starting with the model in Sec. 6.3.1, followed by a small overview about nonequilibrium Green's functions in Sec. 6.3.2 and a description of the auxiliary master equation approach in Sec. 6.3.3. Specifically, we present the Lindblad equation in Sec. 6.3.3.1, discuss the mapping to the auxiliary system in Sec. 6.3.3.2 and introduce the novel MPS scheme in Sec. 6.3.3.3. Sec. 6.3.3.4 presents remarks about physical and auxiliary quantities. Sec. 6.4 contains the results of this work, in particular, the results of the fit, Sec. 6.4.1, and the ones of the many-body solution in equilibrium, Sec. 6.4.2.1, as well as out of equilibrium, Sec. 6.4.2.2. A discussion of the results obtained is found in Sec. 6.5.

6.3 Model and Method

6.3.1 Model

We study the single-impurity Anderson model (SIAM) in as well as out of equilibrium with electronic leads displaying a power-law pseudogap (PSG) in the density of states (DOS). Throughout this paper we use units of $\hbar = e = k_B = 1$. The model is described by the following Hamiltonian,

$$H = H_{\text{imp}} + H_{\text{leads}} + H_{\text{coup}} \,. \tag{6.3.1}$$

H_{imp} is the Hamiltonian of the impurity. It is a single-site Hubbard Hamiltonian with on-site interaction U, accounting for the Coulomb repulsion between electrons, and on-site energy $\varepsilon_f = -\frac{U}{2}$, producing particle-hole (PH) symmetry,

$$H_{\text{imp}} = \sum_{\sigma} \varepsilon_f f_\sigma^\dagger f_\sigma + U n_{f\uparrow} n_{f\downarrow} \,. \tag{6.3.2}$$

$f_\sigma^\dagger/f_\sigma$ creates/annihilates an impurity electron with spin $\sigma \in \{\uparrow,\downarrow\}$ and $n_{f\sigma} = f_\sigma^\dagger f_\sigma$ is the corresponding particle-number operator. H_{leads} is the Hamiltonian of the left and right lead, $\lambda \in \{L, R\}$,

$$H_{\text{leads}} = \sum_{\lambda k\sigma} \varepsilon_{\lambda k} d_{\lambda k\sigma}^\dagger d_{\lambda k\sigma} \,. \tag{6.3.3}$$

It describes a continuum ($N \to \infty$) of noninteracting energy levels $\varepsilon_{\lambda k} = \varepsilon_k + \tilde{\varepsilon}_\lambda$ rigidly shifted symmetrically by half the bias voltage ϕ, so that $\tilde{\varepsilon}_\lambda = \pm\frac{\phi}{2}$. $d_{\lambda k\sigma}^\dagger/d_{\lambda k\sigma}$ are the corresponding creation/annihilation operators. Finally,

$$H_{\text{coup}} = \frac{t'}{\sqrt{N}} \sum_{\lambda k\sigma} \left(d_{\lambda k\sigma}^\dagger f_\sigma + f_\sigma^\dagger d_{\lambda k\sigma} \right) \tag{6.3.4}$$

is the Hamiltonian that describes the coupling of the impurity to the leads via hoppings t'.

We assume that the leads are initially decoupled ($t' = 0$) and in equilibrium at the same temperature T and chemical potentials μ_λ with an occupation given by the Fermi function,

$$f_\lambda(\varepsilon, T) = \frac{1}{1 + \exp\left(\frac{\varepsilon - \mu_\lambda}{T}\right)} \,. \tag{6.3.5}$$

Requiring the (asymptotical) particle density of each lead to be independent of ϕ amounts to setting $\mu_\lambda = \tilde{\varepsilon}_\lambda$.

The leads have a power-law PSG DOS at μ_λ, which we describe with the retarded hybridization functions,

$$\begin{aligned} \Im\Delta_\lambda^R(\omega) &= -\pi \frac{t'^2}{N} \sum_k \delta(\omega - \epsilon_{\lambda k}) \\ &= -\frac{\Gamma}{2} e^{-\gamma(\omega - \tilde{\varepsilon}_\lambda)^2} |\omega - \tilde{\varepsilon}_\lambda|^r \,, \end{aligned} \tag{6.3.6}$$

whose symmetric forms produce a PH symmetric occupation of the leads. Here, Γ is the hybridization strength and $\gamma > 0$ is used to fix the bandwidth.[1]

[1] A Heaviside step function would also fix the bandwidth without distorting the power-

The Keldysh hybridization functions are fixed by the fluctuation-dissipation theorem,

$$\Delta_\lambda^K(\omega) = 2i\ (1 - 2f_\lambda(\omega, T))\, \Im\Delta_\lambda^R(\omega)\,, \tag{6.3.7}$$

and the total hybridization function at the impurity, accounting for both the left and the right lead, $\Delta^\beta(\omega)$ with $\beta \in \{R, K\}$, is given by

$$\Delta^\beta(\omega) = \sum_\lambda \Delta_\lambda^\beta(\omega)\,. \tag{6.3.8}$$

Notice that $\Delta^\beta(\omega)$ encodes the combined effect of H_{leads} and H_{coup} on the impurity. Thus, the properties of the impurity are controlled by $\Delta^\beta(\omega)$ and by H_{imp}, alone.

6.3.2 Nonequilibrium Green's function

Out of equilibrium, there are two independent single-particle Green's functions. We are especially interested in the steady state Green's functions at the impurity. The lesser and the greater one are defined as,

$$\begin{aligned} G_\sigma^<(t) &= \quad i \left\langle f_\sigma^\dagger(t) f_\sigma \right\rangle_\infty\,, \\ G_\sigma^>(t) &= -i \left\langle f_\sigma(t) f_\sigma^\dagger \right\rangle_\infty\,. \end{aligned} \tag{6.3.9}$$

Note that they have only one time argument, since in steady state (indicated by the subscript ∞), the system is time-translation invariant. After a Fourier transform to frequency space,

$$G_\sigma^\alpha(\omega) = \int G_\sigma^\alpha(t) \exp(i\omega t)\, dt\,, \tag{6.3.10}$$

with $\alpha \in \{<, >\}$, these Green's functions may be combined to obtain the spectral function or local impurity DOS and the Keldysh Green's function,

law. We choose the exponential, because AMEA performs better for smooth hybridization functions.

which we are typically interested in,

$$A_\sigma(\omega) = \frac{i}{2\pi}\left[G^>_\sigma(\omega) - G^<_\sigma(\omega)\right] , \tag{6.3.11}$$

$$G^K_\sigma(\omega) = G^>_\sigma(\omega) + G^<_\sigma(\omega) . \tag{6.3.12}$$

From the spectral function the retarded and the advanced Green's function are obtained via the Kramer's Kronig relations.

In the nonequilibrium Green's function formalism $G^R_\sigma(\omega)$, $G^A_\sigma(\omega)$ and $G^K_\sigma(\omega)$ are typically arranged in a 2×2 matrix (Keldysh space), which we indicate by an underline,

$$\underline{G}_\sigma(\omega) \equiv \begin{pmatrix} G^R_\sigma(\omega) & G^K_\sigma(\omega) \\ 0 & G^A_\sigma(\omega) \end{pmatrix} .$$

This has the advantage that Dyson's equation is valid in the same form as in equilibrium,

$$\begin{aligned} \underline{G}^{-1}_\sigma(\omega) &= \underline{G}^{-1}_{0\sigma}(\omega) - \underline{\Sigma}(\omega) , \\ \underline{G}^{-1}_{0\sigma}(\omega) &= \underline{g}^{-1}_{0\sigma}(\omega) - \underline{\Delta}(\omega) . \end{aligned} \tag{6.3.13}$$

Here, $\underline{g}_{0\sigma}$ is the Green's function of the decoupled and noninteracting impurity, the self energy $\underline{\Sigma}(\omega)$ accounts for the interaction, and the hybridization function $\underline{\Delta}(\omega)$ for the coupling to the noninteracting leads.

From the Green's functions defined above, the current across the impurity can be obtained as

$$j_\lambda = \frac{1}{2\pi}\sum_\sigma \int \Re\big(G^R_\sigma \Delta^K_\lambda + G^K_\sigma \Delta^R_\lambda\big)\, d\omega . \tag{6.3.14}$$

In steady state, the left and right-moving current must be identical, $|j_L| = |j_R|$, so we can also compute $j = \frac{1}{2}\left(j_R - j_L\right)$. The differential conductance follows from the current via

$$G = \frac{dj}{d\phi} . \tag{6.3.15}$$

6.3.3 Auxiliary master equation approach

The auxiliary master equation approach (AMEA) is based upon a mapping of the model introduced in Sec. 6.3.1 – which we call *physical* system in the following – consisting of an impurity and an infinite bath, to a finite *auxiliary* open quantum system. The latter consists of the impurity coupled to a small number of $N_B = N - 1$ auxiliary bath sites that are furthermore attached to Markovian environments. The dynamics of the auxiliary system is governed by a Lindblad master equation [63], whose parameters are chosen such that its hybridization function $\underline{\Delta}_{\text{aux}}$ approximates the one of the physical system $\underline{\Delta}_{\text{phys}}$ (Eq. (6.3.8)) as accurately as possible. Upon solving the corresponding many-body Lindblad equation, an approximation for the behavior of the interacting impurity in the physical system is found. We stress that this mapping becomes exponentially exact, upon increasing the number of bath sites $N_B \to \infty$ in the sense that the Lindblad bath provides an exponentially accurate representation of the original Hamiltonian problem [83, 188].

6.3.3.1 Lindblad equation

As outlined in Refs. [63, 86], the Lindblad equation for a fermionic lattice model can be expressed in terms of an ordinary Schrödinger equation in an augmented state space of twice as many sites $2N$,

$$\frac{d}{dt}\,|\rho(t)\rangle = L\,|\rho(t)\rangle\ . \tag{6.3.16}$$

In this augmented space, the density operator is represented by a quantum state $|\rho(t)\rangle$ and the Lindbladian iL plays the role of a non-Hermitian Hamiltonian. For our case,[2] it reads

$$\begin{aligned} iL = &\sum_{\sigma} \boldsymbol{c}_{\sigma}^{\dagger} \begin{pmatrix} \boldsymbol{E} + i\boldsymbol{\Omega} & 2\boldsymbol{\Gamma}^{(2)} \\ -2\boldsymbol{\Gamma}^{(1)} & \boldsymbol{E} - i\boldsymbol{\Omega} \end{pmatrix} \boldsymbol{c}_{\sigma} - 2\,\mathrm{Tr}\,(\boldsymbol{E} + i\boldsymbol{\Lambda}) \\ &+ U \left(n_{f\uparrow} n_{f\downarrow} - \tilde{n}_{f\uparrow} \tilde{n}_{f\downarrow} + \sum_{\sigma} \tilde{n}_{f\sigma} - 1 \right)\ . \end{aligned} \tag{6.3.17}$$

[2] See, e.g., Eqs. (9)-(11) in Ref. [63].

Here, $\boldsymbol{E}$, $\boldsymbol{\Gamma}^{(1)}$ and $\boldsymbol{\Gamma}^{(2)}$ are $N \times N$ matrices holding the parameters of the Lindblad equation yet to be determined by a fit of $\underline{\Delta}_{\text{aux}}$ to $\underline{\Delta}_{\text{phys}}$ and

$$\begin{aligned} \boldsymbol{\Omega} &= \boldsymbol{\Gamma}^{(2)} - \boldsymbol{\Gamma}^{(1)} \,, \\ \boldsymbol{\Lambda} &= \boldsymbol{\Gamma}^{(2)} + \boldsymbol{\Gamma}^{(1)} \,. \end{aligned} \tag{6.3.18}$$

The vector

$$\boldsymbol{c}_\sigma^\dagger = \left(c_{1\sigma}^\dagger, \ldots, c_{N\sigma}^\dagger, \tilde{c}_{1\sigma}^\dagger, \ldots, \tilde{c}_{N\sigma}^\dagger \right) \tag{6.3.19}$$

contains the creation operators $c_{i\sigma}^\dagger$ and $\tilde{c}_{i\sigma}^\dagger$ in the auxiliary system, which is composed of original[3] "nontilde" and additional "tilde" sites. They obey the usual fermionic anticommutation rules. f is the position of the impurity site, which is typically in the center, $f = (N+1)/2$, $n_{f\sigma} \equiv c_{f\sigma}^\dagger c_{f\sigma}$ and $\tilde{n}_{f\sigma}$ analogously.

In this framework, steady state expectation values as well as Green's functions are obtained as[4]

$$\langle A(t)B \rangle = \langle I | A e^{Lt} B | \rho_\infty \rangle \,, \tag{6.3.20}$$

for local impurity operators A, B and times $t \geq 0$. Here, $|\rho_\infty\rangle = \lim_{t\to\infty} |\rho(t)\rangle$ defines the steady state and $|I\rangle$ is the so-called left vacuum,[5]

$$\begin{aligned} |I\rangle &= \sum_{\{\underline{n}\}} |\underline{n}, \underline{\tilde{n}}\rangle \,, \\ |\underline{n}, \underline{\tilde{n}}\rangle &\equiv (-i)^{\sum_{i\sigma} n_{i\sigma}} (c_{1\sigma}^\dagger \tilde{c}_{1\sigma})^{n_{1\sigma}} \ldots (c_{N\sigma}^\dagger \tilde{c}_{N\sigma})^{n_{N\sigma}} \, |0\rangle |\tilde{F}\rangle \,. \end{aligned} \tag{6.3.21}$$

$n_{i\sigma}$ and $|0\rangle$ are the occupation numbers and the vacuum in the nontilde system and $|\tilde{F}\rangle$ is the completely filled Fock state in the tilde system. Eqs. (6.3.16)-(6.3.21) describe the so-called super-fermion (SF) representation.

[3] "original" refers to Eqs. (9)-(11) in Ref. [63].

[4] Here, we have used the fact that $\langle I | L = 0$.

[5] This representation of $|I\rangle$ follows from Eq. (13) in Ref. [86] via particle-hole transformation.

6.3.3.2 Mapping procedure

The mapping to the auxiliary system is outlined in Refs. [2, 83] and we sketch it only briefly, here. Starting from proper initial values, the parameters $\boldsymbol{E}_{ij}, \boldsymbol{\Gamma}^{(1)}_{ij}, \boldsymbol{\Gamma}^{(2)}_{ij}$ are adjusted by minimizing a suitable [63, 83] cost function. This cost function punishes deviations between the auxiliary and the physical hybridization function and, in general, both the retarded and Keldysh component contribute. Its evaluation involves only the solution of a non-interacting problem, which is computationally cheap. In this paper, the optimizaton of the Lindblad parameters is carried out with the ADAM [147] algorithm as implemented in the python library tensorflow [148].

In principle, the best fit is obtained by allowing the Lindblad parameters to connect all pairs of lattice sites [83]. However, employing matrix product states (MPS) as solver for the many-body problem, as described in Sec. 6.3.3.3, it is convenient to adopt a one-dimensional geometry, which minimizes the entanglement. Specifically, here we adopt a chain geometry with the impurity in the center. In this case, the optimal solution numerically turns out to be such that all sites to the left (right) of the impurity have $\boldsymbol{\Gamma}^{(2)} = 0$ ($\boldsymbol{\Gamma}^{(1)} = 0$) and, therefore, are almost completely empty (full) [64]. This situation is particularly convenient for the MPS many-body solution, since it prevents the propagation of entanglement, as discussed in Ref. [64]. In addition, knowing this fact, it is then sufficient to fit the retarded component of the hybridization function, only, as explained in App. 6.7.1.

We start from the zero-bias, $\phi = 0$, i.e. equilibrium situation and perform the fit as discussed above. The important physics obviously occurs in the region around $\omega = 0$ and is controlled by the power-law exponent r. Thus, it is particularly important to have an accurate fit there. In order to achieve this, we introduce a weight in the cost function, which is twice as large on $|\omega| \leq 1$ than on $|\omega| > 1$. For nonzero ϕ, we can construct the nonequilibrium fit from the equilibrium one, as outlined in App. 6.7.2. This has the advantage that the accuracy of the fit to reproduce the power-law is independent of the bias voltage, which is crucial, in order to faithfully investigate the crossover to finite voltage.

6.3.3.3 Matrix product states implementation

We solve the many-body Lindblad equation employing matrix product states (MPS) in combination with the time-dependent density matrix renormalization group (tDMRG) algorithm [108, 109]. MPS are especially suited for one-dimensional problems, where they can provide an efficient representation with a small bond dimension. In particular, ground states of one-dimensional gapped closed systems are conveniently expressed as MPS [92]. On the other hand, also steady states and Green's functions of open quantum systems in a chain geometry are reproduced accurately using MPS and the entanglement remains limited [64]. We decided to employ tDMRG for the time evolution here, since it is conveniently implemented with the C++ tensor network library iTensor [149].

Within AMEA, a chain geometry naturally results from combining a non-tilde and a tilde site associated with an index i, according to Eq. (6.3.19), to a single effective site with a local Hilbert space dimension of $d = 16$ [64], see Fig. 6.1. Since the SIAM couples opposite spins only at the impurity, it is convenient to separate spin-up and spin-down degrees of freedom [189], which reduces the local Hilbert space dimension back to $d = 4$. Fig. 6.1 shows the effective sites we use in this work (lower panel) and sketches the steps to obtain them. Note that in this arrangement, the Hubbard interaction is on the bond between the spin-down and spin-up impurity site. Furthermore, it is necessary to introduce two long-range terms between the empty bath sites and the impurity, violating the linear geometry.

We encode the left vacuum $|I\rangle$ as well as a proper initial state $|\rho(t=0)\rangle$ as MPS on these effective sites. We choose $|\rho(0)\rangle \propto |I\rangle$, since this has proved convenient in our previous work [1, 64]. Taking

$$\begin{aligned} &|n_{1\downarrow}\tilde{n}_{1\downarrow}\dots n_{f-1\downarrow}\tilde{n}_{f-1\downarrow}n_{N\downarrow}\tilde{n}_{N\downarrow}\dots n_{f\downarrow}\tilde{n}_{f\downarrow}\rangle \\ \otimes\, &|n_{f\uparrow}\tilde{n}_{f\uparrow}\dots n_{N\uparrow}\tilde{n}_{N\uparrow}n_{f-1\uparrow}\tilde{n}_{f-1\uparrow}\dots n_{1\uparrow}\tilde{n}_{1\uparrow}\rangle \end{aligned} \tag{6.3.22}$$

as basis states, we can express the corresponding expansion coefficients

$\psi(\{n_{i\sigma}, \tilde{n}_{i\sigma}\})$ of any required state as products of local matrices,

$$\begin{aligned}\psi(\{n_{i\sigma}, \tilde{n}_{i\sigma}\}) = &\boldsymbol{A}^{n_{1\downarrow}\tilde{n}_{1\downarrow}} \dots \boldsymbol{A}^{n_{f-1\downarrow}\tilde{n}_{f-1\downarrow}} \\ &\times \boldsymbol{A}^{n_{N\downarrow}\tilde{n}_{N\downarrow}} \dots \boldsymbol{A}^{n_{f\downarrow}\tilde{n}_{f\downarrow}} \\ &\times \boldsymbol{A}^{n_{f\uparrow}\tilde{n}_{f\uparrow}} \dots \boldsymbol{A}^{n_{N\uparrow}\tilde{n}_{N\uparrow}} \\ &\times \boldsymbol{A}^{n_{f-1\uparrow}\tilde{n}_{f-1\uparrow}} \dots \boldsymbol{A}^{n_{1\uparrow}\tilde{n}_{1\uparrow}} .\end{aligned} \tag{6.3.23}$$

In case of $|I\rangle$, only matrices with $n_{i\sigma} = 1 - \tilde{n}_{i\sigma}$ are nonzero. Specifically, comparing with Eq. (6.3.21), the corresponding expansion coefficients read

$$\psi(\{n_{i\sigma}, \tilde{n}_{i\sigma}\}) = \prod_{i\sigma} \delta_{n_{i\sigma}, 1-\tilde{n}_{i\sigma}} (-i)^{n_{i\sigma}} , \tag{6.3.24}$$

resulting in the 1×1, i.e. scalar matrices $\boldsymbol{A}^{01} = 1$ and $\boldsymbol{A}^{10} = -i$. Having expressed the relevant states as MPS, we can proceed with the time evolution of the auxiliary system.

In tDMRG the time evolution of the system, $|\rho(t)\rangle = \exp(Lt)\,|\rho(0)\rangle$, is decomposed into a Trotter sequence of small time evolutions on bonds induced by gates. After the application of a gate, the original structure of the MPS, Eq. (6.3.23), is restored with a singular value decomposition. As usual at this step, the smallest singular values are neglected defining a truncated weight, which is the sum of all discarded squared singular vales. Then the next gate may be applied in the same way [92].

Fig. 6.2 shows the sequence of gates we use in this work to evolve one time step Δt. There are five layers, labelled "odd", "even" and "swap", and the gates within them are displayed as boxes. In order to understand them, we identify the following terms as building blocks of the Lindbladian, Eq. (6.3.17),

$$\begin{aligned} iL_{i\sigma j\sigma} = &\left(\boldsymbol{E} + i\boldsymbol{\Omega}\right)_{ij} c^\dagger_{i\sigma} c_{j\sigma} - 2\boldsymbol{\Gamma}^{(1)}_{ij} \tilde{c}^\dagger_{i\sigma} c_{j\sigma} \\ &+ 2\boldsymbol{\Gamma}^{(2)}_{ij} c^\dagger_{i\sigma} \tilde{c}_{j\sigma} + \left(\boldsymbol{E} - i\boldsymbol{\Omega}\right)_{ij} \tilde{c}^\dagger_{i\sigma} \tilde{c}_{j\sigma} , \\ iL_{f\uparrow f\downarrow} = &\, U\left(n_{f\uparrow} n_{f\downarrow} - \tilde{n}_{f\uparrow}\tilde{n}_{f\downarrow} + \tilde{n}_{f\uparrow} + \tilde{n}_{f\downarrow}\right) . \end{aligned} \tag{6.3.25}$$

Within the odd layers, all on-site terms in Eq. (6.3.25) as well as the two-

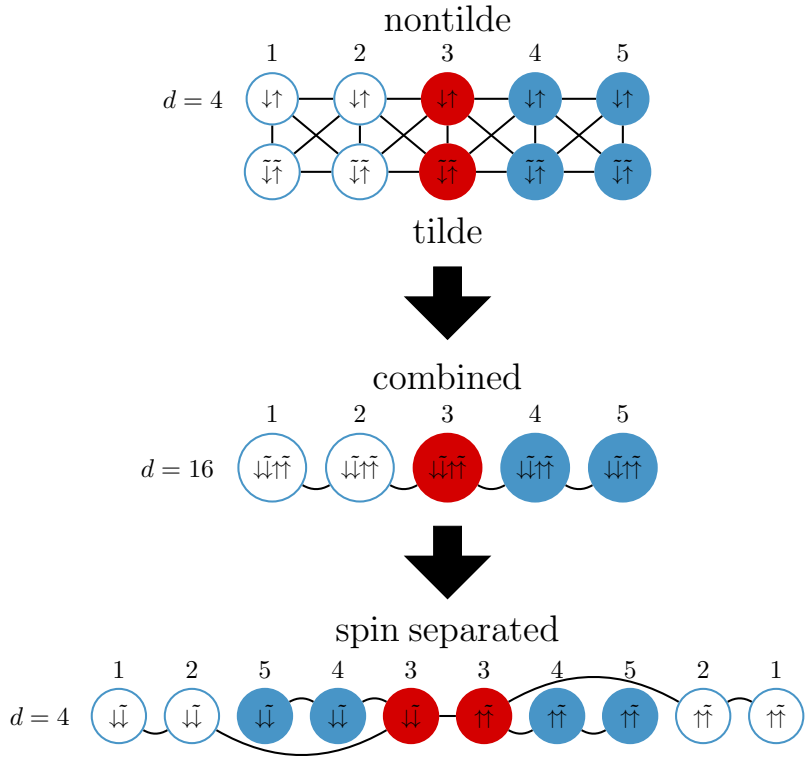

Figure 6.1: Construction of effective sites for the MPS time evolution. The impurity sites are displayed as red circles, the full and empty bath sites as blue and white ones. As discussed in the text, by "full" and "empty" we mean sites for which $\mathbf{\Gamma}^{(1)} = 0$ or $\mathbf{\Gamma}^{(2)} = 0$, respectively, for details, see App. 6.7.1. Each site is labelled with an index and its spin and tilde degrees of freedom. The upper panel of this figure shows the sites and their couplings occurring in the Lindblad equation in the augmented state space. Here, the upper (lower) part of this ladder structure is formed by nontilde (tilde) sites. Lines connecting these two sets of sites represent Γ terms, while lines within the same set are hoppings. The central panel shows the effective sites used in Ref. [64] that result from combining nontilde and tilde sites with the same index. Finally, the lower panel shows the effective sites used in this work that result from the combined sites by separating the spin degrees of freedom. The advantage of this representation is that the local Hilbert space has a dimension of 4, instead of 16 as in our previous work. On the other hand, it introduces two long-range hopping terms.

site terms on every second bond, according to Fig. 6.2, including the impurity bond, are grouped, exponentiated and applied as gates, see Eq. (6.3.26). In the even layers, the two-site gates on the remaining bonds are applied, excluding the long-range bonds between the impurity and the empty baths, which are taken care of in the swap layer [92, 110]. In the swap layer, the innermost sites of the empty baths are swapped with their nearest neighbors, i.e. they change positions, until they are next to the impurity sites. Then the time evolution gates are applied, before they are swapped back to their original positions. Swap gates are displayed as crossing time lines. Summarizing:

$$\begin{aligned}
\text{odd}: \quad & \begin{cases} \exp\left[(L_{i\sigma j\sigma} + L_{j\sigma i\sigma} + L_{i\sigma i\sigma} + L_{j\sigma j\sigma})\frac{\Delta t}{2}\right], \\ \qquad (i,j) = \{(1,2),(4,5),\cdots\} \\ \exp\left[(L_{f\uparrow f\downarrow} + L_{f\uparrow f\uparrow} + L_{f\downarrow f\downarrow})\frac{\Delta t}{2}\right] \end{cases} \\
\text{even}: \quad & \exp\left[(L_{i\sigma j\sigma} + L_{j\sigma i\sigma})\frac{\Delta t}{2}\right], \\
& \qquad (i,j) = \{(3,4),\cdots\} \\
\text{swap}: \quad & \exp\left[(L_{f-1\sigma f\sigma} + L_{f\sigma f-1\sigma})\,\Delta t\right]
\end{aligned} \tag{6.3.26}$$

To complete the time step, also the constant in Eq. (6.3.17) has to be taken into account, so we multiply the MPS with $\exp\{i\Delta t\,[2\mathrm{Tr}\,(\boldsymbol{E} + i\boldsymbol{\Lambda}) + U]\}$.

Notice that the described sequence of gates may be employed, provided that N_B is even, as reasonable at PH symmetry, otherwise the sequence needs to be adjusted accordingly. Since this sequence is derived from a second-order Suzuki-Trotter decomposition, an error $\mathcal{O}(\Delta t^3)$ is acquired in the time evolution, which is further proportional to the commutators of the Lindbladians, Eq. (6.3.26), in different layers. Additionally, there is an error from the truncation of the singular values after the application of each gate.

In this work, we employ the tDMRG scheme as follows: We first determine the steady state $|\rho_\infty\rangle \propto \exp(Lt^*)\,|I\rangle$[6] via time evolution of the initial state with tDMRG up to a time t^*, for which expectation values of

[6] $\langle I|\rho(t)\rangle = 1$ must be fulfilled for all t, since this corresponds to $\mathrm{Tr}\,\rho(t) = 1$.

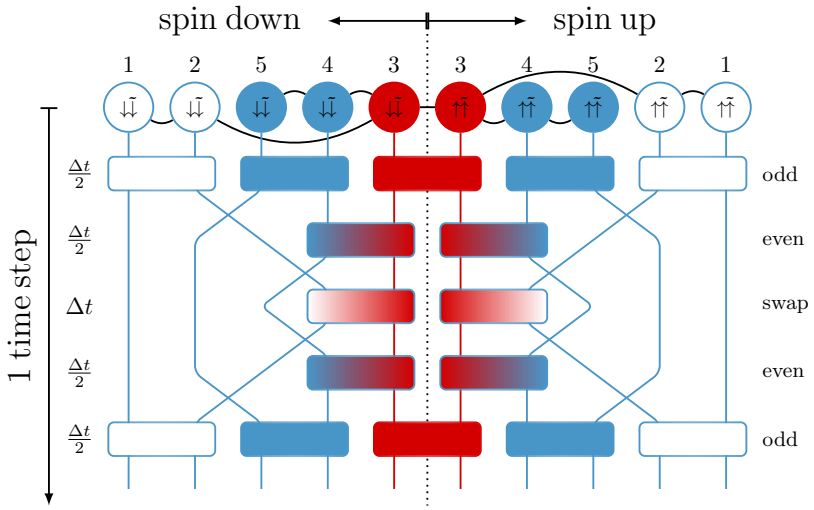

Figure 6.2: Single step in the MPS time evolution of the (PSG) SIAM with separated spin degrees of freedom. The impurity sites are represented as red circles, the full and empty bath sites as blue and white ones. The same colouring also classifies the time evolution gates that are represented as boxes. A time evolution step Δt consists of five layers, labelled "odd", "even" and "swap". In each layer, a site $i\sigma$, with index i and spin σ, is touched only by one gate. In the swap layer, swap gates displayed as crossing time lines are employed to cope with the long-range couplings between the empty bath sites and the impurity sites.

static observables, such as single and double occupancies, are converged. Afterwards, we compute, e.g., the lesser impurity Green's function, $G^<_\sigma(t) = i\,\langle I|c^\dagger_{f\sigma}\exp(Lt)c_{f\sigma}|\rho_\infty\rangle$, by applying $c_{f\sigma}$ to the steady state, employing tDMRG again, applying $c_{f\sigma}$ to $|I\rangle$ and calculating the overlap. $G^<_\sigma(\omega)$ is obtained in the frequency domain via Fourier transformation of $G^<_\sigma(t)$ after linear prediction [190].

6.3.3.4 Physical versus auxiliary quantities

The observables obtained directly by the MPS treatment of the auxiliary system are called "auxiliary" quantities in the following. The auxiliary Green's functions are used as an approximation for the Green's functions of the physical model. As discussed, this approximation becomes exponentially exact upon increasing the number of bath sites. We can get an even better approximation by extracting the self energy from Dyson's equation for the auxiliary system, assuming $\underline{\Sigma}_{\text{phys}}(\omega) \approx \underline{\Sigma}_{\text{aux}}(\omega)$ and reentering Dyson's equation with the (approximated) physical self energy and the (exact) physical hybridization function. The Green's functions extracted in this way are refereed to as "physical" in the following.

6.4 Results

Here, we present results obtained with AMEA for the parameters $r = 0.25$, $U = 6$, $T = 0.05$ and $\Gamma = 1$ in the generalized Kondo (GK) phase and $\Gamma = 0.25$ in the local moment (LM) phase. In equilibrium, we compare the results with the ones obtained with a direct MPS time evolution of the Hamiltonian, Eq. (6.3.1), at $T = 0$ [189]. For clarity, we refer to this procedure as "Hamiltonian MPS" (HMPS), in order to distinguish it from AMEA, which is also treated via MPS. Of course, HMPS cannot be used to achieve the steady state, since the system is finite. Since HMPS is faster, we also provide equilibrium results for different values of r and U obtained with that approach.

6.4.1 Fit

We start by fitting the equilibrium hybridization function with the auxiliary Lindblad system, as described in Sec. 6.3.3.2. As discussed above, we use a weight function, such that the hybridization function is reproduced better at low frequencies. We also concentrate on reproducing the power-law as accurately as possible, while putting less emphasis on the multiplicative factors as well as on the large-ω behavior. The results of the fit are displayed in Fig. 6.3.

From Fig. 6.3(a) we can see that the auxiliary (AMEA) retarded hybridization function accurately matches the physical one for $|\omega| \gtrsim 0.2$, which, on the other hand, behaves approximately as

$$\Im\Delta^R(\omega) \propto |\omega|^r \tag{6.4.1}$$

for $|\omega| \lesssim 1.2$. It follows that $\Im\Delta^R_{\text{aux}}(\omega)$ displays a power-law on the interval $\Omega \equiv (0.2 < |\omega| < 1.2)$, but the exponent is slightly underestimated. In fact, a fit by Eq. 6.4.1 on the interval Ω yields $r' = 0.23$, whereas its value should be equal to $r = 0.25$. Note that the behavior of $-\Im\Delta^R_{\text{aux}}(\omega)$ is qualitatively acceptable[7] even down to $|\omega| \approx 0.02$, which is one order of magnitude smaller than the lower edge of the power-law interval Ω. Below this value, though, it bends towards a constant, $-\Im\Delta^R_{\text{aux}}(\omega = 0) \approx 0.39\Gamma$, instead of going to zero. Fig. 6.3(a) also shows the hybridization function used in HMPS, for comparison. Here, it is plotted using a Lorentzian broadening of $\eta = 0.1$.[8] It features a good representation of the power-law, roughly on the same interval Ω as AMEA, but $-\Im\Delta^R_{\text{HMPS}}(0)$ is larger for this value of η. Note that for HMPS many more bath sites are necessary to get such a high resolution. Specifically, on $|\omega| < 10$ we use $N_B = 1301$ for HMPS in comparison to $N_B =$

[7] in the sense that it is decreasing

[8] In HMPS, in the Fourier transform of the Green's function, Eq. (6.3.10), a modified kernel $\exp(i\omega t - \eta|t|)$ with a finite broadening η is used, instead of the mathematically exact limit $\eta \to 0$. Note that in ω-space this is equivalent to a convolution of the exact (finite size) result with a Lorentzian distribution of width η. Here, η is chosen such that the hybridization function, the spectral function and the self energy are smooth.

10 or 20 for AMEA[9] to achieve roughly the same accuracy. In Fig. 6.3(b) the auxiliary distribution function f_{aux}, obtained from $\Delta^R_{\text{aux}}(\omega)$ and $\Delta^K_{\text{aux}}(\omega)$ via Eq. (6.3.7), is plotted. It compares well to the Fermi function, i.e. the distribution function in the physical system.

Since Ω identifies the interval, where we can faithfully represent the power-law in AMEA and in HMPS with an exponent $r' \approx r$, it is also the interval, where we should study other quantities, such as the spectral function $A(\omega)$ or the self energy $\Sigma^R(\omega)$. With a bias voltage applied, the interval Ω shrinks to

$$\Omega(\phi) = \left(0.2 + \frac{\phi}{2} < |\omega| < 1.2 - \frac{\phi}{2}\right), \quad \text{for } \phi \geq 0\,, \tag{6.4.2}$$

since the hybridization functions Δ^R_L and Δ^R_R are shifted by ϕ with respect to each other. This also limits the values of the bias voltage, in which we can reasonably estimate a power-law behavior to $\phi \lesssim 0.6$. This estimate is obtained by assuming that we need a frequency interval of width $\epsilon = 0.4$, in which to fit power-law exponents.

6.4.2 Many-body solution

After carrying out the fit, we solve the resulting Lindblad equation (or Schrödinger equation in case of HMPS) and determine the steady state (or just equilibrium for HMPS) Green's functions, as described in Sec. 6.3.3.3 (or Ref. [189]). We are especially interested in the spectral function as well as the self energy, as there are predictions about their behavior in equilibrium [165], and in the differential conductance. Unless stated otherwise, our plots display the physical spectral functions and not the auxiliary ones, acoording to the definition in Sec. 6.3.3.4. Due to the Trotter and truncation errors, the MPS results break PH symmetry. Therefore, the curves we show are PH symmetrized and the shadings indicate an estimate of these errors obtained from the deviations from PH symmetry, see App. 6.8 for a more detailed discussion.

[9] $N_B = 20$ in nonequilibrium, see App. 6.7

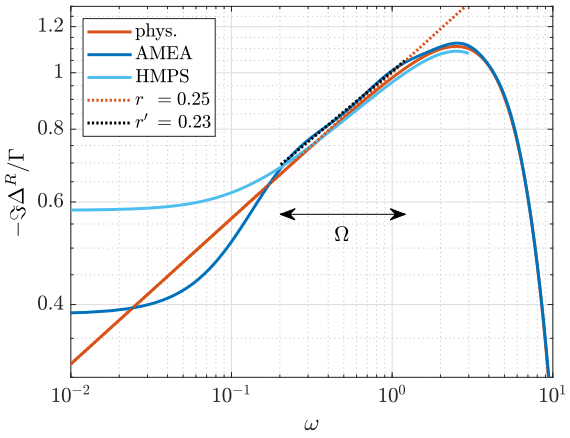

(a)

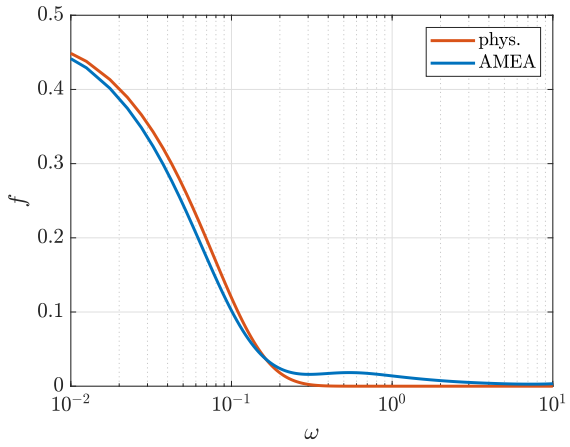

(b)

Figure 6.3: Equilibrium ($\phi = 0$) fit results. (a) Retarded hybridization function $-\Im\Delta^R(\omega)$ in units of the hybridization strength Γ and (b) distribution function f determined from $\Im\Delta^R$ and $\Im\Delta^K$ via Eq. (6.3.7). The power-law exponent r' is obtained by fitting the AMEA hybridization function with Eq. (6.4.1) on the interval Ω. The same procedure applied to the HMPS result yields quite the same exponent (up to a deviation of ≈ 0.01). $|\omega|^r$ is plotted for comparison, see Eq. (6.4.1). These curves are hardly distinguishable (black vs. red dots).

6.4.2.1 Equilibrium case

The equilibrium case has been extensively studied in the literature [81, 82, 159–176]. It is well established that in a certain range of r, U and Γ the system displays a Kondo-like behavior, the so-called generalized Kondo effect. In the GK phase, the spectral function and the retarded self energy are supposed to show a power-law behavior at small frequencies $|\omega|$ [165],

$$A(\omega) \propto |\omega|^{-s}, \quad s = r\,, \tag{6.4.3}$$

$$\Im\Sigma^R(\omega) \propto |\omega|^{\kappa}, \quad \kappa > r\,. \tag{6.4.4}$$

First, we would like to address the question, how these properties are affected by the fact that AMEA cannot reproduce the pseudogap exactly down to asymptotically low energies. Therefore, we study one set of parameters in the GK phase, according to the phase diagram in Fig. 5, Ref. [166], which is reproduced in Fig. 6.6 of the present paper. Specifically, we solve the many-body problem for $r = 0.25$, $U = 6$ and $\Gamma = 1$ (and a small temperature $T = 0.05$) and compute the spectral function and retarded self energy. Then we fit Eqs. (6.4.3) and (6.4.4) to these quantities on the interval Ω and extract the corresponding power-law exponents. In the following, we denote their numerical values as s' and κ', respectively. The results are plotted in Fig. 6.4 together with the ones obtained by an HMPS treatment of the model for $T = 0$ and $\eta = 0.1$.

From the results plotted in Fig. 6.4 we conclude that exponents extracted from the two methods, AMEA and HMPS, agree quite well. We can also see that $\kappa' > r$ is fulfilled, but s' is significantly larger than the predicted value r. This is, because the interval Ω used to determine the exponent lies at too large frequencies $|\omega|$.[10] On the other hand, it is not reasonable to go to smaller $|\omega|$ values, since the power-law is not well represented there in the hybridization function, see Fig. 6.3(a). Possibly, a more appropriate

[10] This is checked easily by calculating the $U = 0$ spectral function for the exact physical hybridization function. The outcome shows that we need a good representation of the power-law exponent in $\Im\Delta^R$ down to $|\omega|$ values that are at least $1-2$ orders of magnitude smaller than the lower edge of Ω and this is not feasible within AMEA, neither HMPS at the moment.

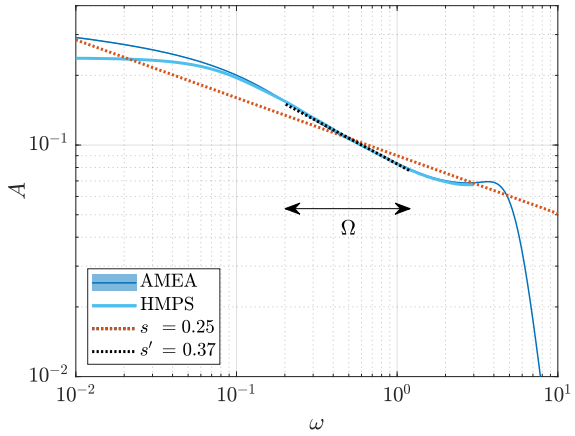

(a)

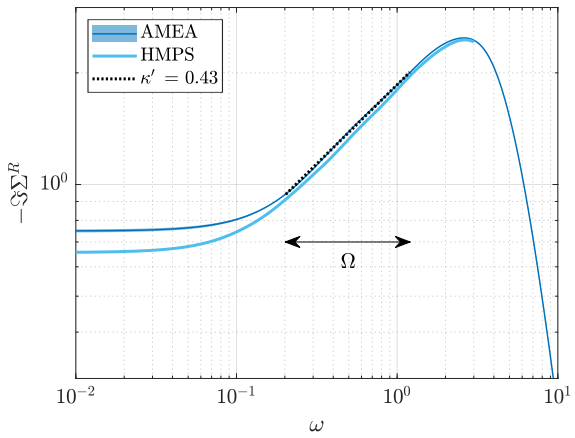

(b)

Figure 6.4: Equilibrium ($\phi = 0$) (a) spectral function $A(\omega)$ and (b) retarded self energy $-\Im\Sigma^R(\omega)$ in the GK phase. The power-law exponents s' and κ' are obtained by fitting the AMEA results with Eqs. (6.4.3) and (6.4.4) on the interval Ω. The same procedure applied to the HMPS results yields quite the same exponents (up to a deviation of ≈ 0.01). A power-law $\propto |\omega|^{-s}$ is plotted for comparison, see Eq. (6.4.3). The error shadings, hardly to be seen in this figure, are estimates of the PH symmetry errors, see App. 6.8.

way to proceed here would be to use a logarithmic energy discretization as in NRG. However, without the possibility to integrate out high-energy degrees of freedom, this is no use here, and indeed the AMEA fit becomes quite unstable.

It is also well established in the literature that upon increasing U, the system undergoes a QPT from the GK to an LM phase, where the Kondo-like behavior is absent. Our next goal is to reproduce the phase boundary from Fig. 5 in Ref. [166], i.e. to numerically calculate the critical value U_c, which depends on r and Γ, see Fig. 6.6. We would like to exploit Eqs. (6.4.3) and (6.4.4) for that purpose. Since we find that it is difficult to extract the correct exponent s' from the impurity spectral function, we choose to use the one of the self energy κ', instead. In Ref. [165] it is shown that, in the GK phase, this exponent must be larger than r. In the equilibrium case, it is convenient to use the HMPS solver rather than AMEA for the numerical calculations. In Figs. 6.3 and 6.4 we have already checked that both methods provide essentially the same values for the exponents up to a small deviation (≈ 0.01). The HMPS solver is suitable for the equilibrium case, and, since it is based on a Hamiltonian time evolution, it is easier to employ and a bit faster, even for this large number of 1301 bath sites.

Specifically, we compute the Green's functions for different values of the interaction strength U and extract the corresponding self energy from Dyson's equation (6.3.13) for various Lorentzian broadenings η. Then we fit $\Im\Sigma^R(\omega)$ on Ω and determine κ' as a function of η. The results of this procedure are illustrated for $r = 0.25$ in Fig. 6.5(a). We can see that κ' displays a significant dependence on η (in contrast to r' and s')[11] and that it is almost a linear function of η for all considered values of U. In order to extract the result without artificial broadening, we perform a linear extrapolation, $\kappa'_0 = \kappa'(\eta \to 0)$. In Fig. 6.5(b) the obtained values for κ'_0 are plotted and we find again an almost linear dependence on the interaction strength. According to the condition in Eq. (6.4.4), the system should leave the GK phase at the value of U for which $\kappa'_0 = r$. Thus, we perform a second linear

[11] This is, due to the fact that the self energy is extracted from an inversion of the Green's function.

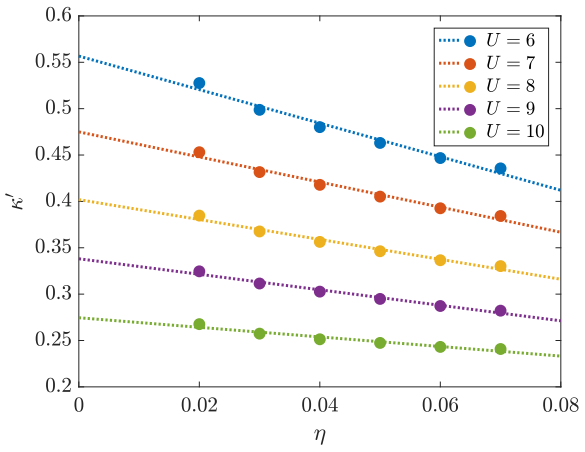

(a)

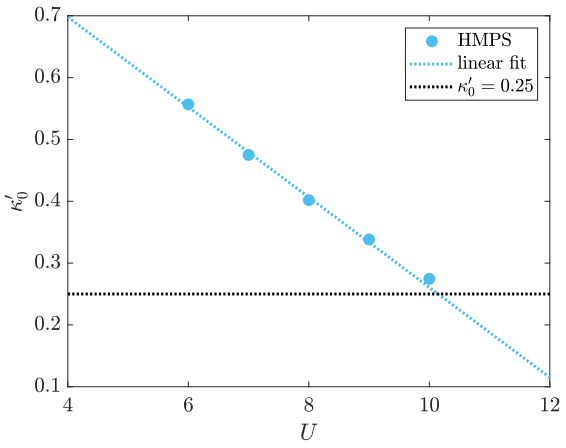

(b)

Figure 6.5: Determination of the phase boundary by linear extrapolation of the power-law exponent κ' of the HMPS self energy in the GK phase. First, (a) κ' is extrapolated to vanishing values of the broadening η to extract $\kappa_0' = \kappa'(\eta \to 0)$ for various values of the interaction strength U. Second, (b) the critical interaction strength is determined from a second extrapolation, $U_c = U(\kappa_0' \to r)$.

extrapolation to extract the critical interaction strength as $U_c = U(\kappa_0' \to r)$.

The phase boundary estimated in this way agrees well with the ones obtained by the numerical renormalization group, see Fig. 6.6. In particular, the deviations within the results obtained from different NRG calculations are of the same size as the deviation of the HMPS results from the NRG results for the considered values of r.[12] It is notable, though, that the HMPS scheme tends to overestimate the critical interaction strength, yielding slightly smaller values U_c^{r-1} in Fig. 6.6. This could be improved by taking into account that $\kappa'(\eta)$ is not strictly a linear function. By accounting for its curvature, one obtains slightly larger values κ_0' (see Fig. 6.5(a)). This, in turn, results in smaller critical interaction strengths (see Fig. 6.5(b)) and thus in larger values of U_c^{r-1}, closer to the corresponding NRG results. From the literature it is known that the GK phase can occur only for $0 < r < 0.5$, see e.g. Ref. [82]. Close to the phase boundary at $r \to 0.5$, the HMPS calculations are more involved, the quantities $\kappa'(\eta)$ and $U(\kappa_0')$ are much more difficult to obtain and the extrapolation scheme described above breaks down. Therefore, in Fig. 6.6 the HMPS results are plotted only up to $r = 0.45$.

It is remarkable that our results reproduce the NRG phase boundary to this level of accuracy, even though the low energy part of the bath hybridization function used in our calculation is not reproduced perfectly and the Kondo effect is of course especially dependent on the hybridization function at $\omega \approx 0$. The encouraging performance of the HMPS scheme and the good agreement between the results obtained from HMPS and from AMEA prompts us to use AMEA to study the system in its nonequilibrium steady state, for which HMPS cannot be used.

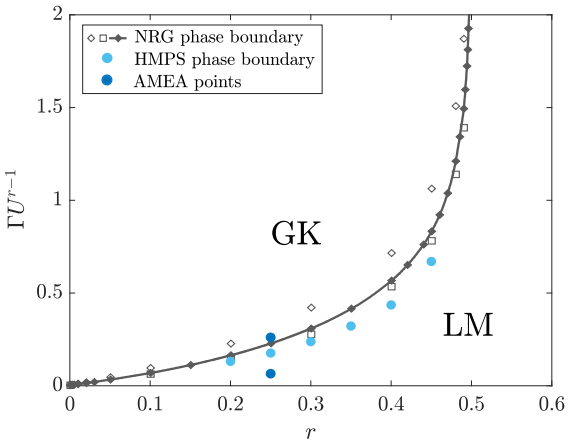

Figure 6.6: Phase diagram adapted from Ref. [166] (with kind permission) displaying different NRG results.[13] On top of this we present our HMPS results for the phase boundary obtained via the extrapolation scheme discussed in the text. We also indicate the two points we consider in AMEA, i.e. $r = 0.25$, $U = 6$ and $\Gamma = 0.25$ and $\Gamma = 1$. If U is much smaller than the bandwidth, the phase boundary for a given r is expected to depend on ΓU^{r-1} only [166].

6.4.2.2 Nonequilibrium steady state

We now present nonequilibrium steady state results obtained by applying a finite bias voltage. Since the calculations are more demanding than the conventional HMPS ones, we focus on two points in the (equilibrium) phase diagram Fig. 6.6, one in the GK and another in the LM phase, instead of doing a complete sweep of parameters. Specifically, we take $r = 0.25$, $T = 0.05$, $U = 6$, and $\Gamma = 0.25$ and 1, respectively.

We start by studying the behavior of the Kondo peak as a function of voltage. Therefore, we plot in Fig. 6.7(a) and (b) the spectral function and the imaginary part of the self energy. In the Kondo regime, we observe that upon increasing the bias voltage from $\phi = 0$ the equilibrium Kondo peak is

[12] Even though the phase diagram of Ref. [166] was obtained under the assumption $U \ll D$, where D is the bandwidth, while in this work we have $U \lesssim D$. For $U \ll D$, D is irrelevant as energy scale and the phase boundary is solely determined by Γ, U and r, see Ref. [166].

[13] Results obtained by the local moment approach were removed here, since they are not relevant to the present discussion.

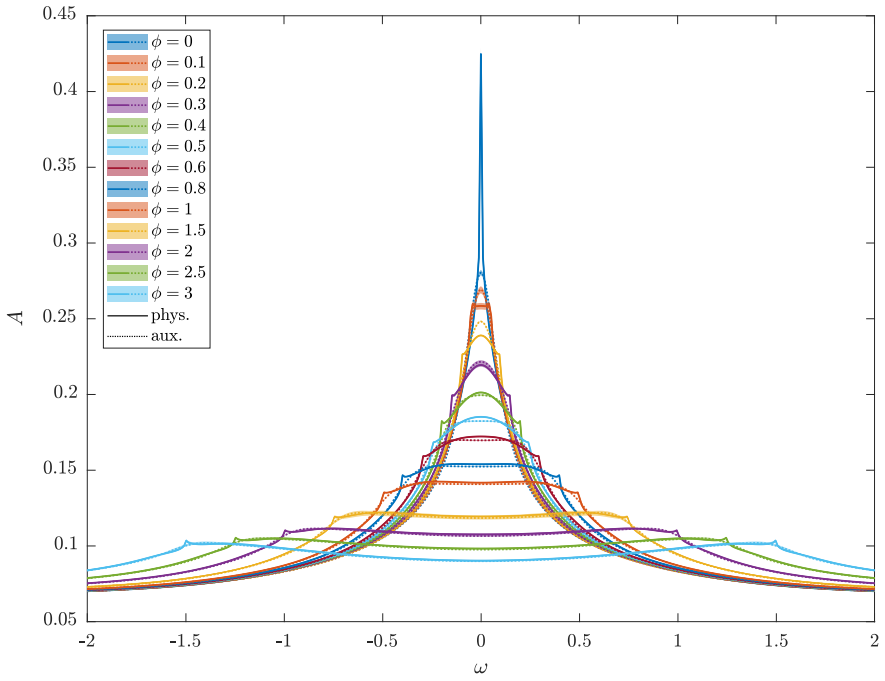

(a)

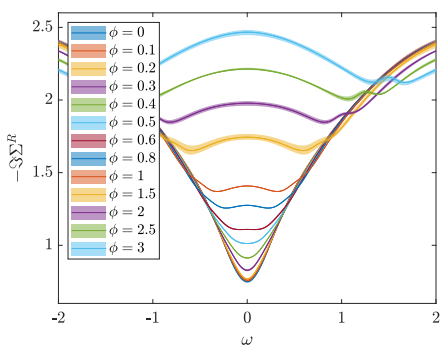

(b)

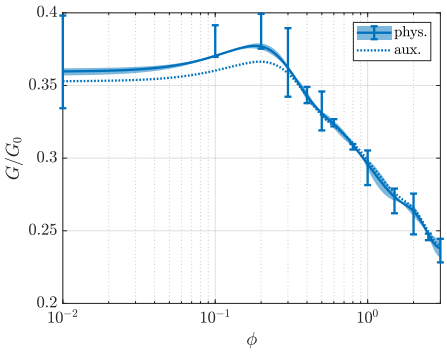

(c)

Figure 6.7: Nonequilibrium ($\phi > 0$) quantities in the Kondo regime, (a) spectral function, (b) retarded self energy, (c) differential conductance. The solid lines are the physical quantities and the dotted lines the auxiliary ones, see Sec. 6.3.3.4. Notice that the two curves are often indistinguishable. The error shadings and error bars are estimates based on symmetry considerations, see App. 6.8.

suppressed and broadened and, at some value of the voltage, it splits in two peaks. The split peaks then move apart together with the chemical potentials and they are further suppressed and broadened. Qualitatively, this is very similar to the situation observed for the nonequilibrium SIAM without a pseudogap [55–65]. In our data, the splitting becomes visible for $\phi \geq 0.8$ in the spectral function and, even before, for $\phi \geq 0.6$ in the self energy.

A measure for the accuracy of the mapping between Eq. (6.3.1) and the auxiliary open system, which is at the basis of the AMEA approach, can be read off from the deviations between the physical and the auxiliary spectral functions, defined in Sec. 6.3.3.4. In the limit in which the mapping to the auxiliary system becomes exact, i.e. for large N_B, these quantities become identical. Our data show that A_{aux} and A_{phys} differ only slightly for $\phi \geq 0.3$. Decreasing the voltage below $\phi = 0.3$ increases this deviation, especially for ω between the chemical potentials, and it is largest at $\phi = 0$, where the exact physical spectral function is expected to diverge at $\omega = 0$. Here we expect the accuracy of the AMEA mapping to be less reliable.

It is notable that as soon as the Kondo split peaks appear, they are very broad and poorly defined, even more in A_{phys}, but also in A_{aux}. They are first located at $|\omega|$ values slightly below $|\mu_\lambda| = \phi/2$, which they reach monotonically upon increasing the bias voltage. The physical spectral function displays additional features, namely two cusps at $\pm\phi/2$, not to be confused with the Kondo split peaks. We believe these to be artefacts originating from the difference between the auxiliary and the physical system and we expect them to disappear upon improving the accuracy.

Figs. 6.8(a) and (b) are obtained for the same parameters as Figs. 6.7(a) and (b), but a reduced hybridization strength of $\Gamma = 0.25$, instead of $\Gamma = 1$. According to the phase diagram in Fig. 6.6, the equilibrium system is in the LM phase, here. This is confirmed by our results which, indeed, do not show signatures of the Kondo effect anymore, neither in equilibrium nor at finite bias voltage.[14] Specifically, at nonzero ϕ, we observe dips in the spectral function located almost exactly at the values of the chemical potentials that

[14] Notice that it is not clear, whether a true phase transition or rather a crossover occurs between the two phases at finite voltage.

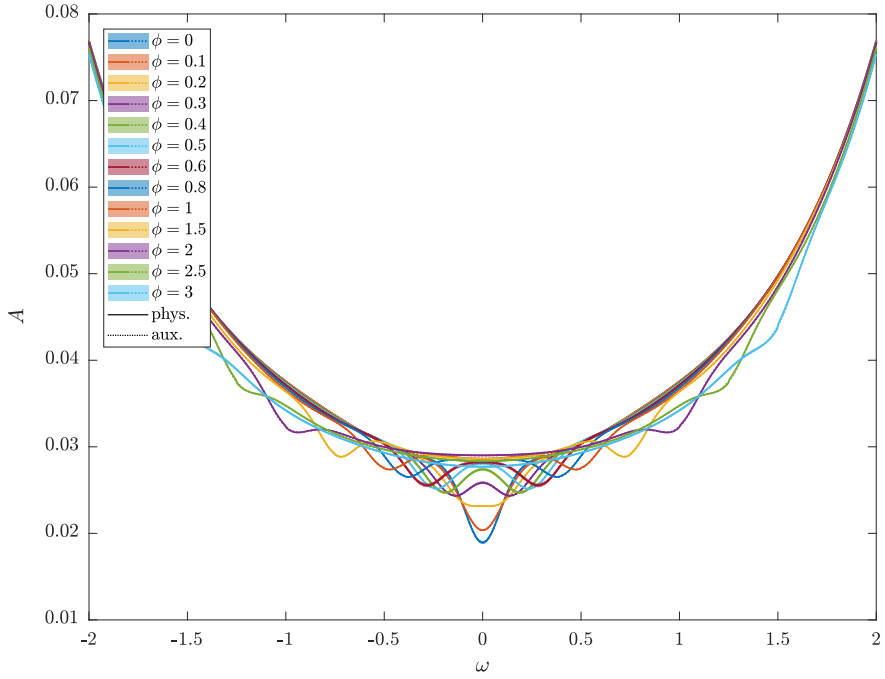

(a)

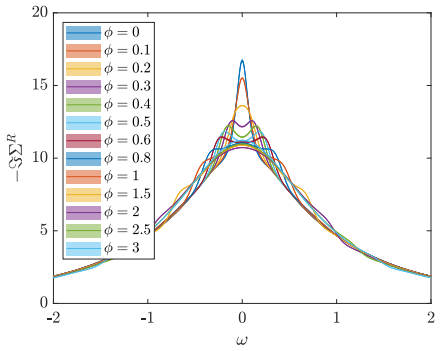

(b)

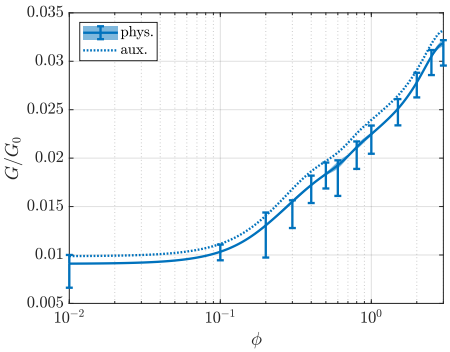

(c)

Figure 6.8: Nonequilibrium ($\phi > 0$) quantities in the LM regime. Conventions are as in Fig. 6.7.

appear to emerge as images of the dips in the leads' density of states. Also in this case, the physical and auxiliary spectral functions agree very well with each other, thus making us confident about the accuracy of our results.

Artificial cusps at $|\mu_\lambda|$ are also present in A_{phys}, but they are much smaller than the cusps in the Kondo regime.[15] These essentially lie within the error shadings of A_{aux} and are notable only upon zooming in.

Figs. 6.7(c) and 6.8(c) display the differential conductance G, obtained from Eqs. (6.3.14) and (6.3.15) as a function of the bias voltage at parameters corresponding to the Kondo and the LM regime. A notable difference with respect to the conventional SIAM is that in the Kondo regime, the maximum of $G(\phi)$ appears to be shifted to a finite voltage of $\phi \approx 0.2$. On the other hand, for $\phi \gtrsim 0.2$, $G(\phi)$ decreases logarithmically, as usual. The unusual structure of the differential conductance in the Kondo regime is probably, due to the fact that the position of the pseudogap is shifted along with the bias voltage. On the other hand, one should be aware of the fact that, due to the relatively large error bars,[16] it is not clear, whether the maximum at finite voltage is a genuine feature: strictly speaking, also a maximum at $\phi = 0$ would be consistent with the error bars. Furthermore, we already noticed in Fig. 6.7(a) that the deviations between A_{phys} and A_{aux} are large at $\phi \leq 0.2$ compared to the other bias voltages and this is exactly, where the peculiar behavior of $G(\phi)$ sets in. In contrast to the Kondo regime, Fig. 6.8(c) shows that in the LM regime the differential conductance increases with the bias voltage, as expected.[17]

[15] Here, a smaller truncated weight was chosen in the SVDs in the MPS time evolution, which could explain this improved accuracy.

[16] The error bars as well as the error shadings are estimated from the violation of PH symmetry of the corresponding quantities, as discussed in App. 6.8. Violation of PH symmetry via protocol 2 produces a slight difference between the left- and right-moving current $|j_L|$ and $|j_R|$, which is clearly unphysical for the steady state. Since $G(\phi)$ is obtained by numerical differentiation of the $j_\lambda(\phi)$ curves, its error is amplified. This explains, why the error bars in the $G(\phi)$ are so large.

[17] There seems to be a flat region up to $\phi \lesssim 0.1$ in $G(\phi)$. However, we do not believe this to have a particular physical meaning. This apparent behavior may be due to the fact that the numerical evaluation of G is quite challenging. G is obtained from finite current differences using three-point Lagrange polynomials to approximate the derivative and cubic splines to interpolate the result. However, we only have a coarse mesh of voltage points, with $\phi = 0.1$ being the first point at nonzero voltage (notice that only the points with errorbars correspond to data points). On the other hand, using a finer mesh does not make sense due to the limited accuracy of the fit. In addition, this apparently flat behavior is enhanced by the logarithmic scale of the ϕ axis. In a linear plot, the region $\phi \lesssim 0.1$ obviously looks much thinner and the curve displays a quadratic shape there.

We now attempt at extracting "effective" power-law exponents in the Kondo regime, as we do in equilibrium, by carrying out a fit of the nonequilibrium curves. More specifically, in analogy to Eqs. (6.4.1), (6.4.3) and (6.4.4), we fit the behavior

$$\Im\Delta^R(\omega) \propto |\omega-\mu_L|^r \ + |\omega-\mu_R|^r\,, \tag{6.4.5}$$

$$A(\omega) \propto |\omega-\mu_L|^{-s} + |\omega-\mu_R|^{-s}\,, \tag{6.4.6}$$

$$\Im\Sigma^R(\omega) \propto |\omega-\mu_L|^\kappa \ + |\omega-\mu_R|^\kappa\,. \tag{6.4.7}$$

The finite voltage and the imperfect pseudogap set a low-frequency cutoff to this behavior, which we expect not to hold down to zero frequency. The exponents, $r'(\phi)$, $s'(\phi)$ and $\kappa'(\phi)$, obtained by a fit on the interval $\Omega(\phi)$, defined in Eq. (6.4.2), are presented in Fig. 6.9. Since this interval shrinks upon increasing the bias voltage, we can faithfully perform the fit only for voltages $\phi \lesssim 0.6$, as discussed below Eq. (6.4.2). Thus, we can just catch the beginning of the interesting voltage region, where the Kondo split peaks start developing at $\phi \approx 0.6$, according to Fig. 6.7(a). Moreover, due to the lower cutoff in energy, the extracted exponents can only provide a rough semi-quantitative estimate. In the range $\phi \lesssim 0.6$ the exponents depend only slightly on the bias voltage. Nevertheless, it is notable that $r'(\phi)$ and $s'(\phi)$ are almost parallel. This may indicate that deviations in $\Im\Delta^R(\omega)$ (such as between $\Im\Delta^R_{\text{aux}}$ and $\Im\Delta^R_{\text{phys}}$) mainly translate into deviations in the spectral function, affecting $\Im\Sigma^R(\omega)$ in a minor way.[18] Indeed, if the self energy is more stable against numerical inaccuracies than the spectral function, one could try to exploit this to study the phase transition or crossover also out of equilibrium, with a scheme similar to the one presented in Sec. 6.4.2.1. However, in order to do this, it would be necessary to resolve a larger fraction of the interesting voltage region, $\phi \gtrsim 0.6$, which, on the other hand, would require a larger Ω interval, where the power-law in the auxiliary hybridization function is accurately resolved.

[18] This argument is supported by the fact that $\underline{\Delta}$ enters $\underline{G}_0$ and $\underline{G}$ in the same way in Dyson's equation. This is easily seen by comparing the general form of Eq. (6.3.13) to the result for zero self energy, $\underline{G} = \underline{G}_0$.

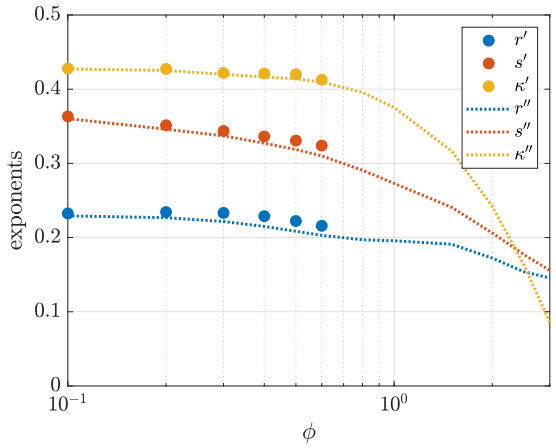

Figure 6.9: Nonequilibrium ($\phi > 0$) effective power-law exponents as a function of the bias voltage ϕ. The three pairs of exponents are extracted from a fit of the auxiliary retarded hybridization function (r', r''), the spectral function (s', s'') and the retarded self energy (κ', κ'') with Eqs. (6.4.5)-(6.4.7). The single and double primes correspond to different fitting intervals $\Omega(\phi)$ and $\Omega_1(\phi)$, see text.

Fig. 6.9 also displays the power-law exponents $r''(\phi)$, $s''(\phi)$ and $\kappa''(\phi)$ fitted on a larger interval $\Omega_1(\phi) = 0.2 + \frac{\phi}{2} < |\omega| < 1.2 + \frac{\phi}{2}$, which is obtained by a rigid shift of the equilibrium interval Ω by $\frac{\phi}{2}$. In the region $\phi \lesssim 0.6$, where both kinds of exponents ($\prime$ and $\prime\prime$) are defined, their values lie very close to each other. This confirms that the influence of the exponential factor in the hybridization function is negligible on these frequency and voltage intervals.

6.5 Summary and Conclusions

In this work we addressed the single-impurity Anderson model with leads displaying a power-law pseudogap in the density of states (PSG SIAM) by means of a nonperturbative approach to deal with nonequilibrium steady states, the auxiliary master equation approach (AMEA). We studied the generalized Kondo (GK) and the local moment (LM) phase of this model in equilibrium as well as their extension out of equilibrium.

In order to assess the validity of our approach, we first compared the re-

sults with the ones obtained with a direct MPS time evolution of the Hamiltonian (HMPS) [189]. HMPS is faster than AMEA and it can treat a larger number of bath sites in equilibrium, but, on the other hand, it cannot deal with a nonequilibrium steady state, due to the lack of a dissipation mechanism. We found that the spectral function, the self energy and the power-law exponents of these quantities agree very well between AMEA and HMPS, see Fig. 6.4. Furthermore, we implemented a scheme to find the phase boundary upon linear extrapolation of the power-law exponent of the self energy in the GK phase. The phase boundary obtained in this way agrees quite well with previous NRG results, see Fig. 6.6.

Out of equilibrium, we observe a splitting of the Kondo peak in the spectral function and in the self energy as a function of the bias voltage, see Figs. 6.7(a) and (b), as in the case of the conventional Kondo effect. On the other hand, the differential conductance appears to display a peculiar maximum at finite bias voltage, Fig. 6.7(c), which could be caused by the shift of the hybridization functions at finite bias voltages. Due to the error bars, it is not clear, whether this maximum can be considered a genuine feature of the model. We are not aware of any other work on this model displaying this feature. For example, in Ref. [187], the conductance maximum occurs at zero bias. However, this work also does not show a splitting of the Kondo resonance at finite bias voltages. The authors attributed this to the fact that the system is not in the limit of large interactions. A comparison with our results is difficult, since the position of the pseudogap as a function of voltage is considered differently in our paper. More specifically, while in Ref. [187] the pseudogap is fixed at $\omega = 0$, in our case it moves with the chemical potentials of the two leads, consistent with a rigid shift of the two leads.

Strictly speaking, what we observe in the Kondo regime, is the result of a superposition of the (pseudogap) GK effect with a small contribution from the ordinary one. This is, due to the fact that the imperfect mapping produces a nonzero residual $\Gamma_{\text{resid}} = -\Im\Delta^R_{\text{aux}}(0) \approx 0.39$, even at zero bias voltage. However, the contribution from this residual DOS is negligible, since the resulting Kondo temperature $T_{K,\text{resid}} \approx 0.0025$ is much smaller than the

temperature of our data $T \approx 20\,T_{K,\mathrm{resid}}$.[19] Therefore, the Kondo resonances shown in Fig. 6.7(a) and (b) are clearly dominated by the pseudogap GK effect.

It would be clearly desirable to be able to extend an accurate mapping of the hybridization function down to smaller $|\omega|$ values. This would further reduce the contribution of the ordinary Kondo effect and it would allow for a more accurate analysis of the low-frequency behavior. In previous works, Refs. [64, 83], we demonstrated that the accuracy of the mapping increases exponentially upon increasing the number of bath sites. However, this is only true, if we find good enough minima of the cost function measuring the difference between $\underline{\Delta}_{\mathrm{aux}}$ and $\underline{\Delta}_{\mathrm{phys}}$. This has, so far, turned out to be difficult for the PSG model studied here. In order to resolve the power-law with the cusp, bath sites on all energy scales would be required, as used in NRG. To make progress in this direction, we tried to fit the hybridization function on a logarithmic frequency grid and/or include its power-law exponent explicitly into the cost function, but without success so far. The fit seems to be quite unstable in all of these cases.

On the technical side, this work presents a development of the AMEA Lindblad many-body impurity problem within a matrix product states algorithm. Due to the reduced local Hilbert space obtained by separating the degrees of freedom, the present implementation is faster and more stable than the one of our previous work, Ref. [64]. On the other hand, the disadvantage of the structure used here is that additional long-range couplings between the impurity and the baths are introduced, as illustrated in Fig. 6.2, and the entanglement must be carried across the sites in between, which causes the bond dimension to increase. An obvious way to avoid this is a "fork" structure, in particular, a "double fork", which has three bonds at the impurity, instead of two. This structure naturally takes into account the spin separation as well as the separation between full and empty baths and, at the same time, only has nearest neighbor couplings. The disadvantage of this scheme

[19] T_K is estimated with the widely used formula from Ref. [31], $T_K = \sqrt{\Gamma U/2}\exp\left[-\pi U/(8\Gamma)\right]$, assuming a constant lead DOS with a hybridization strength of $\Gamma = \Gamma_{\mathrm{resid}}$.

is that it cannot be represented by MPS, because of the third bond, and it thus requires the implementation of a new tensor network, similar to the one described in Ref. [189]. Work along these lines is in progress.

6.6 Acknowledgments

We would like to thank Franz Scherr for providing a first implementation of the AMEA mapping using the python library tensorflow. This work was supported by the Austrian Science Fund (FWF) within the project P26508 and the START program Y746, as well as NaWi Graz. The numerical results presented here have been carried out on the D-Cluster Graz and on the VSC-3 HPC Cluster Vienna.

6.7 Construction of a nonequilibrium system from equilibrium bath parameters

Here, we show two results concerning the representation of a noninteracting fermionic bath in terms of Lindblad open systems, focussing on a geometry that is suitable for a treatment with MPS. As discussed in our previous work [64], for the sake of an MPS treatment, it is convenient to connect the impurity to a bath which is full and one which is empty. Each of the two baths should have a one-dimensional chain geometry and couple on each side of the impurity. This geometry guarantees a slower propagation of entanglement. For this reason, in App. 6.7.1 we show, how to represent an arbitrary hybridization function as originating from a full and an empty bath. This is valid both for a nonequilibrium as well as for an equilibrium $\phi = 0$ hybridization function. In our paper, it is convenient to start with such a representation for the fit of an equilibrium bath and then use this solution to produce a full-empty representation for a finite voltage $\phi \neq 0$. How this is done, is shown in App. 6.7.2.

6.7.1 Splitting into a full and empty bath

The effects of an arbitrary noninteracting fermionic bath on a single-site impurity are completely described by its hybridization function $\underline{\Delta}(\omega)$ in Keldysh space. Here, we show that any (equilibrium or nonequilibrium) $\underline{\Delta}$ can always be split as $\underline{\Delta} = \underline{\Delta}_F + \underline{\Delta}_E$, where $\underline{\Delta}_F$ describes a full (F) and $\underline{\Delta}_E$ an empty (E) (equilibrium) bath. As discussed above, these two baths are represented by a Lindblad equation, where $\mathbf{\Gamma}^{(1)} = 0$ or $\mathbf{\Gamma}^{(2)} = 0$, respectively.

For better readability, we omit the frequency argument ω and introduce the two components of the hybridization function

$$\Delta^{Ri} \equiv \Im \Delta^R \,, \qquad \Delta^{Ki} \equiv \frac{\Delta^K}{2i} \,. \tag{6.7.1}$$

In equilibrium, these two components are linked via the fluctuation-dissipation theorem,

$$\Delta^{Ki} = \Delta^{Ri}(1 - 2f(\omega - \mu)) \,, \tag{6.7.2}$$

where f is the Fermi function and μ the chemical potential. For a full/empty equilibrium bath the relation

$$\Delta^{Ki}_{F/E} = \mp \Delta^{Ri}_{F/E} \tag{6.7.3}$$

follows from Eq. (6.7.2) for $f \equiv 1$ (F) or 0 (E), respectively. We can, therefore, decompose

$$\begin{aligned} \Delta^{Ki} &= \Delta^{Ki}_F + \Delta^{Ki}_E = -\Delta^{Ri}_F + \Delta^{Ri}_E \,, \\ \Delta^{Ri} &= \Delta^{Ri}_F + \Delta^{Ri}_E \,, \end{aligned}$$

which gives

$$\Delta^{Ri}_{F/E} = \frac{\Delta^{Ri} \mp \Delta^{Ki}}{2} \,. \tag{6.7.4}$$

Note that Eqs. (6.7.2) and (6.7.3) are equilibrium properties. Therefore, these are valid for any component of each one of the two (uncoupled) baths, E and F, and in particular for the Green's function matrix. Moreover, a matrix inversion preserves these relations. However, for a matrix $\boldsymbol{A}^\beta$, $\beta \in \{R, K\}$,

such as the Green's function or self energy matrix, one has to replace the imaginary part (6.7.1) with the anti-Hermitian part, i.e.:

$$\begin{aligned} \boldsymbol{A}^{Ri} &= \frac{1}{2i}(\boldsymbol{A}^{R} - \boldsymbol{A}^{R\dagger}) \\ \boldsymbol{A}^{Ki} &= \frac{1}{4i}(\boldsymbol{A}^{K} - \boldsymbol{A}^{K\dagger}) \end{aligned} \tag{6.7.5}$$

Notice that the Keldysh component $\boldsymbol{A}^{K}$ is anti-Hermitian anyway. In this case (6.7.3) becomes

$$\boldsymbol{A}^{Ki}_{F/E} = \mp \boldsymbol{A}^{Ri}_{F/E}\,, \tag{6.7.6}$$

Applying Eq. (6.7.5) to the Green's function matrix of one of the two uncoupled baths (cf. Eqs. (40) and (41) in Ref. [63]),

$$\begin{aligned} \left(\underline{\boldsymbol{G}}^{-1}\right)^{R} &= \omega \boldsymbol{I} - \boldsymbol{E} + i\left(\boldsymbol{\Gamma}^{(1)} + \boldsymbol{\Gamma}^{(2)}\right)\,, \\ \left(\underline{\boldsymbol{G}}^{-1}\right)^{K} &= -2i\left(\boldsymbol{\Gamma}^{(2)} - \boldsymbol{\Gamma}^{(1)}\right)\,, \end{aligned}$$

results in

$$\begin{aligned} \left(\underline{\boldsymbol{G}}^{-1}\right)^{Ri} &= \boldsymbol{\Gamma}^{(1)} + \boldsymbol{\Gamma}^{(2)}\,, \\ \left(\underline{\boldsymbol{G}}^{-1}\right)^{Ki} &= \boldsymbol{\Gamma}^{(1)} - \boldsymbol{\Gamma}^{(2)}\,. \end{aligned} \tag{6.7.7}$$

Inserting this result further into Eq. (6.7.6) yields that a full bath has $\boldsymbol{\Gamma}^{(1)} = 0$ and an empty one $\boldsymbol{\Gamma}^{(2)} = 0$, as expected,

$$\left(\underline{\boldsymbol{G}}^{-1}\right)^{Ri}_{F} = \boldsymbol{\Gamma}^{(2)}\,, \quad \left(\underline{\boldsymbol{G}}^{-1}\right)^{Ri}_{E} = \boldsymbol{\Gamma}^{(1)}\,. \tag{6.7.8}$$

Notice that this splitting procedure does not change the properties of the impurity. Furthermore, it can be carried out also for an equilibrium bath or for a situation in which the leads are partially full or partially empty. A crucial point is that in MPS, it is always convenient to split the baths in this way, because the entanglement is less severe, see Ref. [64].

6.7.2 From equilibrium to nonequilibrium

As discussed, we start by fitting a bath in equilibrium and then we split it into a full and an empty one, see Fig. 6.10. In fact, it turns out that such a geometry naturally comes out for a chain geometry fit.

(a) (b)

Figure 6.10: (a) Impurity (red sphere) coupled to a partially filled bath (semicircle) at chemical potential μ. (b) The same hybridization function can be obtained by coupling the impurity to a full and empty bath with appropriate DOS.

For the situation depicted in Fig. 6.10(b) the fit produces the following Lindblad matrices, assuming PH symmetry,

$$\boldsymbol{E} = \left(\begin{array}{c|c|c} \tilde{\boldsymbol{E}}^{\tau} & \begin{matrix}0\\t\end{matrix} & 0 \\ \hline \begin{matrix}0 & t\end{matrix} & \varepsilon_f & \begin{matrix}t & 0\end{matrix} \\ \hline 0 & \begin{matrix}t\\0\end{matrix} & \tilde{\boldsymbol{E}} \end{array}\right) \tag{6.7.9}$$

and

$$\boldsymbol{\Gamma}^{(1)} = \left(\begin{array}{c|c|c} \tilde{\boldsymbol{\Gamma}}^{\tau} & 0 & 0 \\ \hline 0 & 0 & 0 \\ \hline 0 & 0 & 0 \end{array}\right), \quad \boldsymbol{\Gamma}^{(2)} = \left(\begin{array}{c|c|c} 0 & 0 & 0 \\ \hline 0 & 0 & 0 \\ \hline 0 & 0 & \tilde{\boldsymbol{\Gamma}} \end{array}\right).$$

Here, $\tilde{\boldsymbol{E}}$ and $\tilde{\boldsymbol{\Gamma}}$ are $N_B/2 \times N_B/2$ block matrices and each matrix $\boldsymbol{A}^{\tau}$ is $\boldsymbol{A}$ with the order of indices inverted and different signs, see Eq. (27) in Ref. [83], for the exact relations. For MPS, $\tilde{\boldsymbol{E}}$ and $\tilde{\boldsymbol{\Gamma}}$ should be tridiagonal, which corresponds to having nearest-neighbor hoppings and Γ terms only. The retarded hybridization function of, for instance, the full bath is then

given by

$$\Delta_F^R(\omega) = t^2 \bar{\gamma}^R(\omega) \tag{6.7.10}$$

with the boundary Green's function

$$\bar{\gamma}^R(\omega) = \left[\left(\omega \boldsymbol{I} - \tilde{\boldsymbol{E}} + i\tilde{\boldsymbol{\Gamma}} \right)^{-1} \right]_{11} \tag{6.7.11}$$

and the Keldysh hybridization function $\Delta_F^K(\omega)$ is fixed by Eq. (6.7.3). The result for the empty bath follows from PH symmetry.

Instead of the equilibrium situation in Fig. 6.10(a), we would now like to represent a nonequilibrium one, as depicted in Fig. 6.11(a).

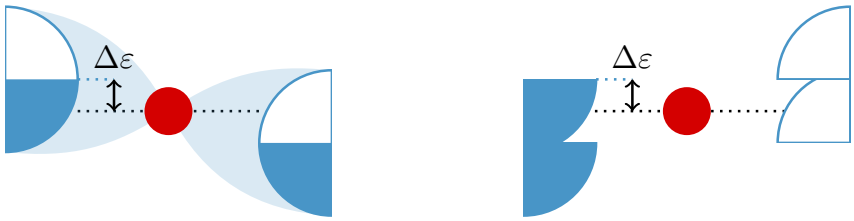

(a) (b)

Figure 6.11: (a) Impurity (red sphere) coupled to a partially filled left bath and a partially filled right bath (semicircles), whose chemical potentials differ by $2\Delta\varepsilon$. (b) The same situation with two full (blue) and two empty (white) baths.

If the total DOS is fixed, this is obtained by reducing the hoppings to the impurity by $1/\sqrt{2}$ and by doubling the number of bath sites and shifting their on-site energies by $\pm\Delta\varepsilon$. Then Fig. 6.10(b) schematically becomes Fig. 6.11(b), which can no longer be represented in a chain geometry (with

tridiagonal matrices). The matrix in Eq. (6.7.9) becomes

$$\boldsymbol{E}' = \left(\begin{array}{c|c|c|c|c} \tilde{\boldsymbol{E}}^{\tau} + \Delta\varepsilon \boldsymbol{I} & 0 & \begin{matrix}0\\ t'\end{matrix} & 0 & 0 \\ \hline 0 & \tilde{\boldsymbol{E}}^{\tau} - \Delta\varepsilon \boldsymbol{I} & \begin{matrix}0\\ t'\end{matrix} & 0 & 0 \\ \hline 0 \quad t' & 0 \quad t' & \varepsilon_f & t' \quad 0 & t' \quad 0 \\ \hline 0 & 0 & \begin{matrix}t'\\ 0\end{matrix} & \tilde{\boldsymbol{E}} - \Delta\varepsilon \boldsymbol{I} & 0 \\ \hline 0 & 0 & \begin{matrix}t'\\ 0\end{matrix} & 0 & \tilde{\boldsymbol{E}} + \Delta\varepsilon \boldsymbol{I} \end{array}\right) \tag{6.7.12}$$

with $t' = t/\sqrt{2}$ and, correspondingly, $\boldsymbol{\Gamma}^{(1)}$ and $\boldsymbol{\Gamma}^{(2)}$. In this situation, Eq. (6.7.10) still holds, but instead of Eq. (6.7.11), we have

$$\Delta_F^R(\omega) = \frac{t^2}{2}\left(\bar{\gamma}^R(\omega + \Delta\varepsilon) + \bar{\gamma}^R(\omega - \Delta\varepsilon)\right) .$$

However, the matrix (6.7.12) is not suitable for MPS, as it is not tridiagonal. To make progress, we observe that $\Delta_F^R(\omega)$ can be obtained by considering the following matrix in block form

$$\boldsymbol{h}' = \left(\begin{array}{c|c|c} 0 & t' \quad 0 & t' \quad 0 \\ \hline \begin{matrix}t'\\ 0\end{matrix} & \tilde{\boldsymbol{E}} - i\tilde{\boldsymbol{\Gamma}} - \Delta\varepsilon \boldsymbol{I} & 0 \\ \hline \begin{matrix}t'\\ 0\end{matrix} & 0 & \tilde{\boldsymbol{E}} - i\tilde{\boldsymbol{\Gamma}} + \Delta\varepsilon \boldsymbol{I} \end{array}\right)$$

and employing Dyson's equation,

$$\Delta_F^R(\omega) = \omega - \frac{1}{[(\omega \boldsymbol{I} - \boldsymbol{h}')^{-1}]_{11}} . \tag{6.7.13}$$

For MPS we need a tridiagonal form, as discussed above. This can be achieved with a Bi-Lanczos transformation. All we need is that $[(\omega \boldsymbol{I} - \boldsymbol{h}')^{-1}]_{11}$

remains invariant. The transformation is produced by a matrix (here the upper block is 1×1 and the lower is $N_B \times N_B$)

$$\boldsymbol{U} = \left(\begin{array}{c|c} 1 & 0 \\ \hline 0 & \tilde{\boldsymbol{U}} \end{array}\right) , \tag{6.7.14}$$

where U is, in general, non-unitary, yielding

$$\begin{aligned} \boldsymbol{h}'' &= \boldsymbol{U}^{-1}\boldsymbol{h}'\boldsymbol{U} \\ &= \left(\begin{array}{c|cc} 0 & t'' & 0 \\ \hline t'' & & \\ 0 & & \boldsymbol{H}'' \end{array}\right) . \end{aligned}$$

Here, the non-Hermitian tridiagonal matrix $\boldsymbol{H}''$ identifies the new parameters of the full (F) bath,

$$\begin{aligned} \tilde{\boldsymbol{E}}'' &\equiv \frac{\boldsymbol{H}''^{\dagger} + \boldsymbol{H}''}{2} , \\ \tilde{\boldsymbol{\Gamma}}'' &\equiv \frac{\boldsymbol{H}''^{\dagger} - \boldsymbol{H}''}{2i} , \end{aligned} \tag{6.7.15}$$

while the ones of the empty (E) bath are obtained by PH symmetry, see Eq. (27) in Ref. [83].

Note that, since $\tilde{\boldsymbol{U}}$ is not unitary, $\tilde{\boldsymbol{E}}''$ and $\tilde{\boldsymbol{\Gamma}}''$ are not simply obtained by transforming $\tilde{\boldsymbol{E}}$ and $\tilde{\boldsymbol{\Gamma}}$, separately. This can, and in our case does, produce $\tilde{\boldsymbol{\Gamma}}''$ that are not semi-positive definite, as should be required for the Lindblad equation. Still, the steady state we obtain is stable and the spectral functions turn out to be causal. The reason is that the new parameters originate from semi-positive definite matrices.

6.8 Symmetry considerations and error estimation

In principle, we can calculate four Green's functions individually, G^{α}_{σ} with $\sigma \in \{\uparrow, \downarrow\}$ and $\alpha \in \{<, >\}$. The system, though, is PH symmetric, which relates the lesser and the greater Green's function to each other, and it is spin symmetric. Therefore, the following relations must be fulfilled,

$$G^{<}_{\sigma}(x) = -G^{>}_{\sigma}(-x)\,, \tag{6.8.1}$$

$$G^{\alpha}_{\uparrow}(x) = G^{\alpha}_{\downarrow}(x)\,, \tag{6.8.2}$$

for x being either t or ω. This reduces the number of actually independent Green's functions to only one. Thus, in order to obtain the spectral function, for example, it is in principle sufficient to calculate only one G^{α}_{σ}, then construct $G^{\bar{\alpha}}_{\sigma}$ with $\bar{\alpha} \neq \alpha$ from Eq. (6.8.1) and evaluate Eq. (6.3.11). We refer to this as **protocol 1**.

However, if we calculate G^{α}_{σ} with AMEA employing MPS, the symmetry relations, Eqs. (6.8.1)-(6.8.2), are not exactly fulfilled. This is, due to the approximations within the MPS calculation, more specifically, due to the truncation and Suzuki-Trotter errors. Fig. 6.12 shows the consequences of these violations at the example of the spectral function.

We can see that the spectral functions determined from only one G^{α}_{σ}, according to protocol 1, are symmetric by construction, $A^{\alpha}_{\sigma}(\omega) = A^{\alpha}_{\sigma}(-\omega)$, but they differ from each other, $A^{\alpha}_{\sigma}(\omega) \neq A^{\bar{\alpha}}_{\bar{\sigma}}(\omega)$ for $\alpha \neq \bar{\alpha}$ and $\sigma \neq \bar{\sigma}$. The area enclosed by the four different solutions is color-shaded and the solid curve in the center is the average of these solutions, which we call symmetrized spectral function in this paper. The deviations of the borders of the shaded area from the symmetrized spectral function can be used as a measure for the symmetry errors throughout the MPS calculation.

In this figure, we can also see the spectral functions naively determined from two Green's functions, $G^{<}_{\sigma}$ and $G^{>}_{\sigma}$, by evaluating Eq. (6.3.11) directly, without enforcing PH symmetry. We refer to this as **protocol 2**. These

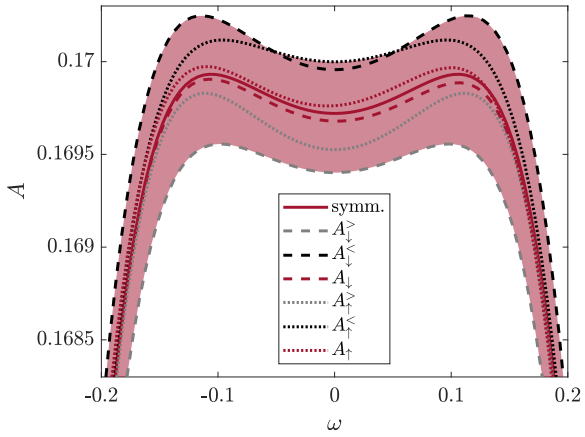

Figure 6.12: Auxiliary spectral functions $A(\omega)$ obtained from different raw data for symmetry considerations and error estimation, see text.

spectral functions are not exactly symmetric, $A_\sigma(\omega) \neq A_\sigma(-\omega)$, as discussed above, but they are close to the symmetrized spectral function and they lie almost entirely within the shaded area for almost all bias voltages (except $\phi = 0.8$ and $\phi = 1$).

Throughout this paper, we display also other, in principle symmetric, quantities as symmetrized curves with errors in the form of color-shaded areas, obtained by protocol 1. Specifically, the self energy and the differential conductance are represented in this way, see Figs. 6.4, 6.7 and 6.8. For the differential conductance, we also consider deviations arising by protocol 2 and plot the corresponding errors separately, as bars, in addition to the shaded area, see Figs. 6.7(c) and 6.8(c). For the other quantities these errors lie almost entirely within the shaded area, anyway, and their inclusion does not make any difference. The differential conductance, though, being obtained as a numerical derivative of these quantities by Eqs. (6.3.14) and (6.3.15), is more sensitive to deviations.

Chapter 7

Conclusions and Outlook

In this thesis, we studied the Anderson impurity model in different nonequilibrium situations generated by the application of a bias voltage. In particular, we considered an additional local magnetic field at the impurity, Ch. 5, and leads displaying a pseudogap in the density of states, Ch. 6. We focused on the interplay of these features with the bias voltage and studied the combined effect on the spectral and transport properties in the steady state of the system. For a detailed conclusion about these specific problem sets, we refer the reader to Secs. 5.5 and 6.5, respectively.

We employed the auxiliary master equation approach in combination with two different schemes based on matrix product states for our studies. Dealing with a genuine open quantum system, we are able to follow the time evolution up to the steady state and compute Green's functions in the steady state. Our approach is not limited to a certain regime of the model, specifically, we can also access the challenging intermediate regime, where $e\phi \approx k_B T_K$ (and $|g|\mu_B B \approx k_B T_K$). We are able to generate very accurate results, see Fig. 5.6, and the accuracy can, in principle, be further increased in a controlled way by increasing the number of bath sites [83].

We found that the novel matrix product states scheme introduced in Ch. 6 is preferable to the one adapted in Ch. 5. The separation of spins clearly reduces the bond dimension, at best to its square root at zero interaction, but also at large interaction, we found that the more complex new scheme is worth

the effort. Both algorithms, the time-dependent density-matrix renormalization group as well as the time-evolving block decimation algorithm worked well for our purposes. Due to the restricted geometry in both schemes, i.e. nearest neighbor couplings only, a comparatively large number of bath sites is required for the mapping to the auxiliary Lindblad system to be accurate, which slows down the many-body solution. This problem might be overcome by employing the time-dependent variational principle [100, 101], instead, which can deal with longer-ranged couplings, as well.

Thinking of future perspectives, the next step could be to tackle the time dependency of the Anderson impurity model after a local quench or the influence of periodic driving. This can be achieved with minor modifications to the present code. Also interesting to study are setups with multiple impurities potentially coupled to multiple baths leading to the emergence of exotic variants of the Kondo effect. This requires a little more effort in the implementation, depending on the complexity of the many-body system under investigation. Examples include the integer-spin Kondo effect in a quantum dot with singlet-triplet degeneracy [191], the ferromagnetic Kondo effect in a triple quantum dot [192] and the two-channel charge Kondo effect [193].

Bibliography

[1] D. M. Fugger, A. Dorda, F. Schwarz, J. von Delft, and E. Arrigoni. Nonequilibrium Kondo effect in a magnetic field: auxiliary master equation approach. *New J. Phys.* 20, 013030 (2018) (see pp. 4, 5, 20, 21, 28, 37, 58, 60, 63, 85, 87, 89, 97).

[2] M. E. Sorantin, D. M. Fugger, A. Dorda, W. von der Linden, and E. Arrigoni. Auxiliary master equation approach within stochastic wave functions: Application to the interacting resonant level model. *Phys. Rev. E* 99, 043303 (2019) (see pp. 30, 60, 96).

[3] D. M. Fugger, D. Bauernfeind, M. E. Sorantin, and E. Arrigoni. Nonequilibrium pseudogap Anderson impurity model: A master equation tensor network approach. *Phys. Rev. B* 101, 165132 (2020) (see pp. 4, 5, 20, 21, 28, 37, 55, 56, 61, 85, 86).

[4] P. W. Anderson. More Is Different. *Science* 177, 393 (1972) (see p. 3).

[5] J. Bardeen, L. N. Cooper, and J. R. Schrieffer. Microscopic Theory of Superconductivity. *Phys. Rev.* 106, 162 (1957) (see p. 3).

[6] M. R. Norman. The Challenge of Unconventional Superconductivity. *Science* 332, 196 (2011) (see p. 3).

[7] H. Tasaki. Ferromagnetism in Hubbard Models. *Phys. Rev. Lett.* 75, 4678 (1995) (see p. 3).

[8] S. Sachdev and B. Keimer. Quantum criticality. *Phys. Today* 64, 29 (2011) (see p. 3).

[9] N. F. Mott. The Basis of the Electron Theory of Metals, with Special Reference to the Transition Metals. *Proc. Phys. Soc. A* 62, 416 (1949) (see p. 3).

[10] S. Wirth and F. Steglich. Exploring heavy fermions from macroscopic to microscopic length scales. *Nat. Rev. Mater.* 1, 16051 (2016) (see p. 3).

[11] J. Kondo. Resistance Minimum in Dilute Magnetic Alloys. *Prog. Theor. Phys.* 32, 37 (1964) (see pp. 3, 7).

[12] E. Assmann, P. Blaha, R. Laskowski, K. Held, S. Okamoto, and G. Sangiovanni. Oxide Heterostructures for Efficient Solar Cells. *Phys. Rev. Lett.* 110, 078701 (2013) (see p. 3).

[13] E. R. Flynn and H. C. Bryant. A biomagnetic system for *in vivo* cancer imaging. *Phys. Med. Biol.* 50, 1273 (2005) (see p. 3).

[14] J. M. Elzerman, R. Hanson, L. H. W. van Beveren, L. M. K. Vandersypen, and L. P. Kouwenhoven. In: *Quantum Computing in Solid State Systems* (eds B. Ruggiero, P. Delsing, C. Granata, Y. Pashkin, and P. Silvestrini) (Springer, New York, 2006) (see p. 3).

[15] G. Schmid. *Nanoparticles: From Theory to Application* (Wiley, 2011) (see p. 3).

[16] D. A. Ryndyk. *Theory of Quantum Transport at Nanoscale* (Springer, 2016) (see p. 3).

[17] P. S. Peercy. The drive to miniaturization. *Nature* 406, 1023 (2000) (see p. 3).

[18] L. Brus. Commentary: Carbon Nanotubes, CdSe Nanocrystals, and Electron-Electron Interaction. *Nano Lett.* 10, 363 (2010) (see p. 3).

[19] J. Hubbard. Electron correlations in narrow energy bands. *Proc. R. Soc. A.* 276, 238 (1963) (see p. 3).

[20] P. W. Anderson. Localized Magnetic States in Metals. *Phys. Rev.* 124, 41 (1961) (see pp. 4, 7).

[21] S. G. Brush. History of the Lenz-Ising Model. *Rev. Mod. Phys.* 39, 883 (1967) (see p. 4).

[22] E. Arrigoni, M. Knap, and W. von der Linden. Nonequilibrium Dynamical Mean-Field Theory: An Auxiliary Quantum Master Equation Approach. *Phys. Rev. Lett.* 110, 086403 (2013) (see pp. 4, 70, 82, 83, 89).

[23] C. Giannetti, M. Capone, D. Fausti, M. Fabrizio, F. Parmigiani, and D. Mihailovic. Ultrafast optical spectroscopy of strongly correlated materials and high-temperature superconductors: a non-equilibrium approach. *Adv. Phys.* 65, 58 (2016) (see p. 4).

[24] A. Lazarides, A. Das, and R. Moessner. Fate of Many-Body Localization Under Periodic Driving. *Phys. Rev. Lett.* 115, 030402 (2015) (see p. 4).

[25] M. E. Sorantin, A. Dorda, K. Held, and E. Arrigoni. Impact ionization processes in the steady state of a driven Mott-insulating layer coupled to metallic leads. *Phys. Rev. B* 97, 115113 (2018) (see pp. 4, 11, 83).

[26] A. Mitra, S. Takei, Y. B. Kim, and A. J. Millis. Nonequilibrium Quantum Criticality in Open Electronic Systems. *Phys. Rev. Lett.* 97, 236808 (2006) (see pp. 4, 88).

[27] T. Pellizzari, S. A. Gardiner, J. I. Cirac, and P. Zoller. Decoherence, Continuous Observation, and Quantum Computing: A Cavity QED Model. *Phys. Rev. Lett.* 75, 3788 (1995) (see p. 4).

[28] M. Eckstein, M. Kollar, and P. Werner. Thermalization after an Interaction Quench in the Hubbard Model. *Phys. Rev. Lett.* 103, 056403 (2009) (see p. 4).

[29] A. Polkovnikov, K. Sengupta, A. Silva, and M. Vengalattore. Colloquium: Nonequilibrium dynamics of closed interacting quantum systems. *Rev. Mod. Phys.* 83, 863 (2011) (see p. 4).

[30] F. Schwarz, I. Weymann, J. von Delft, and A. Weichselbaum. Nonequilibrium Steady-State Transport in Quantum Impurity Models: A Thermofield and Quantum Quench Approach Using Matrix Product States. *Phys. Rev. Lett.* 121, 137702 (2018) (see pp. 4, 65, 71, 81–83).

[31] A. C. Hewson. *The Kondo Problem to Heavy Fermions* (Cambridge University Press, Cambridge, 1993) (see pp. 5, 87, 119).

[32] P. Coleman. *Introduction to Many-Body Physics* (Cambridge University Press, Cambridge, 2015) (see pp. 5, 13, 18).

[33] L. Kouwenhoven and L. Glazman. Revival of the Kondo effect. *Phys. World* 14, 33 (2001) (see pp. 5, 8, 10, 17).

[34] W. J. de Haas, J. de Boer, and G. J. van dën Berg. The electrical resistance of gold, copper and lead at low temperatures. *Physica* 1, 1115 (1934) (see pp. 7, 87).

[35] A. M. Clogston, B. T. Matthias, M. Peter, H. J. Williams, E. Corenzwit, and R. C. Sherwood. Local Magnetic Moment Associated with an Iron Atom Dissolved in Various Transition Metal Alloys. *Phys. Rev.* 125, 541 (1962) (see p. 7).

[36] M. P. Sarachik, E. Corenzwit, and L. D. Longinotti. Resistivity of Mo-Nb and Mo-Re Alloys Containing 1% Fe. *Phys. Rev.* 135, A1041 (1964) (see pp. 7, 87).

[37] A. Blandin and J. Friedel. Propriétés magnétiques des alliages dilués. Interactions magnétiques et antiferromagnétisme dans les alliages du type métal noble-métal de transition. *J. Phys. Radium* 20, 160 (1959) (see p. 7).

[38] C. Zener. Interaction Between the d Shells in the Transition Metals. *Phys. Rev.* 81, 440 (1951) (see p. 7).

[39] T. Kasuya. A Theory of Metallic Ferro- and Antiferromagnetism on Zener's Model. *Prog. Theor. Phys.* 16, 45 (1956) (see p. 7).

[40] K. G. Wilson. The renormalization group: Critical phenomena and the Kondo problem. *Rev. Mod. Phys.* 47, 773 (1975) (see p. 9).

[41] J. R. Schrieffer and P. A. Wolff. Relation between the Anderson and Kondo Hamiltonians. *Phys. Rev.* 149, 491 (1966) (see p. 9).

[42] P. Nozières. A "fermi-liquid" description of the Kondo problem at low temperatures. *J. Low Temp. Phys.* 17, 31 (1974) (see p. 9).

[43] K. Yamada. Perturbation Expansion for the Anderson Hamiltonian. II. *Prog. Theor. Phys.* 53, 970 (1975) (see p. 9).

[44] K. Yosida and K. Yamada. Perturbation Expansion for the Anderson Hamiltonian. III. *Prog. Theor. Phys.* 53, 1286 (1975) (see p. 9).

[45] P. B. Wiegmann. Exact solution of the s-d exchange model (Kondo problem). *J. Phys. C* 14, 1463 (1981) (see p. 9).

[46] N. Andrei. Diagonalization of the Kondo Hamiltonian. *Phys. Rev. Lett.* 45, 379 (1980) (see p. 9).

[47] J. W. Allen, S. J. Oh, M. B. Maple, and M. S. Torikachvili. Large Fermi-level resonance in the electron-addition spectrum of $CeRu_2$ and $CeIr_2$. *Phys. Rev. B* 28, 5347 (1983) (see p. 9).

[48] J. W. Allen, S. J. Oh, O. Gunnarsson, K. Schönhammer, M. B. Maple, M. S. Torikachvili, and I. Lindau. Electronic structure of cerium and light rare-earth intermetallics. *Adv. Phys.* 35, 275 (1986) (see p. 9).

[49] B. Horvatić, D. Šokčević, and V. Zlatić. Finite-temperature spectral density for the Anderson model. *Phys. Rev. B* 36, 675 (1987) (see p. 9).

[50] R. N. Silver, J. E. Gubernatis, D. S. Sivia, and M. Jarrell. Spectral densities of the symmetric Anderson model. *Phys. Rev. Lett.* 65, 496 (1990) (see p. 9).

[51] T. A. Costi, P. Schmitteckert, J. Kroha, and P. Wölfle. Numerical Renormalization Group Study of Pseudo-Fermion and Slave-Boson Spectral Functions in the Single Impurity Anderson Model. *Phys. Rev. Lett.* 73, 1275 (1994) (see p. 9).

[52] A. A. Abrikosov. Electron scattering on magnetic impurities in metals and anomalous resistivity effects. *Physics* 2, 5 (1965) (see p. 10).

[53] H. Suhl. Formation of Local Magnetic Moments in Metals. *Phys. Rev. Lett.* 19, 442 (1967) (see p. 10).

[54] Y. Meir, N. S. Wingreen, and P. A. Lee. Low-temperature transport through a quantum dot: The Anderson model out of equilibrium. *Phys. Rev. Lett.* 70, 2601 (1993) (see pp. 10, 18, 20, 64, 73, 76).

[55] N. S. Wingreen and Y. Meir. Anderson model out of equilibrium: Noncrossing-approximation approach to transport through a quantum dot. *Phys. Rev. B* 49, 11040 (1994) (see pp. 10, 73, 113).

[56] E. Lebanon and A. Schiller. Measuring the out-of-equilibrium splitting of the Kondo resonance. *Phys. Rev. B* 65, 035308 (2001) (see pp. 10, 73, 113).

[57] A. Rosch, J. Kroha, and P. Wölfle. Kondo Effect in Quantum Dots at High Voltage: Universality and Scaling. *Phys. Rev. Lett.* 87, 156802 (2001) (see pp. 10, 73, 113).

[58] T. Fujii and K. Ueda. Perturbative approach to the nonequilibrium Kondo effect in a quantum dot. *Phys. Rev. B* 68, 155310 (2003) (see pp. 10, 73, 113).

[59] J. E. Han and R. J. Heary. Imaginary-Time Formulation of Steady-State Nonequilibrium: Application to Strongly Correlated Transport. *Phys. Rev. Lett.* 99, 236808 (2007) (see pp. 10, 73, 113).

[60] F. B. Anders. Steady-State Currents through Nanodevices: A Scattering-States Numerical Renormalization-Group Approach to Open Quantum Systems. *Phys. Rev. Lett.* 101, 066804 (2008) (see pp. 10, 64, 73, 76, 113).

[61] M. Nuss, C. Heil, M. Ganahl, M. Knap, H. G. Evertz, E. Arrigoni, and W. von der Linden. Steady-state spectra, current and stability diagram of a quantum dot: A nonequilibrium variational cluster approach. *Phys. Rev. B* 86, 245119 (2012) (see pp. 10, 73, 113).

[62] G. Cohen, E. Gull, D. R. Reichman, and A. J. Millis. Green's Functions from Real-Time Bold-Line Monte Carlo Calculations: Spectral Properties of the Nonequilibrium Anderson Impurity Model. *Phys. Rev. Lett.* 112, 146802 (2014) (see pp. 10, 73, 113).

[63] A. Dorda, M. Nuss, W. von der Linden, and E. Arrigoni. Auxiliary master equation approach to nonequilibrium correlated impurities. *Phys. Rev. B* 89, 165105 (2014) (see pp. 10, 19, 21, 30, 70, 73, 82, 89, 94–96, 113, 122).

[64] A. Dorda, M. Ganahl, H. G. Evertz, W. von der Linden, and E. Arrigoni. Auxiliary master equation approach within matrix product states: Spectral properties of the nonequilibrium Anderson impurity model. *Phys. Rev. B* 92, 125145 (2015) (see pp. 10, 30, 49, 60, 65, 70, 72, 73, 82, 83, 96, 97, 99, 113, 119, 120, 122).

[65] A. Dorda, M. Ganahl, S. Andergassen, W. von der Linden, and E. Arrigoni. Thermoelectric response of a correlated impurity in the nonequilibrium Kondo regime. *Phys. Rev. B* 94, 245125 (2016) (see pp. 10, 73, 113).

[66] H. C. Manoharan, C. P. Lutz, and D. M. Eigler. Quantum mirages formed by coherent projection of electronic structure. *Nature* 403, 512 (2000) (see p. 10).

[67] D. Goldhaber-Gordon, H. Shtrikman, D. Mahalu, D. Abusch-Magder, U. Meirav, and M. A. Kastner. Kondo effect in a single-electron transistor. *Nature* 391, 156 (1998) (see pp. 10, 64, 76).

[68] L. Kouwenhoven and C. Marcus. Quantum dots. *Phys. World* 11, 35 (1998) (see p. 10).

[69] G. D. Scott and D. Natelson. Kondo Resonances in Molecular Devices. *ACS Nano* 4, 3560 (2010) (see p. 10).

[70] I. V. Borzenets, J. Shim, J. C. H. Chen, A. Ludwig, A. D. Wieck, S. Tarucha, H.-S. Sim, and M. Yamamoto. Observation of the Kondo screening cloud. *Nature* 579, 210 (2020) (see p. 10).

[71] A. Georges, G. Kotliar, W. Krauth, and M. J. Rozenberg. Dynamical mean-field theory of strongly correlated fermion systems and the limit of infinite dimensions. *Rev. Mod. Phys.* 68, 13 (1996) (see pp. 11, 87).

[72] G. Kotliar, S. Y. Savrasov, K. Haule, V. S. Oudovenko, O. Parcollet, and C. A. Marianetti. Electronic structure calculations with dynamical mean-field theory. *Rev. Mod. Phys.* 78, 865 (2006) (see p. 11).

[73] I. Titvinidze, A. Dorda, W. von der Linden, and E. Arrigoni. Transport through a correlated interface: Auxiliary master equation approach. *Phys. Rev. B* 92, 245125 (2015) (see pp. 11, 83).

[74] A. Dorda, I. Titvinidze, and E. Arrigoni. Quasiparticle excitations in steady state transport across a correlated layer. *J. Phy. Conf. Ser.* 696, 012003 (2016) (see pp. 11, 83).

[75] I. Titvinidze, A. Dorda, W. von der Linden, and E. Arrigoni. Resonance effects in correlated multilayer heterostructures. *Phys. Rev. B* 94, 245142 (2016) (see pp. 11, 83).

[76] I. Titvinidze, A. Dorda, W. von der Linden, and E. Arrigoni. Thermoelectric properties of a strongly correlated layer. *Phys. Rev. B* 96, 115104 (2017) (see pp. 11, 83).

[77] I. Titvinidze, M. E. Sorantin, A. Dorda, W. von der Linden, and E. Arrigoni. Charge redistribution in correlated heterostuctures within nonequilibrium real-space dynamical mean-field theory. *Phys. Rev. B* 98, 035146 (2018) (see p. 11).

[78] T. A. Costi and V. Zlatić. Charge Kondo Anomalies in PbTe Doped with Tl Impurities. *Phys. Rev. Lett.* 108, 036402 (2012) (see p. 14).

[79] D. C. Langreth. Friedel Sum Rule for Anderson's Model of Localized Impurity States. *Phys. Rev.* 150, 516 (1966) (see p. 16).

[80] C. A. Balseiro, G. Usaj, and M. J. Sanchez. Out of equilibrium transport through an Anderson impurity: probing scaling laws within the equation of motion approach. *J. Phys. Condens. Mat.* 22, 425602 (2010) (see pp. 20, 64, 73, 76).

[81] D. Withoff and E. Fradkin. Phase transitions in gapless Fermi systems with magnetic impurities. *Phys. Rev. Lett.* 64, 1835 (1990) (see pp. 20, 88, 106).

[82] L. Fritz and M. Vojta. Phase transitions in the pseudogap Anderson and Kondo models: Critical dimensions, renormalization group, and local-moment criticality. *Phys. Rev. B* 70, 214427 (2004) (see pp. 20, 88, 106, 110).

[83] A. Dorda, M. Sorantin, W. von der Linden, and E. Arrigoni. Optimized auxiliary representation of non-Markovian impurity problems by a Lindblad equation. *New J. Phys.* 19, 063005 (2017) (see pp. 21, 30, 70, 82, 89, 94, 96, 119, 123, 126, 129).

[84] G. Schaller. *Open Quantum Systems Far from Equilibrium* (Springer, Heidelberg, 2014) (see p. 21).

[85] H.-P. Breuer and F. Petruccione. *The Theory of Open Quantum Systems* (Oxford University Press, Oxford, 2002) (see pp. 21, 24).

[86] A. A. Dzhioev and D. S. Kosov. Super-fermion representation of quantum kinetic equations for the electron transport problem. *J. Chem. Phys.* 134, 044121 (2011) (see pp. 21, 30–32, 94, 95).

[87] G. Lindblad. On the generators of quantum dynamical semigroups. *Commun. Math. Phys.* 48, 119 (1976) (see p. 26).

[88] V. Gorini, A. Frigerio, M. Verri, A. Kossakowski, and E. C. G. Sudarshan. Properties of quantum Markovian master equations. *Rep. Math. Phys.* 13, 149 (1978) (see p. 26).

[89] M. E. Sorantin, W. von der Linden, R. Lucrezi, and E. Arrigoni. Nonequilibrium Green's functions and their relation to the negative differential conductance in the interacting resonant level model. *Phys. Rev. B* 99, 075139 (2019) (see p. 30).

[90] G. Stefanucci and R. van Leeuwen. *Nonequilibrium Many-Body Theory of Quantum Systems: A Modern Introduction* (Cambridge University Press, Cambridge, 2013) (see p. 30).

[91] H. Haug and A.-P. Jauho. *Quantum Kinetics in Transport and Optics of Semiconductors* (Springer, Heidelberg, 1998) (see pp. 30, 69).

[92] U. Schollwöck. The density-matrix renormalization group in the age of matrix product states. *Ann. Phys.* 326, 96 (2011) (see pp. 37, 39, 42, 43, 46–48, 51, 52, 59, 71, 97, 98, 100).

[93] G. Vidal. Efficient Classical Simulation of Slightly Entangled Quantum Computations. *Phys. Rev. Lett.* 91, 147902 (2003) (see pp. 46, 52, 58).

[94] F. Verstraete and J. I. Cirac. Matrix product states represent ground states faithfully. *Phys. Rev. B* 73, 094423 (2006) (see p. 49).

[95] J. Eisert, M. Cramer, and M. B. Plenio. Colloquium: Area laws for the entanglement entropy. *Rev. Mod. Phys.* 82, 277 (2010) (see p. 49).

[96] J. D. Bekenstein. Black Holes and Entropy. *Phys. Rev. D* 7, 2333 (1973) (see p. 49).

[97] M. Srednicki. Entropy and area. *Phys. Rev. Lett.* 71, 666 (1993) (see p. 49).

[98] C. Callan and F. Wilczek. On geometric entropy. *Phys. Lett. B* 333, 55 (1994) (see p. 49).

[99] M. B. Plenio, J. Eisert, J. Dreißig, and M. Cramer. Entropy, Entanglement, and Area: Analytical Results for Harmonic Lattice Systems. *Phys. Rev. Lett.* 94, 060503 (2005) (see p. 49).

[100] J. Haegeman, C. Lubich, I. Oseledets, B. Vandereycken, and F. Verstraete. Unifying time evolution and optimization with matrix product states. *Phys. Rev. B* 94, 165116 (2016) (see pp. 50, 60, 130).

[101] S. Paeckel, T. Köhler, A. Swoboda, S. R. Manmana, U. Schollwöck, and C. Hubig. Time-evolution methods for matrix-product states. *Ann. Phys.* 411, 167998 (2019) (see pp. 50, 60, 130).

[102] F. Verstraete, J. J. García-Ripoll, and J. I. Cirac. Matrix Product Density Operators: Simulation of Finite-Temperature and Dissipative Systems. *Phys. Rev. Lett.* 93, 207204 (2004) (see pp. 50, 52, 60).

[103] I. P. McCulloch. From density-matrix renormalization group to matrix product states. *J. Stat. Mech.* 2007, P10014 (2007) (see p. 50).

[104] G. M. Crosswhite and D. Bacon. Finite automata for caching in matrix product algorithms. *Phys. Rev. A* 78, 012356 (2008) (see p. 50).

[105] B. Pirvu, V. Murg, J. I. Cirac, and F. Verstraete. Matrix product operator representations. *New J. Phys.* 12, 025012 (2010) (see p. 50).

[106] F. Fröwis, V. Nebendahl, and W. Dür. Tensor operators: Constructions and applications for long-range interaction systems. *Phys. Rev. A* 81, 062337 (2010) (see p. 50).

[107] G. Vidal. Efficient Simulation of One-Dimensional Quantum Many-Body Systems. *Phys. Rev. Lett.* 93, 040502 (2004) (see pp. 52, 58, 71).

[108] A. J. Daley, C. Kollath, U. Schollwöck, and G. Vidal. Time-dependent density-matrix renormalization-group using adaptive effective Hilbert spaces. *J. Stat. Mech.* 2004, P04005 (2004) (see pp. 52, 56, 71, 97).

[109] S. R. White and A. E. Feiguin. Real-Time Evolution Using the Density Matrix Renormalization Group. *Phys. Rev. Lett.* 93, 076401 (2004) (see pp. 52, 56, 71, 97).

[110] E. M. Stoudenmire and S. R. White. Minimally entangled typical thermal state algorithms. *New J. Phys.* 12, 055026 (2010) (see pp. 54, 100).

[111] D. Bauernfeind. Fork Tensor Product States: Efficient Multi-Orbital Impurity Solver for Dynamical Mean FieldTheory. PhD thesis (Graz University of Technology, 2018). (see pp. 55, 56).

[112] M. B. Hastings. Light-cone matrix product. *J. Math. Phys.* 50, 095207 (2009) (see pp. 59, 60).

[113] M. Zwolak and G. Vidal. Mixed-State Dynamics in One-Dimensional Quantum Lattice Systems: A Time-Dependent Superoperator Renormalization Algorithm. *Phys. Rev. Lett.* 93, 207205 (2004) (see p. 60).

[114] A. J. Daley, J. M. Taylor, S. Diehl, M. Baranov, and P. Zoller. Atomic Three-Body Loss as a Dynamical Three-Body Interaction. *Phys. Rev. Lett.* 102, 040402 (2009) (see p. 60).

[115] D. C. Ralph and R. A. Buhrman. Kondo-assisted and resonant tunneling via a single charge trap: A realization of the Anderson model out of equilibrium. *Phys. Rev. Lett.* 72, 3401 (1994) (see pp. 64, 76).

[116] A. V. Kretinin, H. Shtrikman, D. Goldhaber-Gordon, M. Hanl, A. Weichselbaum, J. von Delft, T. Costi, and D. Mahalu. Spin-$\frac{1}{2}$ Kondo effect in an InAs nanowire quantum dot: Unitary limit, conductance scaling, and Zeeman splitting. *Phys. Rev. B* 84, 245316 (2011) (see pp. 64, 76).

[117] A. V. Kretinin, H. Shtrikman, and D. Mahalu. Universal line shape of the Kondo zero-bias anomaly in a quantum dot. *Phys. Rev. B* 85, 201301 (2012) (see pp. 64, 76).

[118] D. Goldhaber-Gordon, J. Göres, M. A. Kastner, H. Shtrikman, D. Mahalu, and U. Meirav. From the Kondo Regime to the Mixed-Valence Regime in a Single-Electron Transistor. *Phys. Rev. Lett.* 81, 5225 (1998) (see pp. 64, 87).

[119] M. Ferrier, T. Arakawa, T. Hata, R. Fujiwara, R. Delagrange, R. Deblock, Y. Teratani, R. Sakano, A. Oguri, and K. Kobayashi. Quantum Fluctuations along Symmetry Crossover in a Kondo-Correlated Quantum Dot. *Phys. Rev. Lett.* 118, 196803 (2017) (see p. 64).

[120] Y. Zhang, S. Kahle, T. Herden, C. Stroh, M. Mayor, U. Schlickum, M. Ternes, P. Wahl, and K. Kern. Temperature and magnetic field dependence of a Kondo system in the weak coupling regime. *Nat. Commun.* 4, 2110 (2013) (see p. 64).

[121] S. Amasha, I. J. Gelfand, M. A. Kastner, and A. Kogan. Kondo temperature dependence of the Kondo splitting in a single-electron transistor. *Phys. Rev. B* 72, 045308 (2005) (see p. 64).

[122] A. C. Hewson, J. Bauer, and A. Oguri. Non-equilibrium differential conductance through a quantum dot in a magnetic field. *J. Phys. Condens. Mat.* 17, 5413 (2005) (see pp. 64, 73, 76).

[123] A. Rosch, J. Paaske, J. Kroha, and P. Wölfle. Nonequilibrium Transport through a Kondo Dot in a Magnetic Field: Perturbation Theory and Poor Man's Scaling. *Phys. Rev. Lett.* 90, 076804 (2003) (see pp. 64, 66, 73, 76, 78).

[124] F. Reininghaus, M. Pletyukhov, and H. Schoeller. Kondo model in nonequilibrium: Interplay between voltage, temperature, and crossover from weak to strong coupling. *Phys. Rev. B* 90, 085121 (2014) (see p. 64).

[125] S. Smirnov and M. Grifoni. Nonequilibrium Kondo transport through a quantum dot in a magnetic field. *New J. Phys.* 15, 073047 (2013) (see pp. 64, 76).

[126] J. E. Moore and X.-G. Wen. Anomalous Magnetic Splitting of the Kondo Resonance. *Phys. Rev. Lett.* 85, 1722 (2000) (see pp. 65, 73).

[127] T. A. Costi. Kondo Effect in a Magnetic Field and the Magnetoresistivity of Kondo Alloys. *Phys. Rev. Lett.* 85, 1504 (2000) (see pp. 65, 73).

[128] T. A. Costi. In: *Concepts in Electron Correlation* (eds A. C. Hewson and V. Zlatić) 247 (Springer Science & Business Media, Dodrecht, 2003) (see pp. 65, 73).

[129] A. Rosch, T. A. Costi, J. Paaske, and P. Wölfle. Spectral function of the Kondo model in high magnetic fields. *Phys. Rev. B* 68, 014430 (2003) (see pp. 65, 83).

[130] Y. Meir and N. S. Wingreen. Landauer formula for the current through an interacting electron region. *Phys. Rev. Lett.* 68, 2512 (1992) (see pp. 65, 69).

[131] T. Prosen. Third quantization: a general method to solve master equations for quadratic open Fermi systems. *New J. Phys.* 10, 043026 (2008) (see p. 70).

[132] T. Prosen. Spectral theorem for the Lindblad equation for quadratic open fermionic systems. *J. Stat. Mech.* 2010, P07020 (2010) (see p. 70).

[133] E. Boulat, H. Saleur, and P. Schmitteckert. Twofold Advance in the Theoretical Understanding of Far-From-Equilibrium Properties of Interacting Nanostructures. *Phys. Rev. Lett.* 101, 140601 (2008) (see p. 71).

[134] F. Heidrich-Meisner, A. E. Feiguin, and E. Dagotto. Real-time simulations of nonequilibrium transport in the single-impurity Anderson model. *Phys. Rev. B* 79, 235336 (2009) (see p. 71).

[135] K. G. Wilson. The renormalization group: Critical phenomena and the Kondo problem. *Rev. Mod. Phys.* 47, 773 (1975) (see p. 71).

[136] Y. Takahashi and H. Umezawa. Thermo field dynamics. *Collect. Phenom.* 2, 55 (1975) (see p. 72).

[137] A. Das. In: *Quantum Field Theory - A 20th Century Profile* (ed A. N. Mitra) 383 (Hindustan Book Agency, New Delhi, 2000) (see p. 72).

[138] I. de Vega and M.-C. Bañuls. Thermofield-based chain-mapping approach for open quantum systems. *Phys. Rev. A* 92, 052116 (2015) (see p. 72).

[139] J. König, J. Schmid, H. Schoeller, and G. Schön. Resonant tunneling through ultrasmall quantum dots: Zero-bias anomalies, magnetic-field dependence, and boson-assisted transport. *Phys. Rev. B* 54, 16820 (1996) (see p. 73).

[140] N. Shah and A. Rosch. Nonequilibrium conductance of a three-terminal quantum dot in the Kondo regime: Perturbative renormalization group study. *Phys. Rev. B* 73, 081309 (2006) (see p. 73).

[141] P. Fritsch and S. Kehrein. Nonequilibrium Kondo model with voltage bias in a magnetic field. *Phys. Rev. B* 81, 035113 (2010) (see p. 73).

[142] C. J. Wright, M. R. Galpin, and D. E. Logan. Magnetic field effects in few-level quantum dots: Theory and application to experiment. *Phys. Rev. B* 84, 115308 (2011) (see p. 73).

[143] D. E. Logan and N. L. Dickens. Field-dependent dynamics of the Anderson impurity model. *J. Phys. Condens. Mat.* 13, 9713 (2001) (see p. 73).

[144] S. M. Cronenwett, T. H. Oosterkamp, and L. P. Kouwenhoven. A Tunable Kondo Effect of Quantum Dots. *Science* 281, 540 (1998) (see p. 76).

[145] A. Dirks, S. Schmitt, J. E. Han, F. Anders, P. Werner, and T. Pruschke. Double occupancy and magnetic susceptibility of the Anderson impurity model out of equilibrium. *Europhys. Lett.* 102, 37011 (2013) (see p. 78).

[146] A. Weichselbaum and J. von Delft. Sum-Rule Conserving Spectral Functions from the Numerical Renormalization Group. *Phys. Rev. Lett.* 99, 076402 (2007) (see p. 81).

[147] D. P. Kingma and J. Ba. Adam: A Method for Stochastic Optimization. *arXiv e-prints,* arXiv:1412.6980. (2014) (see pp. 85, 96).

[148] M. Abadi, A. Agarwal, P. Barham, E. Brevdo, Z. Chen, C. Citro, G. S. Corrado, A. Davis, J. Dean, M. Devin, S. Ghemawat, I. Goodfellow, A. Harp, G. Irving, M. Isard, Y. Jia, R. Jozefowicz, L. Kaiser, M. Kudlur, J. Levenberg, D. Mane, R. Monga, S. Moore, D. Murray, C. Olah, M. Schuster, J. Shlens, B. Steiner, I. Sutskever, K. Talwar, P. Tucker, V. Vanhoucke, V. Vasudevan, F. Viegas, O. Vinyals, P. Warden, M. Wattenberg, M. Wicke, Y. Yu, and X. Zheng. TensorFlow: Large-Scale Machine Learning on Heterogeneous Distributed Systems. *arXiv e-prints,* arXiv:1603.04467. (2016) (see pp. 85, 96).

[149] ITensor Library. http://itensor.org. (see pp. 86, 97).

[150] A. H. Wilson. *The Theory of Metals* (Cambridge University Press, Cambridge, 1953) (see p. 87).

[151] D. Vollhardt. Dynamical Mean-Field Theory of Electronic Correlations in Models and Materials. In: *Lecture Notes on the Physics of Strongly Correlated Systems* (eds A. Avella and F. Mancini) 1297 (AIP, New York, 2010), 339. (see p. 87).

[152] B. A. Volkov and O. A. Pankratov. Two-dimensional massless electrons in an inverted contact. *Pis. Zh. Eksp. Teor. Fiz.* 42, 145. (1985) (see p. 88).

[153] M. Sigrist and K. Ueda. Phenomenological theory of unconventional superconductivity. *Rev. Mod. Phys.* 63, 239 (1991) (see p. 88).

[154] M. Vojta. Impurity quantum phase transitions. *Phil. Mag.* 86, 1807 (2006) (see p. 88).

[155] L. S. Borkowski and P. J. Hirschfeld. Kondo effect in gapless superconductors. *Phys. Rev. B* 46, 9274 (1992) (see p. 88).

[156] C. R. Cassanello and E. Fradkin. Kondo effect in flux phases. *Phys. Rev. B* 53, 15079 (1996) (see p. 88).

[157] C. R. Cassanello and E. Fradkin. Overscreening of magnetic impurities in $d_{x^2-y^2}$-wave superconductors. *Phys. Rev. B* 56, 11246 (1997) (see p. 88).

[158] M. Vojta and R. Bulla. Kondo effect of impurity moments in d-wave superconductors: Quantum phase transition and spectral properties. *Phys. Rev. B* 65, 014511 (2001) (see p. 88).

[159] K. Chen and C. Jayaprakash. The Kondo effect in pseudo-gap Fermi systems: a renormalization group study. *J. Phys. Condens. Mat.* 7, L491 (1995) (see pp. 88, 106).

[160] C. Gonzalez-Buxton and K. Ingersent. Stabilization of local moments in gapless Fermi systems. *Phys. Rev. B* 54, R15614 (1996) (see pp. 88, 106).

[161] K. Ingersent. Behavior of magnetic impurities in gapless Fermi systems. *Phys. Rev. B* 54, 11936 (1996) (see pp. 88, 106).

[162] R. Bulla, T. Pruschke, and A. C. Hewson. Anderson impurity in pseudo-gap Fermi systems. *J. Phys. Condens. Mat.* 9, 10463 (1997) (see pp. 88, 106).

[163] C. Gonzalez-Buxton and K. Ingersent. Renormalization-group study of Anderson and Kondo impurities in gapless Fermi systems. *Phys. Rev. B* 57, 14254 (1998) (see pp. 88, 106).

[164] D. E. Logan and M. T. Glossop. A local moment approach to magnetic impurities in gapless Fermi systems. *J. Phys. Condens. Mat.* 12, 985 (2000) (see pp. 88, 106).

[165] M. T. Glossop and D. E. Logan. Magnetic impurities in gapless Fermi systems: perturbation theory. *Eur. Phys. J. B* 13, 513 (2000) (see pp. 88, 104, 106, 108).

[166] R. Bulla, M. T. Glossop, D. E. Logan, and T. Pruschke. The soft-gap Anderson model: comparison of renormalization group and local moment approaches. *J. Phys. Condens. Mat.* 12, 4899 (2000) (see pp. 88, 106, 108, 111).

[167] K. Ingersent and Q. Si. Critical Local-Moment Fluctuations, Anomalous Exponents, and ω/T Scaling in the Kondo Problem with a Pseudogap. *Phys. Rev. Lett.* 89, 076403 (2002) (see pp. 88, 106).

[168] M. T. Glossop and D. E. Logan. Spectral scaling and quantum critical behaviour in the pseudogap Anderson model. *Europhys. Lett.* 61, 810 (2003) (see pp. 88, 106).

[169] M. Vojta and L. Fritz. Upper critical dimension in a quantum impurity model: Critical theory of the asymmetric pseudogap Kondo problem. *Phys. Rev. B* 70, 094502 (2004) (see pp. 88, 106).

[170] L. Fritz, S. Florens, and M. Vojta. Universal crossovers and critical dynamics of quantum phase transitions: A renormalization group study of the pseudogap Kondo problem. *Phys. Rev. B* 74, 144410 (2006) (see pp. 88, 106).

[171] H.-J. Lee, R. Bulla, and M. Vojta. Numerical renormalization group for impurity quantum phase transitions: structure of critical fixed points. *J. Phys. Condens. Mat.* 17, 6935 (2005) (see pp. 88, 106).

[172] R. Bulla, T. A. Costi, and T. Pruschke. Numerical renormalization group method for quantum impurity systems. *Rev. Mod. Phys.* 80, 395 (2008) (see pp. 88, 106).

[173] M. T. Glossop, S. Kirchner, J. H. Pixley, and Q. Si. Critical Kondo Destruction in a Pseudogap Anderson Model: Scaling and Relaxational Dynamics. *Phys. Rev. Lett.* 107, 076404 (2011) (see pp. 88, 106).

[174] T. Kanao, H. Matsuura, and M. Ogata. Theory of Defect-Induced Kondo Effect in Graphene: Numerical Renormalization Group Study. *J. Phys. Soc. Jpn.* 81, 063709 (2012) (see pp. 88, 106).

[175] L. Fritz and M. Vojta. The physics of Kondo impurities in graphene. *Rep. Prog. Phys.* 76, 032501 (2013) (see pp. 88, 106).

[176] T. Aono. Electrical and Thermoelectrical Transport Properties of Dirac Fermions through a Quantum Dot. *J. Phys. Soc. Jpn.* 82, 083703 (2013) (see pp. 88, 106).

[177] S. Diehl, A. Micheli, A. Kantian, B. Kraus, H. P. Büchler, and P. Zoller. Quantum states and phases in driven open quantum systems with cold atoms. *Nat. Phys.* 4, 878 (2008) (see p. 88).

[178] P. M. Hogan and A. G. Green. Universal nonlinear conductivity close to an itinerant-electron quantum critical point. *Phys. Rev. B* 78, 195104 (2008) (see p. 88).

[179] C.-H. Chung, K. Le Hur, M. Vojta, and P. Wölfle. Nonequilibrium Transport at a Dissipative Quantum Phase Transition. *Phys. Rev. Lett.* 102, 216803 (2009) (see p. 88).

[180] S. Kirchner and Q. Si. Quantum Criticality Out of Equilibrium: Steady State in a Magnetic Single-Electron Transistor. *Phys. Rev. Lett.* 103, 206401 (2009) (see p. 88).

[181] S. Takei, W. Witczak-Krempa, and Y. B. Kim. Nonequilibrium quantum criticality in bilayer itinerant ferromagnets. *Phys. Rev. B* 81, 125430 (2010) (see p. 88).

[182] P. Ribeiro, Q. Si, and S. Kirchner. Local quantum criticality out of equilibrium: Effective temperatures and scaling in the steady-state regime. *Europhys. Lett.* 102, 50001 (2013) (see p. 88).

[183] L. M. Sieberer, S. D. Huber, E. Altman, and S. Diehl. Dynamical Critical Phenomena in Driven-Dissipative Systems. *Phys. Rev. Lett.* 110, 195301 (2013) (see p. 88).

[184] M. Schiró. Nonequilibrium dynamics across an impurity quantum critical point due to quantum quenches. *Phys. Rev. B* 86, 161101 (2012) (see p. 88).

[185] C.-H. Chung and K. Y.-J. Zhang. Quantum criticality out of equilibrium in the pseudogap Kondo model. *Phys. Rev. B* 85, 195106 (2012) (see p. 88).

[186] P. Ribeiro, F. Zamani, and S. Kirchner. Steady-State Dynamics and Effective Temperature for a Model of Quantum Criticality in an Open System. *Phys. Rev. Lett.* 115, 220602 (2015) (see p. 88).

[187] B. Hara, A. Koga, and T. Aono. Transport properties for a quantum dot coupled to normal leads with a pseudogap. *Phys. Rev. B* 92, 081103 (2015) (see pp. 89, 118).

[188] F. Chen, E. Arrigoni, and M. Galperin. Markovian treatment of non-Markovian dynamics of open Fermionic systems. *New J. Phys.* 21, 123035 (2019) (see p. 94).

[189] D. Bauernfeind, M. Zingl, R. Triebl, M. Aichhorn, and H. G. Evertz. Fork Tensor-Product States: Efficient Multiorbital Real-Time DMFT Solver. *Phys. Rev. X* 7, 031013 (2017) (see pp. 97, 102, 104, 118, 120).

[190] T. Barthel, U. Schollwöck, and S. R. White. Spectral functions in one-dimensional quantum systems at finite temperature using the density matrix renormalization group. *Phys. Rev. B* 79, 245101 (2009) (see p. 102).

[191] S. Sasaki, S. De Franceschi, J. M. Elzerman, W. G. van der Wiel, M. Eto, S. Tarucha, and L. P. Kouwenhoven. Kondo effect in an integer-spin quantum dot. *Nature* 405, 764 (2000) (see p. 130).

[192] P. P. Baruselli, R. Requist, M. Fabrizio, and E. Tosatti. Ferromagnetic Kondo Effect in a Triple Quantum Dot System. *Phys. Rev. Lett.* 111, 047201 (2013) (see p. 130).

[193] A. J. Keller, L. Peeters, C. P. Moca, I. Weymann, D. Mahalu, V. Umansky, G. Zaránd, and D. Goldhaber-Gordon. Universal Fermi liquid crossover and quantum criticality in a mesoscopic system. *Nature* 526, 237 (2015) (see p. 130).